Tutorial

Quantum Electrodynamics of Intense Laser-Matter Interactions: A Tool for Quantum State Engineering

Philipp Stammer,[1,*] Javier Rivera-Dean,[1] Andrew Maxwell,[1,2] Theocharis Lamprou,[3,4] Andrés Ordóñez,[1] Marcelo F. Ciappina,[5,6,7] Paraskevas Tzallas,[3,8] and Maciej Lewenstein[1,9]

[1]*ICFO-Institut de Ciencies Fotoniques, The Barcelona Institute of Science and Technology, Castelldefels, Barcelona 08860, Spain*

[2]*Department of Physics and Astronomy, Aarhus University, Aarhus C DK-8000, Denmark*

[3]*Foundation for Research and Technology-Hellas, Institute of Electronic Structure & Laser, Heraklion, Crete GR-70013, Greece*

[4]*Department of Physics, University of Crete, P.O. Box 2208, Heraklion, Crete GR-71003, Greece*

[5]*Physics Program, Guangdong Technion—Israel Institute of Technology, Shantou, Guangdong 515063, China*

[6]*Technion—Israel Institute of Technology, Haifa 32000, Israel*

[7]*Guangdong Provincial Key Laboratory of Materials and Technologies for Energy Conversion, Guangdong Technion—Israel Institute of Technology, Shantou, Guangdong 515063, China*

[8]*ELI-ALPS, ELI-Hu Non-Profit Ltd., Dugonics tér 13, Szeged, H-6720 Hungary*

[9]*ICREA, Pg. Lluís Companys 23, Barcelona 08010, Spain*

Intense laser-matter interactions are at the center of interest in research and technology since the development of high-power lasers. They have been widely used for fundamental studies in atomic, molecular, and optical physics, and they are at the core of attosecond physics and ultrafast optoelectronics. Although the majority of these studies have been successfully described using classical electromagnetic fields, recent investigations based on fully quantized approaches have shown that intense laser-atom interactions can be used for the generation of controllable high-photon-number entangled coherent states and coherent state superpositions. In this tutorial, we provide a comprehensive fully quantized description of intense laser-atom interactions. We elaborate on the processes of high-harmonic generation, above-threshold ionization, and we discuss new phenomena that cannot be revealed within the context of semiclassical theories. We provide the description for conditioning the light field on different electronic processes, and their consequences for quantum state engineering of light. Finally, we discuss the extension of the approach to more complex materials, and the impact to quantum technologies for a new photonic platform composed of the symbiosis of attosecond physics and quantum information science.

CONTENTS

*philipp.stammer@icfo.eu

I. INTRODUCTION

A. Quantum optics and superintense laser-atom interaction physics

There were two instances that gave rise to the birth of quantum optics: the invention of the laser (and earlier maser) (cf. Ref. [1] and the references therein), and the formulation of the quantum theory of optical coherence by Roy Glauber and George Sudarshan (cf. Refs. [2–4]). At the time of its infancy, and also much later, quantum optics was considered to be "an applied quantum electrodynamics (QED)" (see, for instance, Ref. [5]). From the perspective of atomic molecular and optical physics, QED concerns itself with very advanced, and precise perturbation theory calculations of various quantities relevant for spectroscopic measurements (cf. Refs. [6–8]). Quantum optics, on the other hand, focused for many years on single- or few-body phenomena, trying to understand nonperturbative aspects of atom-light interaction (for a recent overview, see Ref. [9]).

One of the areas of quantum optics that aimed at exploring nonperturbative effects was the so-called strong laser field physics, sometimes termed superintense laser-atom interaction physics (SILAP). The history of this area is well illustrated in the collection of essays on the relevant subjects in the Handbook [10]. At the beginning there was light, but then there were photons. The lasers were strong, but not strong enough, so they were mainly used to generate multiphoton resonant, and then nonresonant processes such as absorption, ionization, or very sophisticated high-order perturbation theory.

With the advent of stronger and stronger lasers came the revolution. The multiphoton processes became nonaccessible to even very high-order perturbation theory. The key strong-field nonperturbative processes are depicted in Fig. 1, which includes above-threshold ionization (ATI), also termed strong-field ionization; high-harmonic generation (HHG), where the photoelectron laser-driven recombination leads to the emission of a high-energy photon; and nonsequential double ionization (NSDI), in which the photoelectron laser-driven recollision leads to the ionization of a second electron. The history of these events is well described in the recent review on the strong-field approximation (SFA) [12], and in several reviews on the subject, which started with the observations of nonperturbative plateaus in ATI [13–15], together with nonperturbative plateaus and cutoff in HHG [16–18], or multielectron ionization, in particular NSDI (cf. Refs. [19–23]). Nowadays, this physics extends from atomic targets [18] to molecules (cf. Refs. [24–27]), atomic clusters (cf. Refs. [28–30]), solids (cf. Ref. [31]), two-dimensional (topological) materials (cf. Refs. [32,33]), and much more. The theoretical methods of this era forgot about QED, and describe the strong laser fields entirely classically. Independently of the process of interest, various theoretical approaches
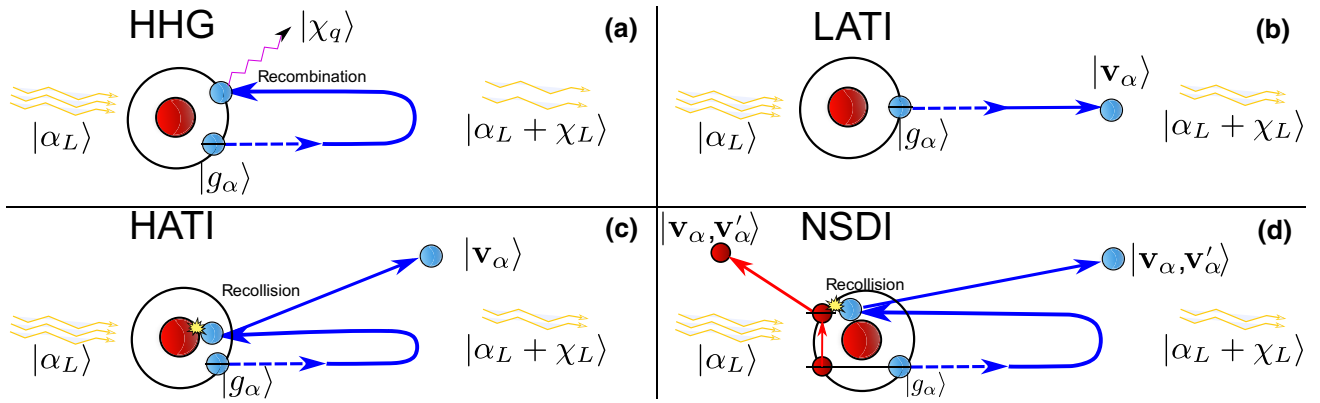
FIG. 1. Depiction of the key quasiclassical strong-field processes, along with the quantum states of light and matter. (a) High-harmonic generation (HHG), (b) low-order above-threshold ionization (LATI) without rescattering events, (c) high-order above-threshold ionization (HATI) including rescattering events, (d) nonsequential double ionization (NSDI). The states of the driving field mode before and after interaction are given by $|\alpha_L\rangle$ and $|\alpha_L + \chi_L\rangle$, respectively. High-order harmonic modes, due to HHG, are given by $|\chi_q\rangle$. The initial and final electronic states are given by $|g_\alpha\rangle$ and $|\mathbf{v}_\alpha\rangle$. To emphasize that the electrons in NSDI may be entangled [11], we have written them as a two-particle state. The quantum optical degrees of freedom may also be entangled with each other and the electronic states; however, for clearer labeling, we have written these separately.

may be used, but all of them assume only the classical nature of the driving laser fields and neglect their quantum fluctuations [34].

B. SILAP—theoretical approaches

Below we list the most important theory approaches to the three most relevant processes of SILAP, each of which is pictorially represented in Fig. 1.

(a) *High-harmonic generation—simple atoms.* For simple atoms, that is, for instance, hydrogen or noble gases, the single-atom response may be calculated using the time-dependent Schrödinger equation in the single active electron (SAE) approximation; it usually works perfectly. Going beyond SAE is rarely necessary, but may be achieved using the time-dependent Hartree-Fock approach [35,36], the time-dependent density functional method [37,38], or quantum chemistry methods such as the time-dependent configuration-interaction method [39,40]. Unfortunately, the full description of the HHG process also requires taking into account propagation effects (cf. Ref. [18]). That often makes the use of the time-dependent Schrödinger equation (TDSE) too demanding, leaving as the reasonable alternative the SFA [12]. The SFA, combined with propagation codes solving classical Maxwell equations, usually gives very satisfactory results. Of course, there are more approaches one can use at the single-atom level: (i) for longer pulses, one can use Floquet or *R*-matrix theory (cf. Ref. [41]);

(ii) for short, intense pulses, the ultimate description belongs to the TDSE; (iii) in some regimes of parameters, even more "brutal" than the SFA, classical (truncated Wigner) methods can be useful (cf. Refs. [42–44]).

(b) *High-harmonic generation—complex targets.* For more complex atoms (with non-negligible electronic correlations) or molecules, the SFA seems to be the only method, although Floquet methods and the *R* matrix work reasonable well for long laser pulses. The situation changes when we go to solids and truly many-body systems. In the weakly correlated cases one can apply the semiconductor Bloch equations [31,45], or the little more flexible Wannier-Bloch approach [46]. But, in the case of strongly correlated systems, more sophisticated approaches must be used: from density functional theory, through exact diagonalization for small systems (cf. Refs. [47–49]) to more advanced mean field theories like the generalized time-dependent pairing theory (cf. Ref. [50]), dynamical mean field theory [51–53], or slave boson theories [54] in a time-dependent version.

(c) *Above-threshold ionization—simple atoms.* For single targets, the same methods as mentioned above can be used [55,56]. While propagation effects are not relevant here as the outputs in this case are photoelectrons, ponderomotive effects and averaging over the spatial intensity profile of the laser pulse are, however, extremely relevant.

(d) *Above-threshold ionization—complex targets.* Obviously, this is particularly challenging, even if

the multielectron effects play no role. The high-energy parts of ATI spectra come from rescattering processes that are possible, but technically hard, to describe with the SFA [57–61]. Again, the ponderomotive effect and averaging over the spatial intensity profile of the laser pulse should be taken into account [62].

(e) *Sequential and nonsequential double ionization.* For simple two-electron systems (helium [63–66]), one-dimensional (1D) two-electron models [67–70], or quasi-3D models [71,72]), one can use the TDSE approach in various "flavors." The quasi-3D approach can even be generalized to three-electron systems [73]. Otherwise, we can only apply approximate methods, such as the SFA; see, e.g., Ref. [74].

C. SILAP and QED

All of these approaches are amazingly impressive and have led to a tremendous amount of important results, but all of them neglect the genuine QED nature of light. Recently, this orthodox paradigm seems to be questioned more and more often. For instance, some of the early papers with "QED" flavor treated the laser field in a QED manner to develop a frequency domain theory for HHG, ATI, and NSDI, which later they used to describe an x-ray pulse in assisted HHG and NSDI [75–78].

More recently, a new line of research was initiated by P. Tzallas and his collaborators, combining quantum optics methods with SILAP. In their two pioneering papers, they observed quantum optical signatures in strong-field laser physics by looking at the infrared photon counting in HHG [79]. In the subsequent paper [80], high-order harmonics were measured by the photon statistics of the infrared driving field exiting the atomic medium. These ideas stimulated other groups to look on QED aspects of SILAP in a more detailed way. I. Kaminer with his collaborators discussed the quantum optical nature of HHG [81] (see also Ref. [82]). They presented a fully quantum theory of extreme nonlinear optics, predicting quantum effects that alter both the spectrum and photon statistics of HHG. In particular, they predicted the emission of shifted frequency combs and identified spectral features arising from the breakdown of the dipole approximation for the emission. Each frequency component of HHG can be bunched and squeezed, and each emitted photon is a superposition of all frequencies in the spectrum, i.e., each photon is a comb. G. Paulus *et al.* looked at the photon counting of extreme ultraviolet high harmonics using a superconducting nanowire single-photon detector [83]. Triggered by recent developments on radiation sources of high-power pulsed squeezed light [84,85], Gorlach *et al.* [86] initiated investigations towards the generation of high harmonics driven by intense squeezed light sources. In a series of papers, S. Varro's group studied the quantum optical

aspects of HHG [87], developing quantum optical models [88], and a quantum optical description of photon statistics and cross-correlation [89].

Our approach followed the earlier ideas of the Crete group, and focused on the experiments in which quantum electrodynamical properties of the driving laser field were observed upon (a) conditioning on HHG, and (b) coherent diminution of the amplitudes of the light field, allowing for the final reconstruction of the Wigner function of the laser mode using quantum tomography. Our results, and their possible implications for applications in quantum information and quantum technologies, were described in a series of papers [90–95]. The culmination of this approach was the observation of a massive optical Schrödinger "cat" state of the fundamental laser mode, conditioned on the HHG process.

D. Motivation and goals of this paper

The main motivation and goals of the present manuscript are as follows.

(a) We provide a full detailed theoretical quantum electrodynamical (QED) formulation of the quantum optics of intense laser-atom interactions. In particular, we describe the processes of HHG and ATI, and characterize their backaction on the coherent state of the driving laser field. Furthermore, we show how quantum operations (conditioning measurements) on HHG and ATI can lead to coherent state superpositions with controllable quantum features. Such Schrödinger "catlike" or "kittenlike" states offer, in principle, fascinating possibilities for applications in quantum technologies.

(b) We discuss what are the experimental conditions needed to control the quantum features of the light state after HHG and ATI. In particular, we show how it is possible to switch the quantum character of the generated Schrödinger optical "catlike" states to "kittenlike" states, and how new observables, e.g., the photon number, inherit information about the quantum nature of the laser-matter interaction processes. Finally, we show the conditions under which the generation of high-photon-number optical "cat" states is possible.

All of this material will be presented in a didactic form. We believe that our tutorial will contribute to the more complete understanding of the strong-field matter processes from a full quantum electrodynamical viewpoint, and to the development of new methods that naturally lead to the creation of massive superpositions and massive entangled states, such as high-photon-number coherent state superpositions with controllable quantum features. Generating, certifying, and applying such states could greatly advance quantum technology.

We attempt, *toutes proportiones gardées*, to shape our tutorial inspired by the best of the best: Cohen-Tannoudji's books [96,97], or the reference paper on quantum optics of dielectric media [98]. Therefore, we first formulate a complete QED theory, including a general description of dynamics, starting from the minimal coupling $\mathbf{p} \cdot A$ ("velocity gauge") Hamiltonian, and discussing cutoff issues. We then carefully discuss going to the $\mathbf{d} \cdot E$ ("length gauge") description, also considering the divergent role of the $\mathbf{x}^2$ term, and introducing the dipole approximation for one atom.

We formulate the problem by assuming as an initial state the coherent state of the modes, contributing to the fundamental laser pulse, and vacuum otherwise. We employ various unitary transformations by going to the interaction picture with respect to the free-field Hamiltonian, shifting away the initial coherent state of the driving laser, and finally moving to the interaction picture with respect to the semiclassical Hamiltonian. We pay a lot of attention to the conditioning idea and its "advantages": conditioning is here the basic, natural tool that allows generation of quantum correlated states.

The presentation is therefore quite technical, but we hope it will indeed be useful for newcomers to the area: it will allow them to understand the basics of the theory and the known results, and, more importantly, the essence of the future challenges and questions to be studied and tackled.

The plan of this tutorial is thus as follows.

(a) Section I is an introduction, discussing the state of the art, motivations, and objectives.
(b) Section II contains the preliminaries, and in particular provides a brief introduction to QED.
(c) Section III focuses on laser-matter interactions, and describes the basic Hamiltonian of a single active electron in a laser field, both in the "velocity" and "length" gauges. We then discuss various approximations used (the dipole approximation, in particular), and the dynamics of the systems.
(d) Section IV is devoted to the discussion of the conditioning methods, which provide our basic tool for the engineering of massively quantum correlated states.
(e) Section V discusses the experimental aspects of the proposed quantum engineering approach based on conditioning.
(f) Finally, Secs. VI and VII contain a discussion of the results and the outlook for future investigations, respectively.

The paper also contains seven appendices with more technical aspects of the derivations, calculations, and numerical simulations.

II. PRELIMINARIES

A. Electromagnetic field operator and Hamiltonian

To derive the microscopic response of the matter to the optical field, and the respective change of the electromagnetic (EM) field quantities, we consider the Hamiltonian [96,97,99]

$$H = H_f + H_{A+f}, \tag{1}$$

where the free-field Hamiltonian H_f consists of the transverse part of the electromagnetic field

$$H_f = \frac{1}{2} \int d^3r \left\{ \frac{1}{\epsilon_0} \mathbf{\Pi}^2(\mathbf{r}) + \frac{1}{\mu_0} [\nabla \times \mathbf{A}(\mathbf{r})]^2 \right\}. \tag{2}$$

The dynamical field variables are given by the vector potential $\mathbf{A}(\mathbf{r})$, and the canonical conjugate field momentum $\mathbf{\Pi}(\mathbf{r}) = \epsilon_0 \partial \mathbf{A}(\mathbf{r}, t)/\partial t$, with the corresponding commutation relation given by $[A_m(\mathbf{r}), \Pi_n(\mathbf{r}')] = i\hbar \delta_{mn}^{\perp}(\mathbf{r} - \mathbf{r}')$, where $\delta_{mn}^{\perp}(\mathbf{r} - \mathbf{r}')$ is the transverse δ function (see Appendix A for details). We use the common procedure of expressing the dynamical variables in a plane-wave expansion

$$\mathbf{A}(\mathbf{r}) = \sum_\mu \int d^3k \left[\sqrt{\frac{\hbar}{2\epsilon_0 ck(2\pi)^3}} g(k) \boldsymbol{\epsilon}_{\mathbf{k}\mu} a_{\mathbf{k}\mu} e^{i\mathbf{k}\cdot\mathbf{r}} + \text{H.c.} \right], \tag{3}$$

where $\boldsymbol{\epsilon}_{\mathbf{k}\mu}$ is the polarization vector for the field mode $\mathbf{k} = (k_x, k_y, k_z)^T$ in the polarization mode μ. We introduced here a regularizing factor $g(k)$, describing the cutoff of the matter-field coupling at high frequencies, i.e. high momenta (see Remark 1 below). The bosonic creation and annihilation operators $a_{\mathbf{k}\mu}^{(\dagger)}$ obey the commutation relation

$$[a_{\mathbf{k}\mu}, a_{\mathbf{k}'\nu}^{\dagger}] = \delta_{\mu\nu}\delta(\mathbf{k} - \mathbf{k}'). \tag{4}$$

Note that we have used the Coulomb gauge $\nabla \cdot \mathbf{A} = 0$ in which $\boldsymbol{\epsilon}_{\mathbf{k}\mu} \perp \mathbf{k}$. The canonical conjugate momentum field is given by

$$\mathbf{\Pi}(\mathbf{r}) = -i \sum_\mu \int d^3k \sqrt{\frac{\hbar\epsilon_0 ck}{2(2\pi)^3}} g(k) \boldsymbol{\epsilon}_{\mathbf{k}\mu} a_{\mathbf{k}\mu} e^{i\mathbf{k}\cdot\mathbf{r}} + \text{H.c.}, \tag{5}$$

such that we can express the free-field Hamiltonian (2) in the form

$$H_f = \sum_\mu \int d^3k \, \hbar\omega_k \left(a_{\mathbf{k}\mu}^{\dagger} a_{\mathbf{k}\mu} + \frac{1}{2} \right) \tag{6}$$

with frequency $\omega_k = c|\mathbf{k}|$ of mode $\mathbf{k}$.

B. Coherent states of light and their superposition

From a classical perspective, the EM field generated by a laser source is often described as a single-mode wave with a well-defined amplitude and phase. However, in the quantum theory of radiation the amplitude and the phase are conjugate variables, and therefore cannot be determined with arbitrary accuracy in the same experiment. The state for which the product of the variances of those two quantities reaches the lower limit, and therefore provides the optimal description of the classical field, is given by *coherent states of light*

$$|\alpha\rangle = e^{-|\alpha|^2/2} \sum_{n=0}^{\infty} \frac{\alpha^n}{\sqrt{n!}} |n\rangle, \tag{7}$$

which is a coherent superposition of Fock states $|n\rangle$ of a single mode, with $\alpha \in \mathbb{C}$ the coherent state amplitude. Coherent states of light are said to be classical states of light, and their properties can be described by classical EM theory.

In order to provide physical intuition on how coherent states are generated, we consider the most basic example of a light source, which is that of a *classical* charge described by the current $\mathbf{J}(\mathbf{r}, t) \in \mathbb{R}^3$ [100]. The charge current couples to the EM field (now for the general multimode case) via the vector potential, given by the operator $\mathbf{A}(\mathbf{r}, t)$ in Eq. (3). The Schrödinger equation describing the dynamics of the state of the EM field is

$$i\hbar \frac{d}{dt} |\phi(t)\rangle = \int d^3r \, \mathbf{J}(\mathbf{r}, t) \cdot \mathbf{A}(\mathbf{r}, t) |\phi(t)\rangle \tag{8}$$

with the solution given by

$$|\phi(t)\rangle = \mathcal{T} \exp\left\{-\frac{i}{\hbar} \int_{t_0}^{t} dt' \int d^3r \mathbf{J}(\mathbf{r}, t') \cdot \mathbf{A}(\mathbf{r}, t')\right\} |\phi(t_0)\rangle$$
$$= \prod_{\mathbf{k}\mu} e^{i\varphi_{\mathbf{k}\mu}} \exp[\alpha_{\mathbf{k},\mu}(t) a_{\mathbf{k}\mu}^\dagger - \alpha_{\mathbf{k},\mu}^*(t) a_{\mathbf{k}\mu}] |\phi(t_0)\rangle, \tag{9}$$

where we have used the definition of the vector potential in Eq. (3), and the initial state of the EM field $|\phi(t_0)\rangle$. Thus, the coupling of the charge current to the EM field induces a shift of the initial state via the displacement operator

$$D(\alpha_{\mathbf{k}\mu}) = \exp[\alpha_{\mathbf{k}\mu} a_{\mathbf{k}\mu}^\dagger - \alpha_{\mathbf{k}\mu}^* a_{\mathbf{k}\mu}]. \tag{10}$$

This operator shifts each mode of the initial state by a quantity $\alpha_{\mathbf{k},\mu}(t)$ given by

$$\alpha_{\mathbf{k},\mu}(t) = \frac{i}{\hbar} \tilde{g}(k) \int_{t_0}^{t} dt' \int d^3r \mathbf{J}(\mathbf{r}, t) \cdot \boldsymbol{\epsilon}_{\mathbf{k},\mu} e^{-i\omega_k t + i\mathbf{k}\cdot\mathbf{r}}, \tag{11}$$

which corresponds to the Fourier transform of the classical charge current. Thus, up to a global phase, we can

define the coherent state of light in mode $\{\mathbf{k}, \mu\}$ when the displacement operator is acting on the initial vacuum state

$$|\alpha_{\mathbf{k}\mu}\rangle = \exp[\alpha_{\mathbf{k},\mu}(t) a_{\mathbf{k}\mu}^\dagger - \alpha_{\mathbf{k},\mu}^*(t) a_{\mathbf{k}\mu}] |0_{\mathbf{k}\mu}\rangle, \tag{12}$$

which are eigenstates of the annihilation operator $a_{\mathbf{k}\mu} |\alpha_{\mathbf{k}\mu}\rangle = \alpha_{\mathbf{k}\mu} |\alpha_{\mathbf{k}\mu}\rangle$. Hence, the oscillation of a classical charge current generates states of light that satisfy the lower bound in the uncertainty relation between the field amplitude and phase. Furthermore, this uncertainty keeps saturated during their free-field evolution, that is, these states remain coherent states when they freely propagate.

For the reasons stated before, coherent states are said to be *classical states*, since their properties can be recovered by classical EM theory. However, despite the fact that coherent states are classical states of light, the superposition of two different coherent states can exhibit genuine quantum features without a classical counterpart [101]. The generic form of a coherent state superposition (CSS) in a single field mode reads

$$|\phi\rangle = \sum_i a_i |\alpha_i\rangle. \tag{13}$$

One of the most well-known examples of CSS are the so-called Schrödinger cat states [101], which consist of the superposition of two macroscopically distinguishable coherent states. The superposition of coherent states can lead to highly nonclassical features that can be witnessed in different ways, e.g., by means of negativities in their Wigner function representation [102,103]. Furthermore, these states can be combined with linear optical elements such as beam splitters [104] to generate entangled coherent states [105], which are useful in many different applications of quantum information science [106] such as quantum communications [107], quantum computation [108,109], and quantum metrology [110].

In the context of the present paper, we are mainly interested in generating nonclassical field states in the fundamental driving laser mode, and therefore compute the backaction on this mode due to the interaction with a gas medium. To measure the change of the driving laser mode, we consider the photon-number probability distribution of coherent states and their superposition. The probability distribution of finding n photons in a single-mode coherent state with amplitude α is Poissonian

$$P(n) = |\langle n|\alpha\rangle|^2 = e^{-|\alpha|^2} \frac{|\alpha|^{2n}}{n!}, \tag{14}$$

where the mean $\langle n \rangle = \langle \alpha| a^\dagger a |\alpha\rangle = |\alpha|^2$ and the variance $(\Delta n)^2 = |\alpha|^2$ are equal. Photon distributions are shown in Fig. 2(a) for $\alpha = 7.95$ (red dashed curve) and 8.73 (black solid curve). Both distributions show a maximum peak at the mean photon value of the distribution, $\langle n \rangle \approx 63.2$
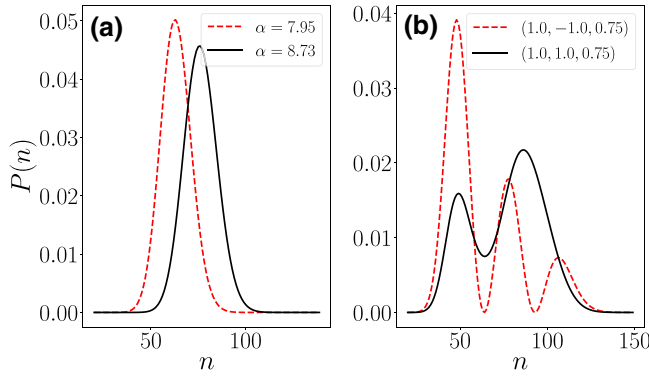
FIG. 2. Photon-number probability distributions for (a) two coherent states with $\alpha = 7.95$ (red dashed curve) and $\alpha = 8.73$ (black solid curve), and (b) a superposition of three coherent states of the form $|\phi\rangle = a_1 |7\rangle + a_2 |9\rangle + a_3 |10\rangle$ with $(a_1, a_2, a_3) = (1.0, -1.0, 0.75)$ (red dashed curve) and $(a_1, a_2, a_3) = (1.0, 1.0, 0.75)$ (black solid curve). The coefficients in the superposition are shown up to a normalization that, nonetheless, has been taken into account when doing the plots. In both plots, the mean photon number is $\langle n \rangle \approx 63.2$ for the red dashed curve probability distribution and $\langle n \rangle \approx 76.2$ for the black solid line.

and $\langle n \rangle \approx 76.2$, respectively. On the other hand, for the coherent state superposition presented in Eq. (13), the photon-number probability distribution is given by

$$P(n) = \left| \sum_i a_i e^{-|\alpha_i|^2/2} \frac{(\alpha_i)^n}{\sqrt{n!}} \right|^2, \qquad (15)$$

which is not a Poissonian distribution anymore due to the interference between the different coherent states $|\alpha_i\rangle$. In Fig. 2(b), we show the obtained probability distribution of a superposition of three coherent states of the form $|\phi\rangle = a_1 |7\rangle + a_2 |9\rangle + a_3 |10\rangle$, when considering different relative phases of the corresponding probability amplitudes a_i. In particular, the mean photon numbers of the two distributions that are shown coincide with those considered for the coherent states in Fig. 2(a). Yet, the distributions are very different for the coherent state superposition, and we observe a multipeak structure. The main difference between the black solid line and the red dashed curve in (b) lies in the relative phase of the $|9\rangle$ coherent state as it differs by π from one case to the other. Depending on this relative phase, we either get a multipeak probability distribution, or a situation where two of the peaks are very close to each other and are indistinguishable.

III. INTENSE LASER-MATTER INTERACTION

A. Minimal coupling Hamiltonian—the velocity gauge

The primary goal of the present tutorial is to describe the dynamics of many particles in the gas phase in strong laser fields, taking into account the full quantum electrodynamic nature of the intense driving laser field. We consider N atoms or molecules located at $\mathbf{R}_\alpha$, $\alpha = 1, \ldots, N$, in the SAE approximation. Readers familiar with fully quantized light-matter interaction in the $\mathbf{p} \cdot \mathbf{A}$ and $\mathbf{r} \cdot \mathbf{E}$ gauges can skip the next subsections, and start with Sec. III C directly.

Hamiltonian H_{A+f} in Eq. (1) describes the coupling of the collection of charges in the SAE approximation with the EM field. It is given by the minimal-coupling Hamiltonian describing the interaction of an electron of mass m and charge $q = -e$ with the EM field [96,97,99]

$$H_{A+f} = \sum_\alpha \frac{[\mathbf{p}_\alpha - q\mathbf{A}(\mathbf{r}_\alpha)]^2}{2m} + V_{\mathrm{at}}(\mathbf{r}_\alpha, \mathbf{R}_\alpha), \qquad (16)$$

where $\mathbf{p}_\alpha = m\dot{\mathbf{r}}_\alpha + q\mathbf{A}(\mathbf{r}_\alpha)$ is the canonical conjugate momentum of the electron with coordinate $\mathbf{r}_\alpha$, which obeys $[r_{i\alpha}, p_{j\alpha'}] = i\hbar \delta_{\alpha\alpha'} \delta_{ij}$, and $V_{\mathrm{at}}(\mathbf{r}_\alpha, \mathbf{R}_\alpha)$ is the effective potential felt by the single active electron (see Remark 2 below).

The total Hamiltonian is then of the form

$$H = \frac{1}{2} \int d^3r \left\{ \frac{1}{\epsilon_0} \mathbf{\Pi}^2(\mathbf{r}) + \frac{1}{\mu_0} [\nabla \times \mathbf{A}(\mathbf{r})]^2 \right\}$$
$$+ \sum_\alpha \left[\frac{[\mathbf{p}_\alpha + e\mathbf{A}(\mathbf{r}_\alpha)]^2}{2m} + V_{\mathrm{at}}(\mathbf{r}_\alpha, \mathbf{R}_\alpha) \right], \qquad (17)$$

and will be used for the transformation to the length gauge. Furthermore, at this point we present some remarks that need to be taken into account in the present description.

Remark 1: Note that we are considering here a nonrelativistic theory of electrons interacting with the quantum EM field. Moreover, we consider the dipole approximation. Obviously, the considered model is ultraviolet divergent. This divergence has no physical meaning, and is related partially to the incorrect treatment of large wave vectors in the dipole approximation. It cannot be removed by a satisfactory renormalization procedure, which leads to nonphysical run-away solutions [111,112]. Instead, we introduce a form factor tempering the coupling for high frequencies, just as the $e^{i\mathbf{k}\cdot\mathbf{r}}$ term does. Following Refs. [113,114], we take the form factor

$$g(k) = \frac{\Gamma}{\sqrt{\Gamma^2 + k^2}}, \qquad (18)$$

where the cutoff parameter Γ is much larger than the laser frequency, and is of the order of $\Gamma \simeq d^{-1}$, where d is equal to the characteristic amplitude of the electronic oscillations. With such a choice, the atomic lifetime remains finite, while the frequency (Lamb) shift is linearly divergent as $\Gamma \to \infty$.

Remark 2: The effective potential $V_{\mathrm{at}}(\mathbf{r}_\alpha, \mathbf{R}_\alpha)$ felt by the single active electron in a given atom or molecule centered at $\mathbf{R}_\alpha$, and for neutral atoms, has a long-range tail

corresponding to the Coulomb interaction between the charges, related to the parallel component of the electric field. For any specific atom or molecule, with the exception of atomic hydrogen, it has to be calculated carefully using advanced Hartree-Fock methods [115,116].

B. Transformation to the length gauge

In the following we are interested in localized systems, e.g., atoms or molecules, which are located at a position $\mathbf{R}_\alpha$. Moreover, for the moment, we only consider systems within the SAE approximation. Since we are dealing with localized atomic or molecular systems, in which a single active bound electron is driven by the intense laser field, we further use the fact that the induced polarization is due to the displacement of electrons with charge e, and we can define the polarization via

$$\nabla \cdot \mathbf{P}(\mathbf{r}) = e \sum_\alpha \delta(\mathbf{r} - \mathbf{r}_\alpha). \qquad (19)$$

To describe the interaction of intense laser fields with matter, we transform Hamiltonian (17) into a more convenient form, in which the dipole moment of the electrons

$$\mathbf{d} = \sum_\alpha q_\alpha \mathbf{r}_\alpha = -e \sum_\alpha \mathbf{r}_\alpha \qquad (20)$$

is coupled to the electric field $\mathbf{E}(\mathbf{r})$. We therefore first obtain a multipolar-coupling Hamiltonian by performing a unitary transformation followed by the dipole approximation.

1. Power-Zienau-Woolley transformation

The unitary transformation that turns the minimal-coupling Hamiltonian (17) into the multipolar coupling is given by the Power-Zienau-Woolley (PZW) transformation [96,97,99]

$$T \equiv \exp\left\{\frac{i}{\hbar} \int d^3r \mathbf{P}(\mathbf{r}) \cdot \mathbf{A}(\mathbf{r})\right\}, \qquad (21)$$

where the atomic polarization $\mathbf{P}(\mathbf{r})$ given by

$$\mathbf{P}(\mathbf{r}) = -e \sum_\alpha \int_0^1 ds(\mathbf{r}_\alpha - \mathbf{R}_\alpha)\delta(\mathbf{r} - \mathbf{R}_\alpha - s(\mathbf{r}_\alpha - \mathbf{R}_\alpha)) \qquad (22)$$

solves Eq. (19). The PZW transformation obviously leaves both the vector potential $\mathbf{A}'(\mathbf{r}) = T\mathbf{A}(\mathbf{r})T^\dagger = \mathbf{A}(\mathbf{r})$ and the electron coordinates $\mathbf{r}'_\alpha = T\mathbf{r}_\alpha T^\dagger = \mathbf{r}_\alpha$ invariant. However, the canonical conjugate field momentum $\mathbf{\Pi}(\mathbf{r})$ and the

electron canonical momentum $\mathbf{p}_\alpha$ transform according to

$$\mathbf{\Pi}'(\mathbf{r}) = T\mathbf{\Pi}(\mathbf{r})T^\dagger = \mathbf{\Pi}(\mathbf{r}) - \mathbf{P}_\perp(\mathbf{r}), \qquad (23)$$

$$\mathbf{p}'_\alpha = T\mathbf{p}_\alpha T^\dagger = \mathbf{p}_\alpha + e\mathbf{A}(\mathbf{r}_\alpha)$$
$$+ e \int_0^1 ds\, s(\mathbf{r}_\alpha - \mathbf{R}_\alpha)\{\nabla \times \mathbf{A}(\mathbf{R}_\alpha + s(\mathbf{r}_\alpha - \mathbf{R}_\alpha))\}, \qquad (24)$$

where $\mathbf{P}_\perp(\mathbf{r})$ is the transverse part of the polarization $\mathbf{P}(\mathbf{r})$. We can now express the minimal-coupling Hamiltonian (17) in terms of the new dynamical variables from Eqs. (23) and (24), and we obtain the multipolar-coupling Hamiltonian $H' = THT^\dagger$ (see Appendix B). In this multipolar Hamiltonian we only consider the term in which the transverse displacement field $\mathbf{\Pi}'(\mathbf{r}) = -[\epsilon_0\mathbf{E}_\perp(\mathbf{r}) + \mathbf{P}_\perp(\mathbf{r})]$ is coupled to the atomic polarization $\mathbf{P}(\mathbf{r})$. The terms describing the interaction of the paramagnetic magnetization with the magnetic induction field $\mathbf{B}(\mathbf{r}) = \nabla \times \mathbf{A}(\mathbf{r})$, and the diamagnetic energy of the system, which is quadratic in the magnetic induction field, will be neglected in the following when performing the dipole approximation.

2. Dipole approximation

Since we are considering electrons that are bound by the Coulomb potential V_C to the atomic core at position $\mathbf{R}_\alpha$, we can expand the field variables in powers of $\mathbf{r}_\alpha - \mathbf{R}_\alpha$. Within the electric dipole approximation, we only keep the zeroth-order term, such that the vector potential $\mathbf{A}(\mathbf{R}_\alpha)$ and the canonical conjugate momentum field $\mathbf{\Pi}(\mathbf{R}_\alpha)$ are evaluated at the atomic position $\mathbf{R}_\alpha$. Therefore, the interaction Hamiltonian H'_{int} in the multipolar form simplifies significantly. Since the vector potential loses its spatial dependence in the electric dipole approximation, the last two terms in Eq. (B5) in Appendix B vanish due to $\nabla_{\mathbf{r}_\alpha} \times \mathbf{A}(\mathbf{R}_\alpha) = 0$. Furthermore, the canonical momentum field is evaluated at the atomic position $\mathbf{R}_\alpha$, and we have

$$H'_{\text{int}} = -\mathbf{d} \cdot \mathbf{E}_\perp = e \sum_\alpha \mathbf{r}_\alpha \cdot \mathbf{E}_\perp(\mathbf{R}_\alpha), \qquad (25)$$

where $\mathbf{d} = -e\sum_\alpha \mathbf{r}_\alpha$ is the electric dipole moment for global neutral systems. Now, the total Hamiltonian after the unitary PZW transformation within the dipole approximation has the form

$$H' = \sum_\mu \int d^3k\, \hbar\omega_k\left(a^\dagger_{\mathbf{k}\mu}a_{\mathbf{k}\mu} + \frac{1}{2}\right)$$
$$+ \sum_\alpha \frac{\mathbf{p}^2_\alpha}{2m} + V_{\text{at}}(\mathbf{r}_\alpha, \mathbf{R}_\alpha)$$
$$+ e \sum_\alpha \mathbf{r}_\alpha \cdot \mathbf{E}_\perp(\mathbf{R}_\alpha) + \frac{1}{2\epsilon_0}\int d^3r \mathbf{P}^2_\perp(\mathbf{r}). \qquad (26)$$

3. Renormalization of polarization self-energy

The last term of Eq. (26) is, in our nonrelativistic theory, and within the dipole approximation, strictly speaking infinite. If we use the large momentum cutoff, it becomes regularized, but gives rise to a nonphysical quadratic contribution to the electronic potential. We thus "renormalize" this term as above, including it in the effective potential $\tilde{V}_{at}(\mathbf{r}_\alpha, \mathbf{R}_\alpha)$. The final Hamiltonian in the dipole approximation (sometimes known as the length gauge) reads

$$
H_{dip} = \sum_\mu \int d^3k \, \hbar\omega_k \left(a^\dagger_{\mathbf{k}\mu} a_{\mathbf{k}\mu} + \frac{1}{2} \right)
$$

$$
+ \sum_\alpha \left[\frac{\mathbf{p}^2_\alpha}{2m} + \tilde{V}_{at}(\mathbf{r}_\alpha, \mathbf{R}_\alpha) + e\mathbf{r}_\alpha \cdot \mathbf{E}_\perp(\mathbf{R}_\alpha) \right]. \quad (27)
$$

This Hamiltonian will provide the starting point for further discussion.

C. Dynamical evolution

In this section we obtain the dynamical evolution of the EM field. We therefore solve the time-dependent Schrödinger equation (TDSE) [90,92]

$$
i\hbar \frac{d}{dt} |\psi(t)\rangle = H_{dip} |\psi(t)\rangle \quad (28)
$$

with the Hamiltonian in Eq. (27). To describe intense laser-matter interactions, we assume that the electrons are initially in the ground state $\bigotimes_\alpha |g_\alpha\rangle$ and that the EM field of the laser pulse is described by multimode coherent states $|\alpha_{\mathbf{k}\mu}\rangle$. The spectral profile and wave vector of the laser pulse are centered around ω_L and $\mathbf{k}_L$, respectively, and the field is in the polarization mode μ. All higher frequency modes (i.e., in particular high-harmonic modes) are assumed to be in the vacuum state $|0_{\mathbf{k}\mu}\rangle$ such that the initial condition is given by

$$
|\psi(t_0)\rangle = \bigotimes_\alpha |g_\alpha\rangle \bigotimes_{\mathbf{k},\mu \simeq \mathbf{k}_{L\mu}} |\alpha_{\mathbf{k}\mu}\rangle \bigotimes_{\mathbf{k} \gg \mathbf{k}_L} |0_{\mathbf{k}\mu}\rangle. \quad (29)
$$

We want to emphasize that the coherent state amplitudes $\alpha_{\mathbf{k},\mu}$ of the driving laser source are a function of the field momentum $\mathbf{k}$ and polarization μ, encoding the information of the spectral characteristics of the driving laser. For each frequency mode $\omega_{\mathbf{k},\mu}$, with given polarization μ, the respective amplitude and phase varies. This allows us to consider arbitrary driving field configurations including different frequency or spatial modes, and to include complex polarization states [101]. The magnitude of each mode $|\alpha_{\mathbf{k},\mu}|$ is proportional to the frequency spectrum of the considered EM driving field, and is centered around the driving laser frequency $\omega_{\mathbf{k}_L}$. In Fig. 3 we illustrate the magnitude $|\alpha_{\mathbf{k},\mu}|$ of the spectral decomposition for a driving laser with a sinusoidal squared envelope with $n_{cyc} = 5$
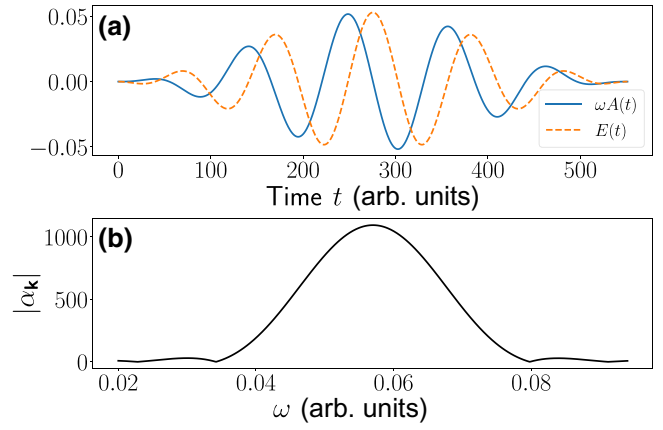
FIG. 3. In (a) we consider a linearly polarized electromagnetic field with a sinusoidal squared envelope, central frequency $\omega = 0.057$ a.u., field amplitude $E = 0.053$ a.u., and $n_{cyc} = 5$ cycles. The orange dashed curve shows the electric field while the blue solid curve the vector potential. In (b) we show the dependence of $|\alpha_{\mathbf{k},\mu}|$ on the frequency mode.

cycles of duration. The spectral amplitude is given by $\alpha_{\mathbf{k},\mu} \propto \int dt \epsilon_{\mathbf{k},\mu} \cdot \mathbf{A}(t) e^{-i\omega_k t}$.

We now solve the TDSE (28) by transforming into the interaction picture with respect to the free-field Hamiltonian H_f such that $|\psi'(t)\rangle = \exp[iH_f t/\hbar] |\psi(t)\rangle$ solves the Schrödinger equation

$$
i\hbar \frac{d}{dt} |\psi'(t)\rangle = \sum_\alpha \left(\frac{\mathbf{p}^2_\alpha}{2m_\alpha} + \tilde{V}_{at}(\mathbf{r}_\alpha, \mathbf{R}_\alpha) \right.
$$

$$
\left. + e\mathbf{r}_\alpha \cdot \mathbf{E}_Q(t, \mathbf{R}_\alpha) \right) |\psi'(t)\rangle, \quad (30)
$$

where the time-dependent electric field operator is now given by

$$
\mathbf{E}_Q(t, \mathbf{R}_\alpha) = i \sum_\mu \int d^3k \, \tilde{g}(k) \epsilon_{k\mu} [a_{k\mu} e^{-i\omega_k t + i\mathbf{k}\cdot\mathbf{R}_\alpha}
$$

$$
- a^\dagger_{k\mu} e^{i\omega_k t - i\mathbf{k}\cdot\mathbf{R}_\alpha}]. \quad (31)
$$

To separate the contribution of the classical electric field from the quantum corrections associated with it, we perform a unitary transformation that shifts the initial coherent state of the field, $\bigotimes_{\mathbf{k},\mu \simeq \mathbf{k}_{L,\mu}} |\alpha_{\mathbf{k}\mu}\rangle$, to the vacuum state. This is performed by applying the displacement operators $D^\dagger(\alpha_k) = D(-\alpha_k)$, such that the new state $|\tilde{\psi}(t)\rangle = \bigotimes_{\mathbf{k},\mu \simeq \mathbf{k}_{L,\mu}} D^\dagger(\alpha_{\mathbf{k},\mu}) |\psi'(t)\rangle$ obeys the Schrödinger equation

$$
i\hbar \frac{d}{dt} |\tilde{\psi}(t)\rangle = \sum_\alpha \left[\frac{\mathbf{p}^2_\alpha}{2m_\alpha} + \tilde{V}_{at}(\mathbf{r}_\alpha, \mathbf{R}_\alpha) - \mathbf{d} \cdot \mathbf{E}_{cl}(t, \mathbf{R}_\alpha) \right.
$$

$$
\left. - \mathbf{d} \cdot \mathbf{E}_Q(t, \mathbf{R}_\alpha) \right] |\tilde{\psi}(t)\rangle \quad (32)
$$

with the new initial condition given by

$$\left|\tilde{\psi}(t_0)\right\rangle = D^\dagger(\alpha_{k_L})\left|\psi(t_0)\right\rangle$$

$$= \bigotimes_\alpha |g_\alpha\rangle \bigotimes_{\mathbf{k},\mu \simeq \mathbf{k}_L\mu} |0_{\mathbf{k}\mu}\rangle \bigotimes_{\mathbf{k}\gg\mathbf{k}_L} |0_{\mathbf{k}\mu}\rangle. \quad (33)$$

The classical part of the electric field is given by

$$\mathbf{E}_{\mathrm{cl}}(t,\mathbf{R}_\alpha) = i\sum_\mu \int d^3k\,\tilde{g}(k)\epsilon_{k\mu}[\alpha_{k,\mu}(k)e^{-i\omega_k t+i\mathbf{k}\cdot\mathbf{R}_\alpha}$$

$$- \alpha_{k,\mu}^*(k)e^{i\omega_k t-i\mathbf{k}\cdot\mathbf{R}_\alpha}], \quad (34)$$

where $\tilde{g}(k) = g(k)\sqrt{\hbar ck/(2\epsilon_0(2\pi)^3)}$ with $g(k)$ from Eq. (18), and the quantum part $\mathbf{E}_Q(t)$ is given by Eq. (31). The dependence of the amplitude $\alpha_{\mathbf{k}\mu}(k)$ of mode $\{\mathbf{k},\mu\}$ on the field momentum takes into account the spectral distribution of the driving laser field, as shown in Fig. 3(b). By virtue of the separation of the classical and quantum parts of the electric field, the semiclassical strong-field Hamiltonian appears in Eq. (32), i.e.,

$$H_{\mathrm{sc}}(t) = \sum_\alpha \left[\frac{\mathbf{p}_\alpha^2}{2m} + \tilde{V}(\mathbf{r}_\alpha,\mathbf{R}_\alpha) + e\mathbf{r}_\alpha \cdot \mathbf{E}_{\mathrm{cl}}(t,\mathbf{R}_\alpha)\right]. \quad (35)$$

We therefore transform the atomic variables into the interaction picture with respect to the semiclassical Hamiltonian $H_{\mathrm{sc}}(t)$ by applying the unitary transformation $U_{\mathrm{sc}}(t) = \mathcal{T}\exp[-i\int_{t_0}^t H_{\mathrm{sc}}(t')dt']$ with the time-ordering operator $\mathcal{T}$ such that the state $|\Psi(t)\rangle \equiv U_{\mathrm{sc}}^\dagger(t)|\tilde{\psi}(t)\rangle$ solves the Schrödinger equation

$$i\hbar\frac{d}{dt}|\Psi(t)\rangle = e\sum_\alpha \mathbf{r}_\alpha(t) \cdot \mathbf{E}_Q(t,\mathbf{R}_\alpha)|\Psi(t)\rangle, \quad (36)$$

where $\mathbf{r}_\alpha(t) = U_{\mathrm{sc}}^\dagger(t)\mathbf{r}_\alpha U_{\mathrm{sc}}(t)$ is the dipole moment operator in the interaction picture with respect to the semiclassical Hamiltonian. Note that this expression is still exact and no approximations have been performed so far [based on the approximate Hamiltonian in Eq. (27)]. To describe the different processes in strong-field physics, such as HHG or ATI, we use the Schrödinger equation of Eq. (36) as the starting point for the respective discussions, and approximations compatible with the strong-field processes will be applied from here on. This will serve as the origin for the light engineering protocols in intense laser-matter interactions, which will be introduced in the subsequent sections.

IV. QUANTUM STATE ENGINEERING USING INTENSE LASER FIELDS

The description of the dynamical evolution of the total system, formed by many electrons, with the EM field

has, thus far, been exact under the Hamiltonian within the dipole approximation. This interaction will entangle the electronic and EM field states [93], and many different processes can occur (see the Introduction). To engineer the photonic degree of freedom for generating nonclassical states of light, we can now perform specific operations on the total state. For instance, we can condition the total evolution on certain electronic states, such as the ground state or a continuum state, which corresponds to the process of HHG or ATI, respectively. The conditional evolution of the EM field modes then allows us to apply approximations based on assumptions in agreement with intense laser-matter interaction.

For instance, it was shown that the EM field state is in an entangled state between all the field modes [91,93], which then further allows us to perform a second stage of conditioning by measuring particular field modes leading to a quantum operation acting on the remaining modes [93]. This will, for instance, generate high-photon-number optical "catlike" states in the infrared (IR) [90,92] or extreme ultraviolet (XUV) regime [91]. Those measurements provide access to the nonclassical character of the entangled state.

In the following we introduce these aspects with the prospect to engineer the quantum state of the EM field.

A. Conditioning on the electronic ground state: HHG

To describe the process of high-harmonic generation in atomic systems, we consider only those cases in which the electron is found in its ground state, leading to the emission of radiation of high-order harmonics of the driving frequency. We therefore project TDSE (36) onto the electronic ground state of all atoms $\bigotimes_\alpha |g_\alpha\rangle$ in the original laboratory frame, such that

$$i\hbar\frac{d}{dt}|\phi(t)\rangle = e\sum_\alpha \mathbf{E}_Q(t,\mathbf{R}_\alpha) \cdot \langle g\cdots g|\mathbf{r}_\alpha(t)|\Psi(t)\rangle, \quad (37)$$

where we have defined the EM field state conditioned on the electronic ground state $|\phi(t)\rangle = \langle g\cdots g|\Psi(t)\rangle$. To simplify the right-hand side, we introduce the identity in the spirit of the SFA by neglecting excited electronic bound states

$$I = \bigotimes_\alpha \left(|g_\alpha\rangle\langle g_\alpha| + \int d^3v_\alpha |\mathbf{v}_\alpha\rangle\langle \mathbf{v}_\alpha|\right), \quad (38)$$

where we have denoted the continuum states as $|\mathbf{v}_\alpha\rangle$ corresponding to an electron with kinetic momentum $m\mathbf{v}$. We

then obtain

$$i\hbar\frac{d}{dt}|\phi(t)\rangle = e\sum_\alpha \langle\mathbf{r}_\alpha(t)\rangle \cdot \mathbf{E}_Q(t,\mathbf{R}_\alpha)|\phi(t)\rangle$$
$$+ e\sum_\alpha \int d^3v_\alpha \langle g_\alpha|\mathbf{r}_\alpha(t)|\mathbf{v}_\alpha\rangle$$
$$\cdot \mathbf{E}_Q(t,\mathbf{R}_\alpha)|\phi_\alpha(\mathbf{v}_\alpha,t)\rangle, \qquad (39)$$

where $\langle\mathbf{r}_\alpha(t)\rangle = \langle g|\mathbf{r}_\alpha(t)|g\rangle$ is the time-dependent dipole moment expectation value in the electronic ground state, and we have defined the state of the EM field with one electron conditioned on a continuum state $|\phi_\alpha(\mathbf{v}_\alpha,t)\rangle = \langle\mathbf{v}_\alpha g\cdots g|\Psi(t)\rangle$. For the process of HHG, we neglect the second term corresponding to the projection of the total state onto an electronic continuum state, which is hardly occupied at the end of the pulse since the electron recombines to its ground state during the process of HHG. However, note that this approximation neglects the continuum population at all times, and not only at the end of the pulse, though this contribution is assumed to be small compared to the ground-state amplitude [117]. We can thus proceed and solve

$$i\hbar\frac{d}{dt}|\phi(t)\rangle = e\sum_\alpha \langle\mathbf{r}_\alpha(t)\rangle \cdot \mathbf{E}_Q(t,\mathbf{R}_\alpha)|\phi(t)\rangle. \qquad (40)$$

Since the field operator is linear in the creation and annihilation operators, we can solve the TDSE exactly and obtain, for the propagator,

$$U(t,t_0) = \mathcal{T}\exp\left\{-\frac{ie}{\hbar}\int_{t_0}^t dt'\sum_\alpha \langle\mathbf{r}_\alpha(t')\rangle\cdot\mathbf{E}_Q(t',\mathbf{R}_\alpha)\right\}$$
$$= \prod_{\mathbf{k}\mu} D[\chi_{\mathbf{k},\mu}(t)]e^{i\varphi_{\mathbf{k},\mu}(t)}, \qquad (41)$$

which is equivalent to a multimode displacement operator, where

$$\varphi_{\mathbf{k},\mu}(t) = \frac{e^2}{\hbar^2}\tilde{g}^2(k)\sum_{\alpha,\alpha'}\int_{t_0}^t dt_1\int_{t_0}^{t_1} dt_2\epsilon_{\mathbf{k}\mu}\cdot\langle\mathbf{r}_\alpha(t_1)\rangle\epsilon_{\mathbf{k}\mu}$$
$$\cdot\langle\mathbf{r}_{\alpha'}(t_2)\rangle\sin[\omega_k(t_1-t_2)]. \qquad (42)$$

Thus, the initial state of the field, up to a phase factor, after the interaction is given by

$$|\phi(t)\rangle = \prod_{\mathbf{k},\mu} D[\chi_{\mathbf{k},\mu}(t)]|\phi(t_0)\rangle$$
$$= \mathcal{D}[\boldsymbol{\chi}(t)]|\phi(t_0)\rangle, \qquad (43)$$

where $\mathcal{D}[\boldsymbol{\chi}(t)]$ is shorthand notation for the product of all displacement operators $D[\chi_{\mathbf{k},\mu}(t)]$ on the field modes, each

of which shifts the initial state of the respective mode by an amplitude

$$\chi_{\mathbf{k},\mu}(t) = -e\sum_\alpha \tilde{g}(k)e^{-i\mathbf{k}\cdot\mathbf{R}_\alpha}\int_{t_0}^t d\tau\epsilon_{\mathbf{k}\mu}\cdot\langle\mathbf{r}_\alpha(\tau)\rangle e^{i\omega_k\tau}. \qquad (44)$$

To obtain the field state in the original laboratory frame, we have to undo the transformations in Eqs. (30) and (32),

$$|\Phi(t)\rangle = \prod_{\mathbf{k},\mu\simeq\mathbf{k}_{L,\mu}} D(\alpha_{\mathbf{k},\mu})e^{-(i/\hbar)H_f t}|\phi(t)\rangle, \qquad (45)$$

and we obtain

$$|\Phi(t)\rangle = \bigotimes_{\mathbf{k},\mu\simeq\mathbf{k}_{L,\mu}} e^{i\varphi_{\mathbf{k},\mu}(t)}\left|[\alpha_{\mathbf{k},\mu}+\chi_{\mathbf{k},\mu}(t)]e^{-i\omega_\mathbf{k}t}\right\rangle$$
$$\bigotimes_{\mathbf{k},\mu\gg\mathbf{k}_{L,\mu}} \left|\chi_{\mathbf{k},\mu}(t)e^{-i\omega_\mathbf{k}t}\right\rangle, \qquad (46)$$

where

$$\varphi_{\mathbf{k},\mu}(t) = \text{Im}[\alpha_{\mathbf{k},\mu}\chi_{\mathbf{k},\mu}^*(t)]. \qquad (47)$$

To obtain the spectrum of scattered light, i.e., the HHG spectrum, we note that in our treatment the interatomic correlations of the dipole moment are neglected [93,118] and that the spectrum is solely governed by the coherent part due to the classical charge current of the dipole moment expectation value (see the physical explanation of the generation of coherent states from classical charge currents in Sec. II B). It should be noted that, due to this approximation, e.g., neglecting the continuum contribution in Eq. (39) that is only valid for a small depletion of the ground state, the final state of the total EM field is given by coherent product states in Eq. (46). This can also be seen from the point of view that only the dipole moment expectation value is coupled to the field [see Eq. (40)], acting as a classical charge current, and all dipole moment correlations are neglected [93,118]. Terms including higher orders of $\mathbf{E}_Q(t)$ would lead, for instance, to squeezing in the field modes. The coherent contribution to the HHG spectrum is proportional to (see Appendix C)

$$S(\omega_{\mathbf{k},\mu}) \propto \lim_{t\to\infty}|\chi_{\mathbf{k},\mu}(t)|^2 = \tilde{g}(k)^2 N^2|\epsilon_{\mathbf{k},\mu}\cdot\langle\mathbf{d}(\omega_\mathbf{k})\rangle|^2. \qquad (48)$$

We observe that the HHG spectrum is proportional to the Fourier components of the time-dependent dipole moment expectation value, which is in agreement with the results obtained when neglecting the correlations of the dipole moment operator [118]. In Fig. 4 we show the HHG spectrum given by Eq. (48) for a linearly polarized driving field
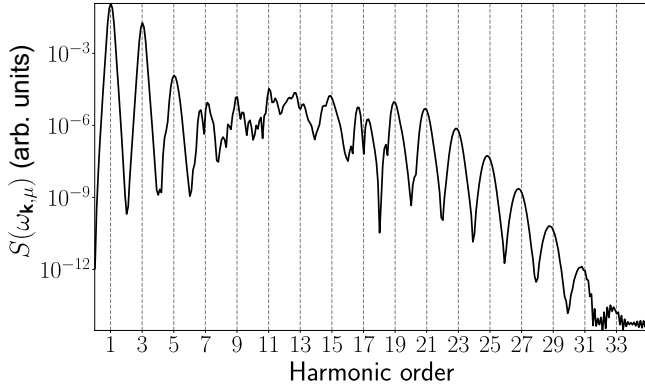
FIG. 4. High-harmonic generation spectrum obtained from the evaluation of Eq. (48) using the QPROP software [119], when a hydrogen atom in the ground state ($I_p = 0.5$ a.u.) interacts with a linearly polarized electromagnetic field with a sinusoidal squared envelope that has ten cycles, driving frequency $\omega = 0.057$ a.u., and electric field amplitude $E = 0.053$ a.u. The harmonic yield extends until the 21st harmonic, which constitutes the cutoff frequency of the spectrum, that is, the maximum energy that can be gained by the electron when accelerating in the continuum.

with a sinusoidal squared envelope and $n_{\text{cyc}} = 10$ cycles. We observe the usual features of a HHG spectrum from linearly polarized, single color driving fields, namely that the peaks of the spectrum are located at the odd harmonics of the fundamental driving frequency, and that the spectrum exhibits a plateau structure that lasts until the cutoff region, here located around the 21st harmonic order. This cutoff frequency corresponds to the maximum kinetic energy that can be gained by the electron within the field [117]. We note that, by controlling the properties of the employed laser field (intensity, polarization, wavelength, etc.) as well as the atomic species used in the interaction region, the extension of the harmonic plateau can be further increased.

B. Conditioning on harmonic field modes

Thus far, we have presented the first step of conditioning, in which the postselection was performed on the electronic degree of freedom, i.e., the electronic ground state, corresponding to the process of HHG. In the next conditioning step for quantum state engineering of light, we perform measurements on the EM field itself. In particular, we perform a conditioning measurement on the harmonic field modes, leading to optical "catlike" states in the fundamental driving laser mode.

As a consequence of the nonlinear interaction with the electron, the fundamental and harmonic modes get shifted by a quantity $\chi_{\mathbf{k},\mu}$, which depends on the time-dependent dipole moment of the electron and correlates the shift obtained in each of the modes. In fact, the mode that gets excited during the HHG process that takes into account all these correlations is given by the corresponding number states $|\tilde{n}\rangle$. Thus, the HHG process corresponds to the case

in which these wavepacket modes get excited, i.e., whenever $\tilde{n} \neq 0$. This allows us to introduce a set of positive operator-valued measure (POVM) [120] considering these two events [93]

$$\mathcal{A}_{\tilde{n}} = \{\Pi_{\tilde{0}}, \Pi_{\tilde{n} \neq 0}\}, \tag{49}$$

where $\Pi_{\tilde{0}} = |\tilde{0}\rangle\langle\tilde{0}|$ considers the case where no harmonic radiation is emitted and $\Pi_{\tilde{n} \neq 0} = \sum_{\tilde{n} \neq 0} |\tilde{n}\rangle\langle\tilde{n}|$ considers the case where the wavepacket mode is excited, i.e., harmonic radiation is generated. Note that the states $|\tilde{n}\rangle$ are the number states of the HHG wavepacket mode, and thus, by definition, all possible excitations sum to the identity, i.e., $\Pi_{\tilde{0}} + \Pi_{\tilde{n} \neq 0} = \mathbb{1}$. Having in mind that the vacuum state of this wavepacket mode $|\tilde{0}\rangle$ state coincides with the state of the field prior to the interaction, i.e., the quantum state of the field modes in Eq. (29), the conditioning on the case where harmonics are generated can be written as $\Pi_{\tilde{n} \neq 0} = \mathbb{1} - \Pi_{\tilde{0}}$. Applying this operation to the state in Eq. (46), we obtain

$$\begin{aligned}
\big|\tilde{\Phi}(t)\big\rangle = &\bigotimes_{\mathbf{k},\mu \simeq \mathbf{k}_{L,\mu}} e^{i\varphi_{\mathbf{k},\mu}(t)} \big|[\alpha_{\mathbf{k},\mu} + \chi_{\mathbf{k},\mu}(t)]e^{-i\omega_k t}\big\rangle \\
&\bigotimes_{\mathbf{k},\mu \gg \mathbf{k}_{L,\mu}} \big|\chi_{\mathbf{k},\mu}(t)e^{-i\omega_k t}\big\rangle \\
&- \bigotimes_{\mathbf{k},\mu \simeq \mathbf{k}_{L,\mu}} \xi_{\text{IR}} e^{i\varphi_{\mathbf{k},\mu}(t)} \big|\alpha_{\mathbf{k},\mu}e^{-i\omega_k t}\big\rangle \\
&\bigotimes_{\mathbf{k},\mu \gg \mathbf{k}_{L,\mu}} \xi_{\text{HH}} \big|0_{\mathbf{k},\mu}\big\rangle, \tag{50}
\end{aligned}$$

where ξ_{IR} and ξ_{HH} are the overlaps between the initial state and the state we condition on, and are given by

$$\xi_{\text{IR}} = \prod_{\mathbf{k},\mu \simeq \mathbf{k}_{L,\mu}} \big\langle\alpha_{\mathbf{k},\mu}e^{-i\omega_k t}\big|[\alpha_{\mathbf{k},\mu} + \chi_{\mathbf{k},\mu}(t)]e^{-i\omega_k t}\big\rangle, \tag{51}$$

$$\xi_{\text{HH}} = \prod_{\mathbf{k},\mu \gg \mathbf{k}_{L,\mu}} \big\langle 0_{\mathbf{k},\mu}\big|\chi_{\mathbf{k},\mu}(t)e^{-i\omega_k t}\big\rangle. \tag{52}$$

The final state obtained in Eq. (50) is an entangled state, heralded by the emission of harmonic radiation, between all the field modes that get excited during the HHG process, and thus includes all the harmonic modes up to the cutoff frequency given by the harmonic spectrum. The harmonic cutoff depends on the driving laser field parameters, and the atomic species used for the HHG process [121]. Furthermore, the amount of entanglement in the obtained state depends on the shift $\chi_{\mathbf{k},\mu}$ [91], which can be controlled by means of the gas density in the interaction region [92]. In Refs. [90,92], the states in Eq. (50) were used to generate a coherent state superposition in the driving laser mode. The implemented scheme introduced a measurement where the radiation obtained in the

harmonic modes was anticorrelated with the depletion obtained in the fundamental modes (see Sec. V for further details). In the present analysis, this measurement corresponds to a projective operation onto the harmonic modes, i.e., $|\tilde{\Phi}_{\mathbf{k}_{L,\mu}}\rangle = \prod_{\mathbf{k},\mu \gg \mathbf{k}_{L,\mu}} \langle \chi_{\mathbf{k},\mu}|\tilde{\Phi}(t)\rangle$, such that the state of the fundamental mode is given by

$$|\tilde{\Phi}_{\mathbf{k}_{L,\mu}}\rangle = \bigotimes_{\mathbf{k},\mu \simeq \mathbf{k}_{L,\mu}} \left|[\alpha_{\mathbf{k},\mu} + \chi_{\mathbf{k},\mu}(t)]e^{-i\omega_k t}\right\rangle$$
$$- \bigotimes_{\mathbf{k},\mu \simeq \mathbf{k}_{L,\mu}} \xi_{\text{IR}}|\xi_{\text{HH}}|^2 \left|\alpha_{\mathbf{k},\mu}e^{-i\omega_k t}\right\rangle, \qquad (53)$$

which represents a coherent state superposition (CSS) between two overlapping coherent states. This superposition state has the particular form of two overlapping coherent states, i.e., two coherent states that are not too much separated in phase space, and can change from optical "catlike" to "kittenlike" states depending on the parameter $\chi_{\mathbf{k}_L}$ [92]. It is important to note that the distance between the two states in the superposition cannot be too large since, for increasing $\chi_{\mathbf{k}_L}$, the overlap ξ_{IR} would decrease [see Eq. (51)], and thus the second term in the superposition would vanish. However, this also brings an advantage for practical purposes, since traditional cat states are much more fragile against decoherence such as losses for increasing separation of the two states [122]. A fate the CSS generated from strong laser fields does not experience. Furthermore, this particular property allows this catlike state to grow in size by increasing the amplitude $\alpha_{\mathbf{k}_L}$, leading to high-photon-number coherent state superpositions orders of magnitude higher than current schemes [91–93]. Those CSS show prominent nonclassical features in their respective Wigner function (see Sec. V B 4), showing the close analogy to optical cat states. An analysis of the properties, such as photon statistics and different non-classicality measures, of a CSS of this form can be found in Ref. [123].

Similarly, one can instead perform the projective operation over the driving field mode, and all the harmonic modes except that in mode $(\mathbf{k}, \mu)$. This operation allows one to obtain coherent state superpositions that belong to the XUV region [91]

$$|\tilde{\Phi}_{\mathbf{k},\mu}\rangle = \left|\xi_{\mathbf{k},\mu}e^{-i\omega_k t}\right\rangle - \xi_{\mathbf{k},\mu}\left(\prod_{\mathbf{k}',\mu' \neq \mathbf{k},\mu} |\xi_{\mathbf{k}',\mu'}|^2\right)|0_{\mathbf{k},\mu}\rangle, \qquad (54)$$

where $\xi_{\mathbf{k}',\mu'} = \langle \alpha_{\mathbf{k}',\mu'}e^{-i\omega_{k'}t}|[\alpha_{\mathbf{k}',\mu'} + \chi_{\mathbf{k}',\mu'}(t)]e^{-i\omega_{k'}t}\rangle$ if $\mathbf{k}'$, $\mu' \simeq \mathbf{k}_{L,\mu}$ and equal to $\langle 0_{\mathbf{k}',\mu'}|\chi_{\mathbf{k}',\mu'}(t)e^{-i\omega_{k'}t}\rangle$ otherwise. To relate the formal approach of this subsection to the actual experiment in which an optical "catlike" CSS of the form (53) was measured [90], we summarize the conditioning procedure introduced in this section. We first projected the

evolution of the total system in Eq. (37) onto the electronic ground state for taking into account the process of HHG. We then conditioned the shifted optical field state on the HHG wavepacket modes via projecting state (46) onto $\Pi_{\tilde{n} \neq 0} = \mathbb{1} - \Pi_{\tilde{0}}$. This measurement operation leads to the entangled field state, e.g., wave function "collapse," into state (50). This does not affect the HHG dynamics itself, but formally conditions the field state onto the process of HHG. Finally, the harmonic field modes are detected, and thus the total entangled state is projected onto the respective coherent states of all harmonic modes that are shifted by the respective harmonic amplitudes $\chi_{\mathbf{k}\cdot\mu}$. This leads to the CSS as written in Eq. (53), and which was reconstructed in Ref. [90]. The actual experimental conditioning on HHG has its formal description by the sequence of these three measurements, and is derived in terms of a quantum theory of measurement via POVM in Ref. [93]. In simple terms, the conditioning leads to a projection on everything that was not in the initial field state $|\alpha_{\mathbf{k}_L}\rangle$, i.e., $\mathbb{1} - |\alpha_{\mathbf{k}_L}\rangle\langle\alpha_{\mathbf{k}_L}|$, the identity subtracted by the initial state.

C. Conditioning on electronic continuum states: ATI

1. Optical field state conditioned on ATI

In the following we are interested in describing the process of above-threshold ionization (ATI) in which the electron is found in the continuum after the end of the pulse. We therefore project the TDSE (36) onto the electronic state where one electron is found in a continuum state $|\mathbf{v}_\alpha\rangle$, and the other atoms are in the ground state

$$i\hbar\frac{d}{dt}|\phi_\alpha(\mathbf{v}_\alpha, t)\rangle = e\sum_{\alpha'} \mathbf{E}_Q(t, \mathbf{R}_{\alpha'})$$
$$\cdot \langle \mathbf{v}_\alpha g \cdots g| \, \mathbf{r}_{\alpha'}(t) \, |\Psi(t)\rangle, \qquad (55)$$

where we have defined $|\phi_\alpha(\mathbf{v}_\alpha, t)\rangle = \langle \mathbf{v}_\alpha g \cdots g| \, |\Psi(t)\rangle$. We again use the identity (38) to obtain

$$i\hbar\frac{d}{dt}|\phi_\alpha(\mathbf{v}_\alpha, t)\rangle$$
$$= e\mathbf{E}_Q(t, \mathbf{R}_\alpha) \cdot \langle \mathbf{v}_\alpha| \, \mathbf{r}_\alpha(t) \, |g\rangle \, |\phi(t)\rangle + e\mathbf{E}_Q(t, \mathbf{R}_\alpha)$$
$$\cdot \int d^3 v'_\alpha \, \langle \mathbf{v}_\alpha| \, \mathbf{r}_\alpha(t) \, |\mathbf{v}'_\alpha\rangle \, |\phi_\alpha(\mathbf{v}'_\alpha, t)\rangle$$
$$+ e\sum_{\alpha' \neq \alpha} \mathbf{E}_Q(t, \mathbf{R}_{\alpha'}) \cdot \Bigg[\langle \mathbf{r}_{\alpha'}(t)\rangle \, |\phi_\alpha(\mathbf{v}_\alpha, t)\rangle$$
$$+ \int d^3 v'_{\alpha'} \, \langle g| \, \mathbf{r}_{\alpha'}(t) \, |\mathbf{v}'_{\alpha'}\rangle \, |\phi_{\alpha,\alpha'}(\mathbf{v}_\alpha, \mathbf{v}'_{\alpha'}, t)\rangle\Bigg]. \qquad (56)$$

Here, we have defined the field state conditioned on ionization of two atoms $|\phi_{\alpha,\alpha'}(\mathbf{v}_\alpha, \mathbf{v}'_{\alpha'}, t)\rangle = \langle \mathbf{v}_\alpha \mathbf{v}'_{\alpha'} g \cdots g| \, |\Psi(t)\rangle$. In the following, we only take into account the single-atom response such that we can neglect all terms in which

$\alpha' \neq \alpha$, i.e., we neglect the last two terms in Eq. (56). Note that if one would include the sum over α' of the remaining $N-1$ atoms, this gives rise to a strongly correlated many-body system, and should be considered when many-body phenomena are investigated. We are first interested in the process of direct ATI such that we neglect the contributions from scattering events at the ionic potential after ionization. The time-dependent continuum-continuum transition matrix elements $\langle \mathbf{v}_\alpha | \mathbf{r}_\alpha(t) | \mathbf{v}'_\alpha \rangle$ of the electronic degrees of freedom can be written as (see Appendix D 3)

$$\langle \mathbf{v} | \mathbf{r}(t) | \mathbf{v}' \rangle \simeq \int d^3 v'' \int d^3 v''' b_{\mathbf{v}}^*(\mathbf{v}'',t) b_{\mathbf{v}'}(\mathbf{v}''',t) \langle \mathbf{v}'' | \mathbf{r} | \mathbf{v}''' \rangle, \tag{57}$$

where (see Appendix D 1)

$$b_{\mathbf{v}}(\mathbf{v}',t) = \exp\left\{ -\frac{i}{\hbar} S(\mathbf{v}',t,t_0) \right\} \delta(\mathbf{v}-\mathbf{v}') \tag{58}$$

is the amplitude of a continuum state with momentum $\mathbf{v}'$ when initially having momentum $\mathbf{v}$, and where we have defined the action

$$S(\mathbf{v}',t,t_0) = \int_{t_0}^{t} dt' \left[\frac{1}{2m} \left(m\mathbf{v}' - \frac{e}{c}\mathbf{A}(t) + \frac{e}{c}\mathbf{A}(t') \right)^2 + I_p \right]. \tag{59}$$

The transition matrix element in Eq. (57) is given by

$$e\langle \mathbf{v}'' | \mathbf{r} | \mathbf{v}''' \rangle = ie\hbar \nabla_{\mathbf{v}''} \delta(\mathbf{v}'' - \mathbf{v}''') - \hbar \mathbf{g}(\mathbf{v}'', \mathbf{v}'''), \tag{60}$$

where the first and second terms contribute to direct and rescattering ATI, respectively. In the following we only consider the first term, which is the contribution not influenced by the scattering center, and neglect the rescattering transition matrix element $\mathbf{g}(\mathbf{v}'', \mathbf{v}''')$. It therefore remains to solve

$$i\hbar \frac{d}{dt} |\phi_\alpha(\mathbf{v}_\alpha,t)\rangle = e\mathbf{E}_Q(t,\mathbf{R}_\alpha) \cdot \Delta \mathbf{r}_\alpha(t,\mathbf{v}_\alpha) |\phi_\alpha(\mathbf{v}_\alpha,t)\rangle$$
$$+ e\mathbf{E}_Q(t,\mathbf{R}_\alpha) \cdot \langle \mathbf{v}_\alpha | \mathbf{r}_\alpha(t) | g \rangle |\phi(t)\rangle \tag{61}$$

with the total displacement of the electron in terms of the canonical momentum $\mathbf{p}_\alpha = m\mathbf{v}_\alpha - e\mathbf{A}(t)/c$, given by

$$\Delta \mathbf{r}_\alpha(t,\mathbf{v}_\alpha) = \frac{1}{m} \int_{t_0}^{t} dt' \left[\mathbf{p}_\alpha + \frac{e}{c}\mathbf{A}(t') \right]. \tag{62}$$

The right-hand side of Eq. (61) is decomposed into two terms. The first term is the homogeneous part of the differential equation in which the electric field operator is coupled to the total displacement of the electron during its propagation in the continuum $\Delta \mathbf{r}_\alpha(t,\mathbf{v}_\alpha)$. This takes

into account the backaction of the electron's motion in the continuum over the EM field. In the second term, the electric field is coupled to the transition matrix element from the ground state to the continuum state, which takes into account the effect of ionization. The solution of Eq. (61) is given by

$$|\phi_\alpha(\mathbf{v}_\alpha,t)\rangle = \frac{-ie}{\hbar} \int_{t_0}^{t} dt_1 \mathcal{T} e^{-(ie/\hbar) \int_{t_1}^{t} dt' \mathbf{E}_Q(t',\mathbf{R}_\alpha) \Delta \mathbf{r}_\alpha(t',\mathbf{v}_\alpha)}$$
$$\times \mathbf{E}_Q(t_1,\mathbf{R}_\alpha) \langle \mathbf{v}_\alpha | \mathbf{r}_\alpha(t_1) | g \rangle |\phi(t_1)\rangle, \tag{63}$$

where we have used the initial condition that the electron is initially in the ground state, i.e., $|\phi_\alpha(\mathbf{v}_\alpha,t_0)\rangle = \langle \mathbf{v}_\alpha g \cdots g | \Psi(t_0) \rangle = 0$. However, the homogeneous part of the differential equation (63) adds an important contribution to the total solution, namely, the displacement of the field due to the electron's propagation in the continuum. The exponential term in Eq. (63) can be solved analytically since it is linear in the field operators, and gives rise to a multimode displacement operator

$$\mathcal{T} \exp\left\{ -\frac{ie}{\hbar} \int_{t_1}^{t} dt' \Delta \mathbf{r}_\alpha(t',\mathbf{v}_\alpha) \cdot \mathbf{E}_Q(t',\mathbf{R}_\alpha) \right\}$$
$$= \prod_{\mathbf{k},\mu} D[\delta_\alpha(t,t_1,\omega_k,\mathbf{v}_\alpha)] e^{i\varphi_{\mathbf{k}\mu}(t,t_1,\mathbf{v}_\alpha)}$$
$$= \mathcal{D}[\boldsymbol{\delta}(t,t_1,\mathbf{v}_\alpha)], \tag{64}$$

where $\mathcal{D}[\boldsymbol{\delta}(t,t_1,\mathbf{v}_\alpha)]$ is a shorthand notation for the product over all modes with displacement operators $D[\delta_\alpha(t,t_1,\omega_k,\mathbf{v}_\alpha)]$ for which we have

$$\delta_\alpha(t,t_1,\omega_k,\mathbf{v}_\alpha) = -\frac{e}{\hbar}\tilde{g}(k)e^{-i\mathbf{k}\cdot\mathbf{R}_\alpha} \boldsymbol{\epsilon}_{\mathbf{k}\mu} \cdot \Delta \tilde{\mathbf{r}}_\alpha^*(t,t_1,\omega_k,\mathbf{v}_\alpha), \tag{65}$$

$$\varphi_{\mathbf{k}\mu}(t,t_1,\mathbf{v}_\alpha) = \frac{e^2}{\hbar^2}\tilde{g}^2(k) \int_{t_1}^{t} d\tau_1 \int_{t_1}^{\tau_1} d\tau_2 \boldsymbol{\epsilon}_{\mathbf{k}\mu}$$
$$\cdot \Delta \mathbf{r}_\alpha(\tau_1,\mathbf{v}_\alpha) \boldsymbol{\epsilon}_{\mathbf{k}\mu}$$
$$\times \Delta \mathbf{r}_\alpha(\tau_2,\mathbf{v}_\alpha) \sin[\omega_k(\tau_1-\tau_2)], \tag{66}$$

with the Fourier transform of the electron displacement

$$\Delta \tilde{\mathbf{r}}_\alpha(t,t_1,\omega_k,\mathbf{v}_\alpha) = \int_{t_1}^{t} dt' e^{i\omega_k t'} \Delta \mathbf{r}_\alpha(t',\mathbf{v}_\alpha). \tag{67}$$

Finally, the state of the EM field conditioned on ATI is given by

$$|\phi_\alpha(\mathbf{v}_\alpha,t)\rangle = \frac{-ie}{\hbar} \int_{t_0}^{t} dt_1 \mathcal{D}[\boldsymbol{\delta}(t,t_1,\mathbf{v}_\alpha)] \mathbf{E}_Q(t_1,\mathbf{R}_\alpha)$$
$$\cdot \langle \mathbf{v}_\alpha | \mathbf{r}_\alpha(t_1) | g \rangle \mathcal{D}[\boldsymbol{\chi}(t_1)] |\phi(t_0)\rangle. \tag{68}$$

The time-dependent transition matrix element from the ground state to the continuum state is given by (see

Appendix D 2)

$$\langle \mathbf{v}_\alpha | \, \mathbf{r}_\alpha(t_1) \, |g\rangle \simeq \left\langle \mathbf{p}_\alpha + \frac{e}{c} \mathbf{A}(t_1) \middle| \, \mathbf{r}_\alpha \, |g\rangle \exp \left\{ \frac{i}{\hbar} \int_{t_0}^{t_1} dt' \right.$$

$$\left. \times \left[\frac{1}{2m} \left(\mathbf{p}_\alpha + \frac{e}{c} \mathbf{A}(t') \right)^2 + I_p \right] \right\}. \quad (69)$$

The state of the EM field (68), conditioned on ATI, has an illustrative interpretation in terms of the backaction on the field due to the electron dynamics. The initial state of the field $|\phi(t_0)\rangle$ is displaced by the oscillation of the electron in the ground state [124] via $\mathcal{D}[\chi_{\mathbf{k}\mu}]$ acting until ionization time t_1, when the electron transitions from the ground state to the continuum state. These bound state oscillations have a natural formulation in the Kramers-Henneberger frame, where their contribution to HHG has been estimated [124]. The transition matrix element $\langle \mathbf{v}_\alpha | \, \mathbf{r}_\alpha(t_1) \, |g\rangle$, which includes the phase of the semiclassical action, induces a change of the field due to its coupling to the electric field operator at ionization time t_1. Once the electron is ionized, it propagates in the continuum under the influence of the field. The backaction on the EM field due to the electron's dynamics in the continuum is reflected in the displacement $\mathcal{D}[\boldsymbol{\delta}_\alpha(t, t_1, \omega_k, \mathbf{v}_\alpha)]$. This shift of the individual EM field modes is proportional to the respective Fourier component of the electron displacement in the continuum (67). In the latter contribution, in contrast to the bound state oscillation, the electron does not only oscillate, but also has a drift since it can appear in the continuum with a nonvanishing momentum $\mathbf{p}$. The fact that this induces a displacement in the optical field can intuitively be understood when recalling that a propagating electron in the continuum is the same as a classical charge current, and thus, when coupled to the field operator, induces a coherent displacement. In Fig. 5 we show the behavior of the absolute value of the different displacements for different modes of the EM field (n_{harm}) at the end of the pulse $t = T$ for varying ionization time t_1. We can see that the largest contribution to the shift on the initial field states is due to the electron displacement in the continuum via $\delta(T, t_1, \omega_k, \mathbf{p})$ [see Figs. 5(b) and 5(c)], as would be expected for the process of ATI. The contribution from the bound state oscillation prior to ionization is, at least, 2 orders of magnitude smaller than the continuum contribution [see Fig. 5 (a)]. Moreover, we observe that the bound state oscillation prior ionization $\chi_{\mathbf{k},\mu}(t_1)$ increases for later ionization times (increasing ionization time t_1), while the contribution from the continuum propagation $\delta(T, t_1, \omega_k, \mathbf{p})$ decreases. This is consistent with the fact that, for later ionization times, the more time the electron is bound, the larger the contribution coming from $\chi_{\mathbf{k},\mu}(t_1)$, and accordingly the electron spends less time propagating in the continuum, leading to a smaller $\delta(T, t_1, \omega_k, \mathbf{p})$. In Figs. 5(b) and 5(c), we show the contribution from
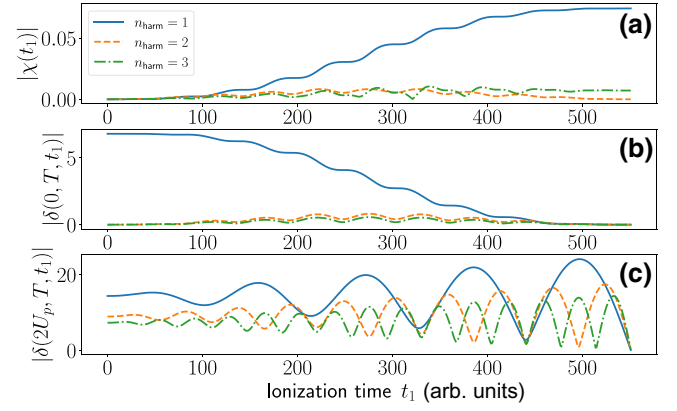

FIG. 5. Behavior of the shifts $|\chi(t_1)|$ [in (a)] and $|\delta(T, t_1, \omega_k, \mathbf{p})|$ [(b) $p = 0$ and (c) $p = 0.93\sqrt{U_p}$] over ionization time t_1. The different curves in each of the plots represent contributions to different harmonic modes (n_{harm}). In particular, the blue solid curve corresponds to the fundamental mode $n = 1$, the orange dashed curve to the second harmonic $n = 2$, and the green dash-dot curve to the third harmonic $n = 3$. In general, the displacement from $|\chi(t_1)|$ is, at least, 2 orders of magnitude smaller than that coming from $|\delta(T, t_1, \omega_k, \mathbf{p})|$, which furthermore gets enhanced for increasing values of the canonical momentum $\mathbf{p}$.

the continuum displacement $\delta(T, t_1, \omega_k, \mathbf{p})$ for two different canonical momenta $\mathbf{p} \in \{0, 0.93\sqrt{U_p}\}$. We observe that, for large canonical momentum, the shift is in general larger, and shows pronounced oscillations. The different oscillation periods in the displacement $\delta(T, t_1, \omega_k, \mathbf{p})$ for different harmonics, which is most pronounced in Fig. 5(c), originates from the nonlinear motion of the electron in the continuum. Since the displacement of each field mode is proportional to the respective Fourier component of the electron displacement in the continuum, the different modes are shifted depending on this nonlinear electron motion after ionization.

In Figs. 6(a) and 6(b) we respectively show the behaviors of the real and imaginary parts of the backaction on the field due to the continuum propagation of the electron $\delta_\alpha(T, t_1, \omega_k, \mathbf{p})$ for the fundamental mode for positive (blue solid curve) and negative (orange dashed curve) values of the initial canonical momentum. The real part shows similar behavior in both cases with a phase difference of π between the oscillations. The imaginary part shows the same phase difference of π, but is positive (negative) for positive (negative) initial momenta $\mathbf{p}$. The different signs of the initial electron momentum dictates the propagation direction of the electron in the continuum. Since the sign of the displacement amplitude $\delta_\alpha(T, t_1, \omega_k, \mathbf{p})$ determines the in- or out-of-phase shift of the fundamental mode in phase space, this leads to an increasing or decreasing in the coherent state amplitude, respectively. This interference then either leads to an enhancement or depletion of
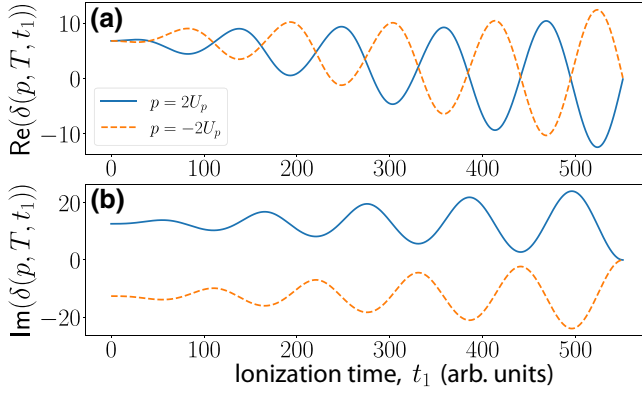
FIG. 6. Real (a) and imaginary (b) parts of the shift of the fundamental mode $\delta(T, t_1, \omega_k, \mathbf{p})$ for values of the canonical momenta $p = 0.93\sqrt{U_p}$ (blue solid curve) and $p = -0.93\sqrt{U_p}$ (orange dashed curve). The different behaviors obtained for positive and negative momenta are a consequence of the carrier-envelope phase (CEP) (which is the phase between the carrier wave and the pulse envelope) of the employed laser field, such that a change in π of this phase interchanges the behavior obtained for positive and negative momenta.

the fundamental driving laser amplitude (see the discussion below). Note that the influence of the positive and negative momenta depends on the carrier-envelope phase (CEP) of the driving laser field. A π phase change in the CEP leads to the same effect as interchanging the positive and negative electron momenta [125].

However, so far we have only considered a conditioning on a single final electron momentum. In order to obtain the EM field state when including all possible final momenta of the electron, we integrate Eq. (68) over $\mathbf{v}_\alpha$ and obtain the corresponding mixed state density matrix

$$\rho_{\mathrm{ATI}}(t) = \int d^3 v_\alpha \, |\phi_\alpha(\mathbf{v}_\alpha, t)\rangle \langle\phi_\alpha(\mathbf{v}_\alpha, t)| \,. \qquad (70)$$

The states in Eq. (68) (pure state for single final electron momentum) and Eq. (70) (mixed state for all possible final electron momenta) are the final states of the EM field in intense laser-atom interaction conditioned on the process of ATI. All relevant quantities of the optical field can be obtained from here on.

2. Field observables

To obtain further insights into the dynamical behavior of the optical field during the process of ATI, we compute the corresponding photon-number distribution of the fundamental mode that drives the ionization process. We consider the case where the ionization is conditioned on a particular electron momentum such that we can use the pure state (68), and evaluate the action of the first displacement operation

$$|\phi_{\mathrm{ATI}}(t, \mathbf{p})\rangle = \frac{-ie}{\hbar} \int_{t_0}^{t} dt' \mathcal{D}[\boldsymbol{\delta}(t, t_1, \mathbf{v}_\alpha)] \mathbf{E}_Q(t', \mathbf{R}_\alpha)$$

$$\cdot \langle \mathbf{v}_\alpha | \, \mathbf{r}_\alpha(t') \, |g\rangle \bigotimes_{\mathbf{k},\mu \simeq \mathbf{k}_{L,\mu}} |\chi_{\mathbf{k},\mu}(t')\rangle$$

$$\bigotimes_{\mathbf{k},\mu \gg \mathbf{k}_{L,\mu}} |\chi_{\mathbf{k},\mu}(t')\rangle \,. \qquad (71)$$

To compute the observables of the EM field, we first need to transform back into the original laboratory frame

$$|\Phi_{\mathrm{ATI}}(t, \mathbf{p})\rangle = e^{-iH_f t} D(\alpha_{\mathbf{k}_L}) |\phi_{\mathrm{ATI}}(t, \mathbf{p})\rangle \,. \qquad (72)$$

In the following, we are interested in the backaction on the driving field due to the process of ATI. In Fig. 5 we have seen that the oscillation of the electron in the continuum gives rise to non-negligible contributions to the shift in the harmonic modes. Thus, in order to eliminate possible contributions from HHG, we project state (72) onto the vacuum of harmonic modes $|\{0\}_{\mathrm{HH}}\rangle = \bigotimes_{\mathbf{k},\mu \gg \mathbf{k}_L \mu} |0_{\mathbf{k}\mu}\rangle$, which takes into account only the cases in which no harmonic photon is emitted. The state of the fundamental mode, after conditioning on a final electron momentum $\mathbf{p}$, and on zero harmonic photons $|\{0\}_{\mathrm{HH}}\rangle$, is then given by (see Appendix E for details)

$$|\Phi_{\mathrm{ATI}}^{\mathbf{k}_L}(t, \mathbf{p})\rangle = \langle\{0\}_{\mathrm{HH}}| \, |\Phi_{\mathrm{ATI}}(t, \mathbf{p})\rangle \,. \qquad (73)$$

We first compute the photon-number distribution of the driving field (see Appendix E)

$$P_{n_{\mathbf{k}_L}}(t, \mathbf{p}) = |\langle n_{\mathbf{k}_L} | \tilde{\Phi}_{\mathrm{ATI}}(t, \mathbf{p})\rangle|^2 \,. \qquad (74)$$

Having calculated the photon-number distribution $P_{n_{\mathbf{k}_l}}$ $(t, \mathbf{p})$, we further compute the photon-number expectation value in the fundamental mode

$$\langle n_{\mathbf{k}_L}(t, \mathbf{p})\rangle = \sum_{n_{\mathbf{k}_L}} n_{\mathbf{k}_L} P_{n_{\mathbf{k}_L}}(t, \mathbf{p}) \,. \qquad (75)$$

In Fig. 7, we show the mean photon number from Eq. (75) for values of the canonical momentum ranging from $-0.46\sqrt{U_p}$ to $0.46\sqrt{U_p}$, i.e., within a regime where we can neglect the rescattering effects [126]. On the other hand, in Fig. 8 we show the photon-number probability distribution for different values of the canonical momentum. In both cases, we use $\alpha = 7i$, in agreement with the form considered for the vector potential (see Appendix G for more details about the numerical implementation). The main feature that one can observe in these plots is the different behaviors that are obtained for the conditioning over positive and negative momenta. As we see in Fig. 7, for negative values of the canonical momentum, we find that the actual mean photon number of the input field gets
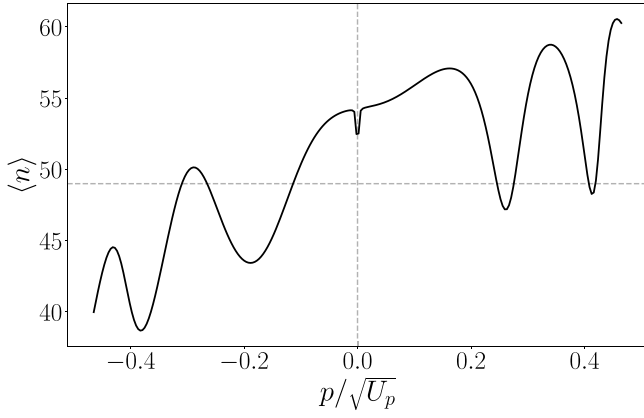
FIG. 7. The mean value of the photon number (75) of the fundamental mode at the end of the pulse. Here, we use $\alpha = 7i$ to reproduce the form of the considered field. In order to avoid reaching the numerical limit of the machines used for the computation, we have multiplied the field constant by 0.2 (see Appendix G for details). We consider a field with a sinusoidal squared envelope with $\omega = 0.057$ a.u., five cycles of duration, and field amplitude $E_0 = 0.053$ a.u.

reduced, in contrast to positive momenta that can increase the mean value of the photon number in the fundamental mode.

Since the shift of the amplitude in the fundamental mode is mostly determined by the displacement due to the electron propagation in the continuum via $\delta(T, t_1, \omega_k, \mathbf{p})$ (see Fig. 5), the different behaviors for positive and
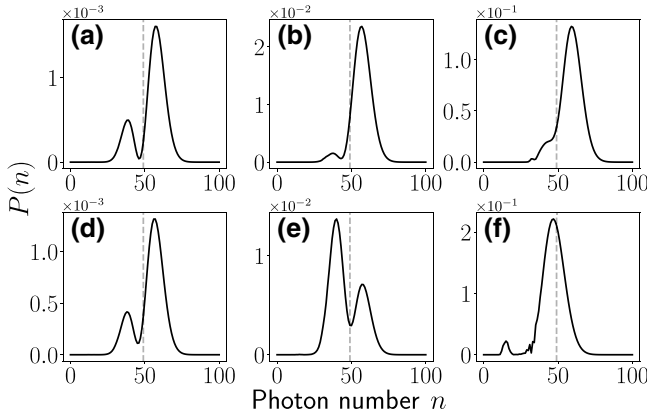

FIG. 8. Photon-number probability distribution (74) for positive (upper row) and negative (lower row) values of the canonical momentum. Specifically, we use (a) $p = 0.05\sqrt{U_p}$, (b) $p = 0.14\sqrt{U_p}$, (c) $p = 0.32\sqrt{U_p}$, (d) $p = -0.05\sqrt{U_p}$, (e) $p = -0.14\sqrt{U_p}$, and (f) $p = -0.32\sqrt{U_p}$. We consider a field with a sinusoidal squared envelope with $\omega = 0.057$ a.u., five cycles of duration, and field amplitude $E_0 = 0.053$ a.u. The vertical gray dashed line shows the location of the maximum photon-number probability for the initial coherent state used in the numerical analysis, i.e., $\alpha = 7i$.

negative momenta crucially depend on the phase of $\delta(T, t_1, \omega_k, \mathbf{p})$ (see Fig. 6). Thus, the depletion (enhancement) of the average photon number in the driving laser mode is due to the phase of the displacement for the continuum propagation for negative (positive) initial electron momenta. The opposite sign comes from the opposite propagation direction of the electron for opposite initial momenta, such that the Fourier transform of this displacement leads to the π phase difference in the shift of the field. This observed behavior of the displacement for opposite momenta can be summarized as follows: for negative values of p, the scattered radiation by the electron interferes out of phase with the input field, leading to a decrease in the overall mean photon number; for positive values of p, the interference takes place in phase, and an overall enhancement in the mean photon number of the input field is obtained. For increasing momentum, the enhancement or depletion generally increases. This is an expected feature as the larger the canonical momentum, the larger the electron's excursion and therefore the value of the displacement $|\delta(T, t_1, \omega_k, \mathbf{p})|$.

Finally, we show the photon-number probability distribution in Fig. 8, which reveals that the fundamental mode is in a coherent state superposition when the interaction is conditioned on the ATI processes [see Eq. (71)]. This is reflected in the multipeak structure of the photon-number probability distribution that can be seen in Fig. 8 (cf. Sec. II B). However, especially for large momenta as in Figs. 8(c) and 8(f) with canonical momenta $p = 0.32\sqrt{U_p}$ and $p = -0.32\sqrt{U_p}$, respectively, we get a dominant peak. Even though in this case, and according to Fig. 5, more peaks are expected as the value of $\delta(T, t_1, \omega_k, \mathbf{p})$ has more pronounced oscillations, the conditioning measurement over the harmonic modes we considered selects some specific values of $\delta(T, t_1, \omega_k, \mathbf{p})$, leading to a Poissonian-like behavior for the final probability.

D. Rescattering in ATI

We are now interested in incorporating the rescattering events in the ATI description given in the previous subsection. For that purpose, we start from Eq. (56), and consider only a single atom within the single active electron approximation (we therefore drop the index α)

$$i\hbar \frac{d}{dt} |\psi(\mathbf{v}, t)\rangle = e\mathbf{E}_Q(t, \mathbf{R}) \cdot \langle \mathbf{v}| \mathbf{r}(t) |\Psi(t)\rangle, \quad (76)$$

which, after introducing the SFA version of the identity (38), leads to

$$i\hbar \frac{d}{dt} |\phi(\mathbf{v}, t)\rangle = e\mathbf{E}_Q(t, \mathbf{R}) \cdot \langle \mathbf{v}| \mathbf{r}(t) |g\rangle |\phi(t)\rangle$$
$$+ e\mathbf{E}_Q(t, \mathbf{R}) \cdot \int d^3v' \langle \mathbf{v}| \mathbf{r}(t) |\mathbf{v}'\rangle |\phi(\mathbf{v}', t)\rangle. \quad (77)$$

In the direct ionization analysis we neglected the effect of the rescattering transition terms, i.e., the $\mathbf{g}(\mathbf{v}, \mathbf{v}')$ term in Eq. (60). The reason for this is that we treat them as a first-order perturbation term [12]. However, in order to describe the rescattering process, these terms need to be taken into account, such that our differential equation now reads

$$i\hbar \frac{d}{dt} |\phi(\mathbf{v}, t)\rangle = e\mathbf{E}_Q(t, \mathbf{R}) \cdot \langle \mathbf{v}| \mathbf{r}(t) |g\rangle |\phi(t)\rangle + e\mathbf{E}_Q(t, \mathbf{R}) \cdot \Delta\mathbf{r}(t, \mathbf{v}) |\phi(\mathbf{v}, t)\rangle$$

$$- \frac{\hbar}{e} \int d^3 v' \exp\left[\frac{i}{\hbar} S(\mathbf{v}, t, t_0)\right] \mathbf{E}_Q(t, \mathbf{R}) \cdot \mathbf{g}(\mathbf{v}, \mathbf{v}') \exp\left[-\frac{i}{\hbar} S(\mathbf{v}', t, t_0)\right] |\phi_\alpha(\mathbf{v}', t)\rangle. \qquad (78)$$

We now perform a perturbative expansion of the quantum optical state when conditioned to ATI up to first order in perturbation theory, such that we now include the effect of the rescattering terms

$$|\phi(\mathbf{v}, t)\rangle \approx |\phi^{(0)}(\mathbf{v}, t)\rangle + |\phi^{(1)}(\mathbf{v}, t)\rangle. \qquad (79)$$

Introducing these terms into the Schrödinger equation (78) we get for the first-order perturbation theory term (see Appendix F for details)

$$|\phi^{(1)}(\mathbf{p}, t)\rangle = -\frac{e}{\hbar} \int_{t_0}^t dt_2 \int d^3 p' \int_{t_0}^{t_2} dt_1 \mathcal{D}[\boldsymbol{\delta}(t, t_2, \mathbf{p}_\alpha)] \exp\left[\frac{i}{\hbar} S(\mathbf{p}, t_2, t_0)\right]$$

$$\times \mathbf{E}_Q(t_2, \mathbf{R}) \cdot \mathbf{g}\left(\mathbf{p} + \frac{e}{c}\mathbf{A}(t), \mathbf{p}' + \frac{e}{c}\mathbf{A}(t)\right) \mathcal{D}[\boldsymbol{\delta}(t_2, t_1, \mathbf{p}'_\alpha)] \exp\left[\frac{i}{\hbar} S(\mathbf{p}', t_2, t_1)\right]$$

$$\times \mathbf{E}_Q(t_1, \mathbf{R}) \cdot \left\langle \mathbf{p}' - \frac{e}{c}\mathbf{A}(t) |\mathbf{r}(t_1)|g \right\rangle \mathcal{D}[\boldsymbol{\chi}(t_1)] |\phi(t_0)\rangle, \qquad (80)$$

where we have expressed the final state in terms of the canonical momenta $\mathbf{p}$ and $\mathbf{p}'$.

The expression above gives the complete quantum electrodynamics of the rescattering process: first the electron gets ionized at t_1, which has associated a displacement in the photonic quadratures; afterwards, the electron propagates in the continuum until t_2, acquiring the usual semiclassical phase while the electromagnetic field gets displaced by $\delta(t_2, t_1, \omega_k, \mathbf{p}')$, a quantity that depends on the electron displacement from t_1 to t_2; finally, at time t_2, the electron rescatters with the core potential such that its velocity changes from $\mathbf{p}'$ to $\mathbf{p}$, and it propagates in the continuum until it is measured. Again, during this last process, the field gets displaced by $\delta(t, t_2, \omega_k, \mathbf{p})$, i.e., a quantity that depends on the electron displacement since the rescattering takes place at time t_2 until it is finally measured at time t. From here, and analogously to the direct ionization case, we can introduce the single-mode approximations and then proceed to compute the quantum optical observables, which leads to expressions where the rescattering terms add incoherently to those we already obtained in direct ATI. While, for values of $p < 2\sqrt{U_p}$, we do not expect these terms to play a very important role, similarly to what happens in the semiclassical analysis [126], the same cannot be said for the regime $2\sqrt{U_p} < p < 5\sqrt{U_p}$, and will be part of future investigations.

V. EXPERIMENTAL APPROACH FOR QUANTUM STATE ENGINEERING

In this section we provide an approach where the aforementioned theoretical findings can be experimentally investigated. Specifically, we describe the operation principles of an experimental scheme that allows: (a) generation of the nonclassical light states by implementing conditioning approaches on the field modes after the interaction, (b) the control of the quantum features of the generated nonclassical light states, and (c) the characterization of the quantum states of light.

A. General description

A schematic diagram of the experimental configuration is shown in Fig. 9, with the scheme divided into four units. Unit 1 concerns the laser beam delivery (LBD). It is used to control the properties of the driving laser field towards the laser-atom interaction region. It contains the laser beam steering, polarization control, beam shaping, pulse characterization, and focusing optics. Unit 2 is the target area (TA) where the intense femtosecond (fs) infrared (IR) laser pulse interacts with the gas target, leading to the generation of ions (that we omit from our present discussion), ATI photoelectrons, and high-harmonic photons emitted towards the extreme ultraviolet (XUV) spectral region. The atomic gas medium is placed at the focus of the IR
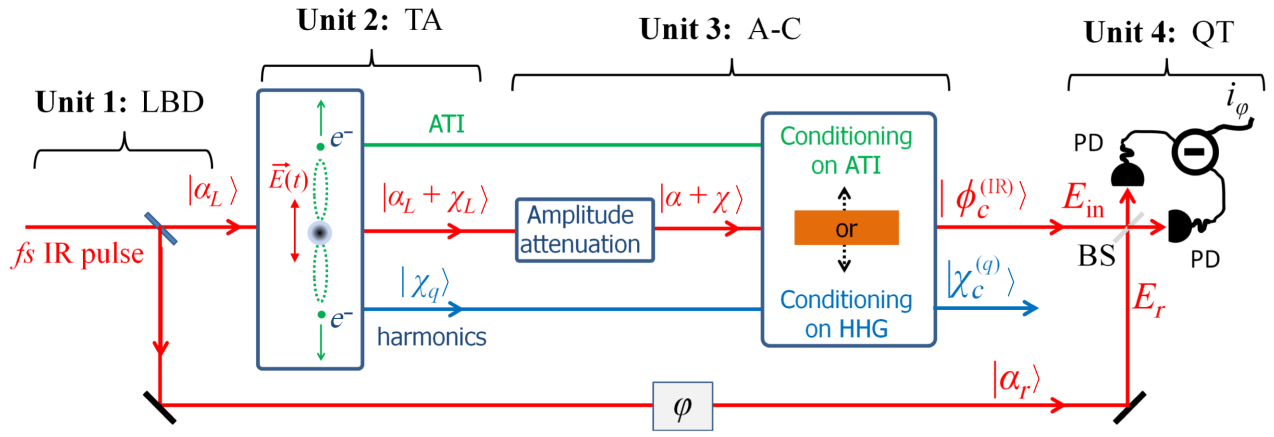
FIG. 9. Schematic illustration of the operation principle of the experimental approach. Unit 1: laser beam delivery (LBD) system. Unit 2: target area (TA). The intense laser-atom interaction is shown in the context of the electron recollision picture. The ATI photoelectrons are emitted in the direction of the polarization of the driving IR field, while the generated high harmonic copropagates with the IR field. Unit 3: IR attenuation and conditioning (A-C) on HHG and/or ATI processes. Here $|\alpha_L\rangle$ is the initial coherent state of the driving field and $|\alpha_L + \chi_L\rangle$, $|\alpha + \chi\rangle$ are the states of the IR field after the interaction and attenuation, respectively; the $|\chi_q\rangle$ correspond to the coherent states of the harmonic modes; $|\phi_c^{(\text{IR})}\rangle$ and $|\chi_c^q\rangle$ are the field states conditioned on HHG or ATI processes for the IR and high-harmonic field states, respectively, which correspond to a coherent state superposition. We note that the detailed expressions of the light states are given in Sec. IV. Unit 4: a typical scheme of the QT method for the characterization of state $|\phi_c\rangle$, with state $|\alpha_r\rangle$ of the local oscillator reference field, with a controllable phase shift ϕ. BS is a beam splitter, the PD are identical IR photodiodes used from the balanced detector, and i_ϕ is the ϕ-dependent output photocurrent difference used for the measurement of the electric field operator and the light state characterization via the reconstruction of the Wigner function.

beam, and the photon or electron detectors are used to measure the interaction products. Unit 3 contains an optical arrangement for IR photon-number attenuation, and a photon (electron) correlation approach is used to condition the field modes exiting the medium on the HHG (ATI) processes. Unit 4 deals with the quantum state characterization of the field, which can be achieved using the quantum tomography (QT) approach [127,128]. It is noted that the degree of IR attenuation in unit 3 is associated with the limitations of the QT approach to characterize the optical field states [129], which is typically in the range of a few photons, and does not originate from the conditioning approach itself, which in principle is applicable for high-photon-number light states.

B. Experimental procedure

In a typical intense laser-atom interaction experiment [130, and references therein], a linearly polarized IR femtosecond laser pulse of $\langle N_0 \rangle \sim 10^{14}$ photons per pulse is delivered by unit 1. The pulse is focused with an intensity $I_{\text{IR}} \sim 10^{14}$ W/cm^2 into an atomic ensemble of atomic density typically of 10^{18} atoms/cm^3 placed in unit 2 (see Fig. 10). The photon number and the spectrum of the generated harmonics can be measured by means of calibrated XUV photodetectors and/or XUV spectrometers, respectively. The charged ions (not shown in Fig. 10) and the ATI photoelectrons can be measured by means of time-of-flight (TOF) spectrometers. The two TOF spectrometers

(shown in the upper and lower parts of Fig. 10) can be used for measuring the ATI spectra, and discriminating between the electrons with positive and negative momenta. This arrangement is central when using few-cycle laser pulses, and has been extensively used as a diagnostic of the CEP pulse-to-pulse stability of laser systems delivering few-cycle laser pulses [131]. As an example, in Fig. 11 we show the calculated HHG and ATI spectra produced by the interaction of xenon atoms with a multi- and few-cycle femtosecond IR ($\lambda_L \approx 800$ nm) laser pulse. Quantities S_{XUV} and $S_{\text{ATI}}^{(\text{pos,neg})}$ correspond to the current from the integrated, over a defined region of the spectra (shown as a gray shaded region in Fig. 11), harmonic intensity and ATI photoelectron signals, respectively. We note that, when using multicycle driving laser fields, the use of two TOF spectrometers is not needed as the positive and negative electron ATI spectra are almost identical, i.e., $S_{\text{ATI}}^{(\text{pos})} \approx S_{\text{ATI}}^{(\text{neg})}$.

After the harmonic separator, the IR beam enters in unit 3 (Fig. 12). Here, the beam passes through an amplitude attenuation optical arrangement consisting of neutral density filters (F), a beam splitter (BS), and a spatial filter (aperture) placed in the IR beam path. In this way, the mean photon number of the IR beam after the aperture (A) (i.e., before entering unit 4) can be reduced to the level of a few photons per pulse. Separating some portion of the IR beam via the BS is necessary for implementing the conditioning procedure, which will be explained in more
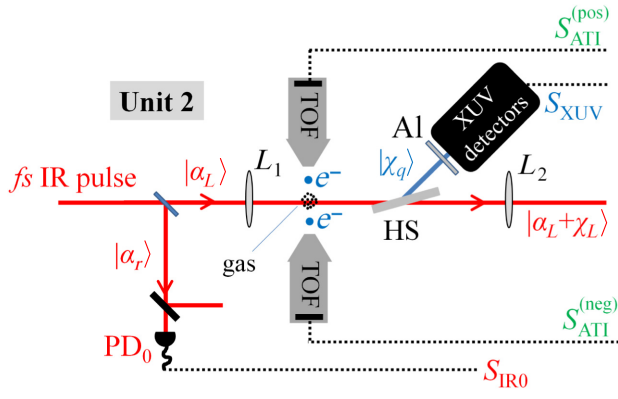
FIG. 10. A more detailed scheme of unit 2. Here L_1 is an IR focusing lens. The arrangement with the TOF spectrometers can be used for measuring the ATI spectra associated with positive and negative electron momenta. HS is a harmonic separator that transmits the IR field and reflects the high harmonics towards the XUV detectors. Al is a thin aluminum metal filter that transmits the harmonics with $q \geq 11$ (harmonics in the plateau and cutoff region of the spectrum). In this way we eliminate the contribution of low-order harmonics that are mainly produced by multiphoton processes. Additionally, the presence of a metal filter is an experimental requirement for blocking any residual part of the IR beam reflected by the HS. The lens L_2 is used to collimate the IR beam after the interaction. With $S_{\mathrm{ATI}}^{(\mathrm{pos,neg})}$ and S_{XUV} we denote the integrated, over a defined region of the spectra, ATI and HHG signals, respectively. When using multicycle driving laser fields, the use of only one TOF is sufficient as $S_{\mathrm{ATI}}^{(\mathrm{pos})} \approx S_{\mathrm{ATI}}^{(\mathrm{neg})}$.

detail below. The photodiode $\mathrm{PD_{IR}}$ is used to record the IR photon-number signal S_{IR} that is reflected by the BS. The S_{XUV}, $S_{\mathrm{ATI}}^{(\mathrm{pos,neg})}$, S_{IR}, as well as the photon-number signal of the driving laser field S_{IR0} entering in unit 2, need to be simultaneously recorded for each laser shot in order to condition the outgoing field modes on the HHG and ATI processes. The S_{IR0} is used to trace the energy of the driving laser field and selects (in case that is needed) only the shots with the highest possible energy stability, typically at a level of $\lesssim 1\%$. It is noted that the electronic noise needs to be subtracted from all signals.

1. Conditioning in the experiment

The quantum operations described in Sec. IV can be implemented by means of the quantum spectrometer (QS) approach [80,132]. The QS is a shot-to-shot photon correlation–based method that provides the probability of absorbing photons from a driving laser field towards the generation of intense laser-atom interaction products, such as HHG photons and ATI electrons. Its operation principle relies on photon statistics and the shot-to-shot correlation between the interaction products and the energy conservation, i.e., when the signal of the interaction products increases, the IR signal S_{IR} decreases. The method has been described in Refs. [80,90,94,132], and was used for
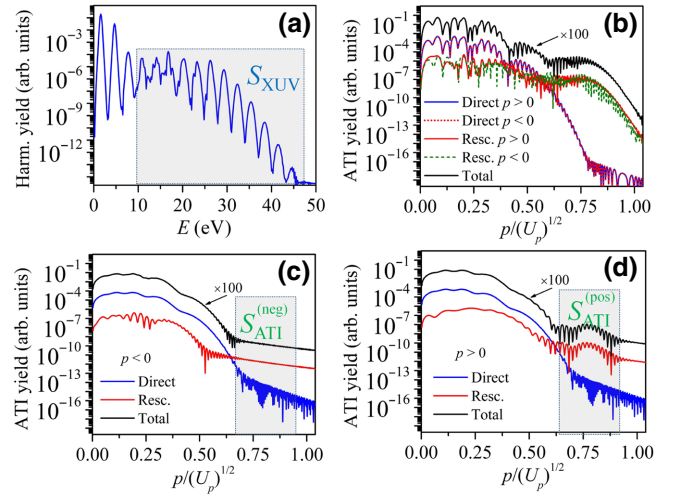

FIG. 11. Calculated HHG and ATI spectra using the QPROP software [119]. Panels (a) and (b) respectively show the HHG and ATI spectra produced by the interaction of xenon atoms with a linearly polarized laserpulse, with a sinusoidal squared envelope, of intensity 8×10^{13} W/cm^2 and about 30-fs duration. In (b) the photoelectron spectra corresponding to direct and rescattered photoelectrons with positive ($p > 0$) and negative ($p < 0$) momenta are shown with different colors. Panels (c) and (d) respectively show the ATI spectra for negative and positive electron momenta produced by the interaction of xenon atoms with a linearly polarized laser pulse of intensity 8×10^{13} W/cm^2 and about 5-fs duration. The CEP effect is depicted in the high-energy part of the ATI spectra of the negative and positive photoelectrons. The ATI spectra corresponding to the direct and rescattered electrons are shown with different colors. In all graphs the total ATI spectrum (black solid curve), which includes the contribution of the direct and rescattered electrons, has been shifted by a factor of 100 for visualization reasons. The gray shaded areas depict an example of the controllable (in the width and their position in the spectra) integrated areas of the $S_{\mathrm{ATI}}^{(\mathrm{pos,neg})}$ and S_{XUV}.

the generation of optical Schrödinger "catlike" and "kittenlike" states [90,92] by conditioning the IR field state on the HHG process.

Here, as an example, we briefly discuss the QS method using the HHG process. After the light-matter interaction takes place in unit 2, the IR and XUV photon numbers are respectively N_{IR} and N_{XUV}. The N_{IR} is smaller than the photon number of the IR field before the interaction (N_0) due to IR photon losses associated with all processes taking place in the interaction region. The IR and XUV photon numbers reaching the $\mathrm{PD_{IR}}$ detector in unit 3 and the XUV detector in unit 2 are n_{IR} and n_{XUV}, respectively. These are related with N_{XUV} and N_{IR} through the equations $n_{\mathrm{XUV}} = N_{\mathrm{XUV}}/A_{\mathrm{XUV}}$ and $n_{\mathrm{IR}} = N_{\mathrm{IR}}/B_{\mathrm{IR}}$, where A_{XUV} and B_{IR} are the attenuation factors corresponding to the XUV and IR photon losses introduced by the optical elements in the beam paths. The n_{IR}, n_{XUV}, and n_0 (where n_0 is the photon number of the attenuated IR field reaching the detector $\mathrm{PD_0}$ in unit 2) signals are recorded for each laser
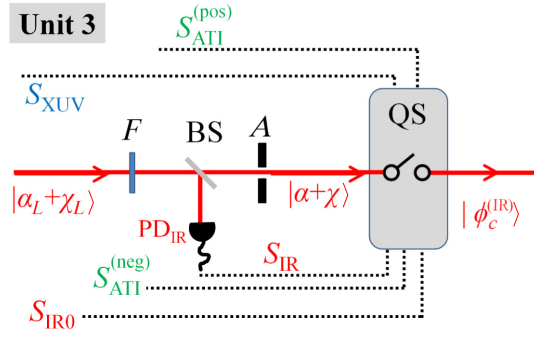
FIG. 12. A schematic illustration of unit 3. Here F, BS, and A respectively represent a neutral density filter, a beam splitter, and an aperture; PD_{IR} is an IR photodetector; S_{XUV}, $S_{ATI}^{(pos,neg)}$, S_{IR}, and S_{IR0} are the signals used by the quantum spectrometer (QS) to condition the $|\alpha + \chi\rangle$ state on the HHG or ATI processes.

FIG. 13. (a) (S_{XUV}, S_{IR}) photon-number distribution (gray points). The mean values of S_{XUV} and S_{IR} are normalized to 1. Here W_j shows the width of the distribution. The red points show the selected points along the anticorrelation diagonal of width w_{ant}. The distribution is created by keeping the energy stability of the driving field at the level of approximately 1%, and after subtracting the electronic noise from each laser shot. (b) Probability of absorbing IR photons (P_{IR}) towards HHG. The arrows depict the positions of the peaks in the multipeak structure of P_{IR}. Figure reproduced from Ref. [92].

shot by a high dynamic range boxcar integrator, resulting in photocurrent outputs S_{IR}, S_{XUV}, and S_{IR0}. The S_{IR0} is used in order to collect the laser shots that provide energy stability typically at a level of $\lesssim 1\%$. Then, and after balancing the mean value of the S_{XUV} on the mean value of the S_{IR}, we create the joint distribution (S_{XUV}, S_{IR}) shown in Fig. 13(a). The distribution is a kind of multidimensional map that contains information of all processes occurring during the laser-atom interaction, and provides access to the correlated XUV-IR signals. Also, taking into account the fact that the generation of N_q photons of the qth harmonic corresponds to qAN_q IR photons lost (where A is the XUV absorption factor in the HHG medium), information about the probabilities of absorbing IR photons towards harmonic generation can be extracted. However, the number of points at which the IR photons are correlated with the generated harmonic photons is a small fraction (typically about 0.1%) compared to the total number of points in the distribution. To reveal these points, we take advantage of the energy conservation, and we collect only those lying along the anticorrelation diagonal of the joint distribution. These points provide the probability of absorbing IR photons (P_{IR}) towards the harmonic emission. The P_{IR} depicts a multipeak structure corresponding to the generated high-harmonic orders [Fig. 13(b)], with a spacing between the peaks of $(\Delta q)AN_q = 2AN_q$, with $\Delta q = 2$ the distance between two harmonic peaks in the HHG spectrum. The minimum value of the width (w_{ant}) of the anticorrelation diagonal, which defines the resolution of the QS, can be experimentally obtained by the accuracy to find the peak of the joint distribution, which is $w_{ant} = W_j/\sqrt{k}$, where W_j is the percentage of the width of the joint distribution relative to its mean value and k is the number of points in the distribution. Here, it is important to note that the power of the QS to resolve the multipeak structure of P_{IR} and to condition the IR state on the HHG process is associated
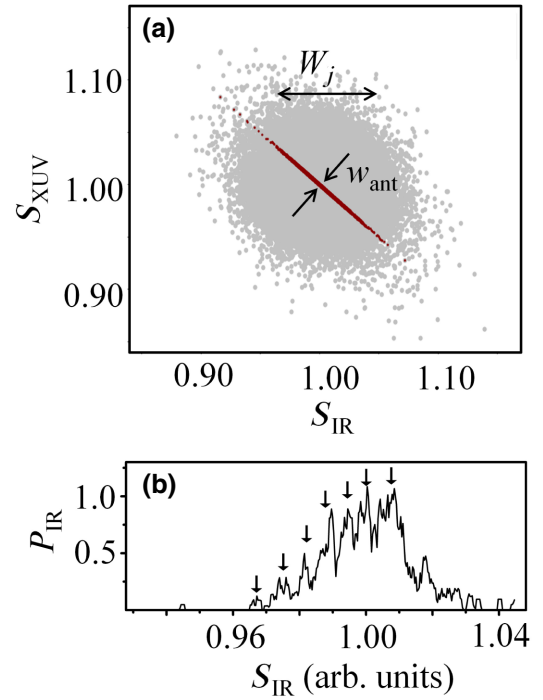
with the dynamic range of the detection system, the number of IR photons absorbed towards the harmonic emission (associated with the conversion efficiency of the HHG process), the number of accumulated shots, and the number of XUV-IR correlated points. Because of this multiparameter dependence of the resolution, there is large space for further improvement in the QS method.

Additionally, by selecting the points along the anticorrelation diagonal, we condition the IR field state exiting the medium on the HHG process. This is because we select only those shots that are relevant to the harmonic emission, and we remove the unwanted background associated with all residual processes, e.g., electronic excitation or ionization. This action corresponds to the application of the $\Pi_{\tilde{n}\neq 0} = \mathbb{1} - \Pi_{\tilde{0}}$ operator onto the field state given by Eq. (46), and its projection onto the harmonic field modes [see Eq. (53) in Sec. IV B] [91,93]. This results in the creation of an IR field coherent state superposition that is given by Eq. (53).

Hereafter, for the sake of simplicity, we express the conditioned light states by considering only a single mode for the input IR field (we further omit the oscillation term

$e^{-i\omega t}$). In this case Eq. (53) reads

$$|\phi_c^{(\text{IR})}\rangle_{\text{HHG}} = |\alpha + \chi\rangle - \xi_{\text{IR}} |\alpha\rangle, \qquad (81)$$

which is a genuine optical Schrödinger "catlike" state in the IR spectral range. The approach can likewise be used for creating an optical Schrödinger "catlike" state in the XUV spectral range [91]. This can be achieved if the S_{XUV} contains the integrated signal of all high-harmonic orders except one, let us say the qth. In this case Eq. (54) reads

$$|\chi_c^{(q)}\rangle_{\text{HHG}} = |\chi_q\rangle - \xi_q |0_q\rangle, \qquad (82)$$

which is a coherent state superposition in the spectral range of the qth harmonic. In a similar way, the method can be applied to the ATI process using the photoelectron signal $S_{\text{ATI}}^{(\text{pos,neg})}$. After selecting only the shots that are relevant to the ATI photoelectron emission from the joint distribution $(S_{\text{ATI}}^{(\text{pos,neg})}, S_{\text{IR}})$, we condition the IR field state on the ATI process. In the case that the signal $S_{\text{ATI}}^{(\text{pos,neg})}$ is integrated over all possible outgoing momenta, the resulting IR state is a mixed state of coherent state superpositions given by Eq. (70), and is therefore written as

$$\rho_c^{(\text{ATI})} = \int d\mathbf{p} C(\mathbf{p}) |\Phi_{\text{ATI}}^{\mathbf{k}_L}(t, \mathbf{p})\rangle \langle \Phi_{\text{ATI}}^{\mathbf{k}_L}(t, \mathbf{p})|. \qquad (83)$$

When using a multicycle fundamental driving field, where the ATI spectrum consists of well-defined photoelectron peaks [Fig. 11(b)], we can approximate the state by

$$\rho_c^{(\text{ATI})} = \sum_{\mathbf{p}_i} C(\mathbf{p}_i) |\Phi_{\text{ATI}}^{\mathbf{k}_L}(t, \mathbf{p}_i)\rangle \langle \Phi_{\text{ATI}}^{\mathbf{k}_L}(t, \mathbf{p}_i)|. \qquad (84)$$

We note that in Eqs. (81)–(84), the factors ξ_{IR}, ξ_q, and $C(\mathbf{p})$, are complex, and reflect the coupling of the initial coherent state with the shifted one. Their absolute values are in the range $0 < |\xi_{\text{IR}}|, |\xi_q|, |C(\mathbf{p})| < 1$ and they depend on χ, χ_q, and $\mathbf{p}$, respectively.

Additionally, the approach can be used for creating entangled coherent state superpositions between different driving frequency modes [91,93]. This can be achieved, for instance, by generating high harmonics using a multimode driving field. Such experiments are typically performed using a two-frequency ($\omega_1 - \omega_2$) field (in the visible-infrared spectral range), usually consisting of the fundamental harmonic and its second harmonic [133–135]. In this case, the state of the field before the interaction is $|\alpha_{\omega_1}\rangle |\alpha_{\omega_2}\rangle$, which after the interaction and attenuation becomes $|\alpha_{\omega_1} + \chi_{\omega_1}\rangle |\alpha_{\omega_2} + \chi_{\omega_2}\rangle$. Following the correlation measurement-based procedure used to obtain

Eq. (81), the state conditioned on HHG is given by

$$\begin{aligned}|\phi_c^{(\omega_1, \omega_2)}\rangle_{\text{HHG}} = \,&|\alpha_{\omega_1} + \chi_{\omega_1}\rangle |\alpha_{\omega_2} + \chi_{\omega_2}\rangle \\ &- \xi_{(\omega_1, \omega_2)} |\alpha_{\omega_1}\rangle |\alpha_{\omega_2}\rangle, \qquad (85)\end{aligned}$$

which is an entangled coherent state in the visible-infrared spectral range. The degree of entanglement for different shifts $\chi_{\omega_{1,2}}$ of the two driving field modes has been discussed in Ref. [91] in terms of an entanglement witness based on the purity of the reduced density matrix.

2. Control of the optical quantum state

The control of quantum features of light states shown in Eqs. (81)–(84) relies on the control of χ, χ_q, and $\mathbf{p}$. This can be achieved by changing the density of atoms in the interaction region, the intensity of the employed laser field, the field polarization, the CEP when using a few-cycle laser system, or the measured interaction products used by the QS. Evidently, there is a large number of combinations that can be used as "knobs" for controlling the quantum features of the coherent state superposition. A representative example that shows the power of the approach on controlling the features of the coherent state superposition can be given using Eq. (81). It can be shown that, when the shift of the coherent state χ is reduced, the overlap between the initial coherent state and the shifted one gets higher, i.e., the value of $|\xi_{\text{IR}}|$ increases, and in the extreme case where $|\xi_{\text{IR}}| \to 1$ the coherent state superposition takes the form $|\phi_c^{(\text{IR})}\rangle_{\text{HHG}} \approx D(\alpha) |1\rangle$, which is an optical "kitten-like" state [90,92]. This has been confirmed experimentally [92] by reducing the gas density in the TA of unit 2. On the other hand, when the shift of the coherent state χ is increased (which can be done by increasing the gas density), the overlap between the initial coherent state and the shifted one decreases, i.e., the value of $|\xi_{\text{IR}}|$ is reduced, and in the extreme case where $|\xi_{\text{IR}}| \to 0$ the coherent state superposition takes the form $|\phi_c^{(\text{IR})}\rangle_{\text{HHG}} \approx |\alpha + \chi\rangle$, which is a regular coherent state.

Finally, it is noted that the combination of the aforementioned control "knobs," together with optical arrangements consisting of passive linear optical elements (such as phase shifters, beam splitters, fibers, etc.), can provide an enormous number of combinations [136, and references therein] for the generation of large optical "catlike" states, and massively entangled states with controllable quantum features. We note that beam splitters and phase shifters are considered to be one of the most important optical elements in quantum state engineering and, hence, a brief description of their action on a field state is required.

3. Linear optical elements and "catlike" states from HHG

Phase shifter. A phase shifter introduces a phase shift φ in the field state. This can be achieved by exploiting the

refractive index of the materials introduced in the beam path, or via optical arrangements such as a delay stage. The unitary operator that describes the action of a phase shifter on a field state is $U(\varphi) = \exp[i\varphi b^\dagger b]$. When the light field before the phase shifter is in a coherent state $|\beta\rangle$, the state of the outgoing field is

$$U(\varphi)|\beta\rangle = |\beta e^{i\varphi}\rangle. \tag{86}$$

Obviously, if the incoming field is in an optical CSS state, e.g., $|\gamma\rangle + \xi|\beta\rangle$, the state of the output field will be $|\gamma e^{i\varphi}\rangle + \xi|\beta e^{i\varphi}\rangle$.

Beam splitter. The beam splitter is an optical element that mixes two incoming spatial field modes into two outgoing spatial modes, and is characterized by its transmission T and reflection $R = 1 - T$ coefficients. These coefficients depend on the frequency, and usually on the polarization of the light field. With b ($b^\dagger$) and c ($c^\dagger$) the annihilation (creation) operators of the two incoming spatial modes onto the BS, the unitary operator that describes the action of the beam splitter on the field state is $B(\theta) = \exp[\theta(bc^\dagger - b^\dagger c)]$ with $\theta = \arctan(\sqrt{T})$.

Coherent states on a beam splitter. Assuming that the incoming field modes are the coherent states $|\beta\rangle$ and $|\gamma\rangle$, the outgoing state from the beam splitter is

$$\begin{aligned} B(\theta)|\beta\rangle|\gamma\rangle &= |\beta\cos(\theta) + \gamma\sin(\theta)\rangle_t \\ &\otimes |-\gamma\cos(\theta) + \beta\sin(\theta)\rangle_r, \end{aligned} \tag{87}$$

where each of the components in the product state corresponds to one of the outgoing modes of the beam splitter. Subscripts t and r denote the transmitted and reflected parts, respectively. Here, it is important to note that in quantum optics, when only one field mode (let us say $|\beta\rangle$) enters the beam splitter, the input of the other mode is described by the vacuum state $|0\rangle$. In this case, it is evident from Eq. (87) that the output field state is $|\beta\cos(\theta)\rangle_t|-\beta\sin(\theta)\rangle_r$.

Optical "cat" states on a beam splitter. Assuming that the incoming field modes are an optical CSS state $|\gamma\rangle + \xi|\beta\rangle$ and the vacuum state $|0\rangle$, the outgoing state from the beam splitter reads

$$\begin{aligned} B(\theta)(|\gamma\rangle + \xi|\beta\rangle)|0\rangle &= |\gamma\cos(\theta)\rangle_t|-\gamma\sin(\theta)\rangle_r \\ &+ \xi|\beta\cos(\theta)\rangle_t|-\beta\sin(\theta)\rangle_r, \end{aligned} \tag{88}$$

which, for a nonzero transmissivity of the beam splitter, takes the form of an entangled coherent state between the two spatial modes, and is of the form

$$|\psi\rangle = \frac{1}{\sqrt{N}}(|\gamma_r\rangle_r|\gamma_t\rangle_t + \xi|\beta_r\rangle_r|\beta_t\rangle_t), \tag{89}$$

where N is the normalization factor and $|\gamma_r\rangle_r = \gamma\cos(\theta)$,
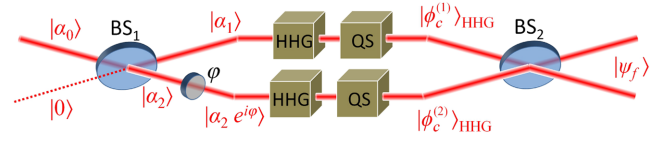

FIG. 14. An optical arrangement that leads to the entangled coherent state $|\psi_f\rangle$. Here $|\alpha_0\rangle$ is the initial coherent state of the driving IR field; $|\alpha_{1,2}\rangle$ are the coherent states after the beam splitter BS$_1$; $|\alpha_2 e^{i\varphi}\rangle$ is the state of the field after the phase shifter that introduces a phase φ in $|\alpha_2\rangle$; HHG and QS are the HHG areas and the QS arrangements; $|\psi_f\rangle$ is the final state after the last beam splitter (BS$_2$); $|\phi_c^{(1/2)}\rangle_{\text{HHG}}$ are the optical "catlike" states created after conditioning on HHG. State $|\psi_f\rangle$ can be controlled by the variables χ_1, χ_2, and φ.

$|\gamma_t\rangle_t = -\gamma\sin(\theta)$ (similar definitions follows for β). The entanglement properties of this state are particularly interesting if the distance between the coherent states appearing in each of the terms in the superposition is large enough, and the states $|\gamma_{r,t}\rangle_{r,t}$ and $|\beta_{r,t}\rangle_{r,t}$ are almost orthonormal. However, within the HHG approach, the generation of the coherent state superpositions is conditioned to relatively small values of the displacement χ, so in this scenario it is of interest to look for approaches that allow us to enlarge the distance between the two coherent states [95,137,138]. We can go even further with the entanglement by using a multibeam splitter arrangement and schemes consisting of multiple HHG and QS arrangements [95]. For example, let us assume that we use the arrangement shown in Fig. 14, where a single-mode IR coherent state $|\alpha_0\rangle$ enters the system that contains two beam splitters (BS$_1$ and BS$_2$), a phase shifter (φ), two HHG areas (unit 2 in Fig. 9), and two QS (unit 3 in Fig. 9). In this scheme the incoming field modes on the last beam splitter (BS$_2$) are both optical "catlike" states $|\phi_c^{(1)}\rangle = |\gamma_1\rangle + \xi_1|\beta_1\rangle$ and $|\phi_c^{(2)}\rangle = |\gamma_2\rangle + \xi_2|\beta_2\rangle$, and thus the outgoing state from the beam splitter reads

$$\begin{aligned} &B(\theta)(|\gamma_1\rangle + \xi_1|\beta_1\rangle)(|\gamma_2\rangle + \xi_2|\beta_2\rangle) \\ &= |\gamma_1\cos(\theta) + \gamma_2\sin(\theta)\rangle_t \otimes |-\gamma_1\sin(\theta) + \gamma_2\cos(\theta)\rangle_r \\ &\quad + \xi_2|\gamma_1\cos(\theta) + \beta_2\sin(\theta)\rangle_t \\ &\quad \otimes |-\gamma_1\sin(\theta) + \beta_2\cos(\theta)\rangle_r \\ &\quad + \xi_1|\beta_1\cos(\theta) + \gamma_2\sin(\theta)\rangle_t \\ &\quad \otimes |-\beta_1\sin(\theta) + \gamma_2\cos(\theta)\rangle_r \\ &\quad + \xi_1\xi_2|\beta_1\cos(\theta) + \beta_2\sin(\theta)\rangle_t \\ &\quad \otimes |-\beta_1\sin(\theta) + \beta_2\cos(\theta)\rangle_r. \end{aligned} \tag{90}$$

Using Eqs. (81), (86), and (90) in the optical arrangement shown in Fig. 14, and considering for reasons of simplicity a 50:50 beam splitter (i.e., $|\alpha_1\rangle = |\alpha_2\rangle$ for

$\theta = \pi/4$), the output field state $|\psi_f\rangle$ reads

$$
\begin{aligned}
|\psi_f\rangle = {}& \left| \frac{1}{\sqrt{2}}[\alpha_1(1 + e^{i\varphi}) + \chi_1 + \chi_2 e^{i\varphi}] \right\rangle_t \otimes \left| \frac{1}{\sqrt{2}}[-\alpha_1(1 - e^{i\varphi}) + \chi_1 + \chi_2 e^{i\varphi}] \right\rangle_r \\
& + \xi_2 \left| \frac{1}{\sqrt{2}}[\alpha_1(1 + e^{i\varphi}) + \chi_1] \right\rangle_t \otimes \left| \frac{1}{\sqrt{2}}[-\alpha_1(1 - e^{i\varphi}) + \chi_1] \right\rangle_r \\
& + \xi_1 \left| \frac{1}{\sqrt{2}}[\alpha_1(1 + e^{i\varphi}) + \chi_2 e^{i\varphi}] \right\rangle_t \otimes \left| \frac{1}{\sqrt{2}}[-\alpha_1(1 - e^{i\varphi}) + \chi_2 e^{i\varphi}] \right\rangle_r \\
& + \xi_1 \xi_2 \left| \frac{1}{\sqrt{2}}[\alpha_1(1 + e^{i\varphi})] \right\rangle_t \otimes \left| \frac{1}{\sqrt{2}}[-\alpha_1(1 - e^{i\varphi})] \right\rangle_r .
\end{aligned}
\tag{91}
$$

The above expression is an entangled coherent state that can be controlled by the variables χ_1, χ_2 (and consequently ξ_1, ξ_2), and φ. We note that by performing measurements over one of the modes, one can generate coherent state superpositions involving more than two coherent states.

4. Optical quantum state characterization

The characterization of the optical light state is a large chapter in quantum optics and is practically impossible to address completely in a single section of a manuscript. For this reason, here we focus in one of the most commonly used methods named quantum tomography [127, 128], which relies on the use of a homodyne detection technique [139] (unit 4 in Fig. 9).

According to classical electrodynamics, the mode of E_{in} can be decomposed into two quadrature components x and p oscillating with a $\pi/2$ phase difference. This is because $E_{\text{in}}(t) = (E_0 e^{i\varphi} e^{-i\omega t} + E_0^* e^{-i\varphi} e^{i\omega t}) = \frac{1}{2}(\alpha e^{-i\omega t} + \alpha^* e^{i\omega t}) = \cos(\omega t)X + \sin(\omega t)P$, where $\alpha = E_0 e^{i\varphi} = X + iP$, $\alpha^* = E_0^* e^{-i\varphi} = X - iP$ with $X = \text{Re}[\alpha] = \frac{1}{2}(\alpha + \alpha^*)$, $P = \text{Im}[\alpha] = (\alpha - \alpha^*)/2i$, and E_0 the field amplitude. Following the canonical quantization procedure, the electric field operator $\hat{E}_{\text{in}}(t) = E_0(\hat{a}e^{-i\omega t} + \hat{a}^\dagger e^{i\omega t})$ reads

$$
\hat{E}_{\text{in}}(t) = \sqrt{2}E_0(\cos(\omega t)\hat{x} + \sin(\omega t)\hat{p}), \tag{92}
$$

where $\hat{x} = (\hat{a} + \hat{a}^\dagger)/\sqrt{2}$ and $\hat{p} = (\hat{a} - \hat{a}^\dagger)/i\sqrt{2}$ are the noncommuting quadrature field operators, and $\hat{a}$, $\hat{a}^\dagger$ are the photon annihilation and creation operators, respectively. Operators $\hat{x}$ and $\hat{p}$ are the analogues to the position and momentum operators of a particle in a harmonic potential, and satisfy the commutation and uncertainty relations $[\hat{x}, \hat{p}] = i$ and $\Delta x \Delta p \geq \frac{1}{2}$, respectively.

In unit 4 of Fig. 9, E_{in} is the field of the state to be characterized. The E_{in} is spatiotemporally overlapped on a BS with the field of a local oscillator (E_r) coming from the second branch of the interferometer that introduces a controllable delay $\Delta\tau$ (phase shift φ) between the E_r and E_{in} fields. An important requirement for the applicability of

the method is that the photon number of the local oscillator field should be much larger than that of E_{in} to be characterized (for details, see Ref. [140]). The fields after the BS are detected by a balanced differential photodetection system consisting of two identical photodiodes (PDs), which provides at each value of φ the photocurrent difference i_φ. Setting the delay stage around $\Delta\tau \approx 0$, the characterization of the quantum state of light can be achieved by recording, for each shot, the value of i_φ as a function of φ. The beauty of the homodyne detection scheme [139] is that it provides access to the measurement of the values of the field quadrature. The values of the photocurrent difference i_φ are directly proportional to the measurement of the electric field operator, i.e.,

$$
\hat{E}_{\text{in}}(\varphi) \propto \hat{x}_\varphi = \cos(\varphi)\hat{x} + \sin(\varphi)\hat{p}. \tag{93}
$$

The unknown proportionality factor between the measured photocurrent and the quadrature values in Eq. (93) can be obtained by using the condition that the variance of the vacuum state is $1/2$, as for the vacuum state $\langle \hat{x}_\varphi \rangle = 0$, and $(\Delta x_\varphi)^2 = 1/2$. In other words, the homodyne data are scaled according to the measured vacuum state quadrature noise. Experimentally, that is all that someone has to do in order to characterize the light state. This is because repeated measurements of $\hat{x}_\varphi$ at each φ provides the probability distribution $P_\varphi(x_\varphi) = \langle x_\varphi | \hat{\rho} | x_\varphi \rangle$ of its eigenvalues x_φ, where $\hat{\rho} \equiv |\phi\rangle\langle\phi|$ is the density operator of the light state to be characterized and $|x_\varphi\rangle$ the eigenstate with eigenvalue x_φ. The density matrix $\hat{\rho}$, which provides complete information about the light state, can be obtained in the Fock basis by calculating the matrix elements ρ_{nm} using an iterative *maximum-likelihood* procedure beautifully described in Ref. [141]. Having these values, the mean photon number of the light state can be obtained by the diagonal elements ρ_{nn} of the density matrix $\hat{\rho}$, and the relation $\langle n \rangle = \sum n \rho_{nn}$.

One of the most complete and commonly used ways to visualize the quantum character of light states is via the quasiprobability distribution in phase space (x, p), namely,

the Wigner function $W(x,p)$, which has been extensively addressed over the years in an enormous number of research articles and books (see, for instance, Refs. [139, 142–145]). What is important to be mentioned here is that: (a) the marginal distributions $P(x) = \langle x|\hat{\rho}|x\rangle = \int_{-\infty}^{+\infty} dp\, W(x,p)$ and $P(p) = \langle p|\hat{\rho}|p\rangle = \int_{-\infty}^{+\infty} dx\, W(x,p)$ yield the position and momentum distributions, respectively, and (b) if we introduce a phase shift φ, the x and p components rotate by φ in phase space via the operator $\hat{U}(\varphi)$ shown in Eq. (86). Taking this into account, the equation that connects the $P_\varphi(x_\varphi)$ with $W(x,p)$ for each φ is

$$P_\varphi(x_\varphi) = \langle x|\hat{U}(\varphi)\hat{\rho}\hat{U}^\dagger(\varphi)|x\rangle$$
$$= \int_{-\infty}^{+\infty} dp_\varphi\, W(x_\varphi \cos\varphi - p_\varphi \sin\varphi, x_\varphi \sin\varphi$$
$$+ p_\varphi \cos\varphi), \qquad (94)$$

where $x_\varphi = x\cos\varphi + p\sin\varphi$ and $p_\varphi = -x\sin\varphi + p\cos\varphi$. The above equation is called the *Radon transformation* and has been extensively studied in the theory of tomographic imaging [146], while the inverse *Radon transformation*, implemented via the standard filtered backprojection algorithm, is the key tool in quantum state tomography and quantum state reconstruction [127,144, and references therein]. Hence, the Wigner function can be reconstructed by applying the algorithm directly to the quadrature values $x_{\varphi,k}$, using the formula $W(x,p) \simeq (1/2\pi^2 N)\sum_{k=1}^{N} K(x \cdot \cos(\varphi_k) + p \cdot \sin(\varphi_k) - x_{\varphi,k})$ [127], where N is the number of the recorded quadrature-phase pairs $(x_{\varphi,k}, \varphi_k)$. In the previous expression, k is the index of each value and $K(z) = \frac{1}{2}\int_{-\infty}^{\infty} d\xi\, |\xi| \exp(i\xi z)$ is called the integration kernel with $z = x \cdot \cos(\varphi_k) + p \cdot \sin(\varphi_k) - x_{\varphi,k}$. The numerical implementation of the integration kernel requires the replacement of the infinite integration limits with a finite cutoff k_c. In order to reduce the numerical artifacts (rapid oscillations) and allow the details of the Wigner function to be resolved, the value of k_c is typically set to be around $k_c \sim 4$. Alternatively, the $W(x,p)$ can also be obtained using the density matrix formalism [141,147].

In the following, we provide three characteristic examples of the homodyne traces, and their corresponding Wigner functions as have been calculated for optical coherent, "cat", and "kittenlike" states. These cases have been experimentally measured in Refs. [90,92] by means of the arrangement shown in Fig. 9. In Fig. 15 we show the calculated homodyne trace (left panel) and the Wigner function (right panel) of a coherent state. This corresponds to the case where the HHG process is switched off. The calculation is performed using a coherent state $|\alpha\rangle$ of amplitude $|\alpha| = 2$. In this case, $\hat{\rho} \equiv |\alpha\rangle\langle\alpha|$ and therefore the mean value $\langle \hat{x}_\varphi \rangle = \langle \alpha|\hat{x}_\varphi|\alpha\rangle$ exhibits an oscillation with $\langle \hat{x}_\varphi \rangle = |\alpha|\cos\varphi$. Furthermore, the P_φ defined in Eq. (94) and the quantum fluctuation [which is the same as the vacuum state
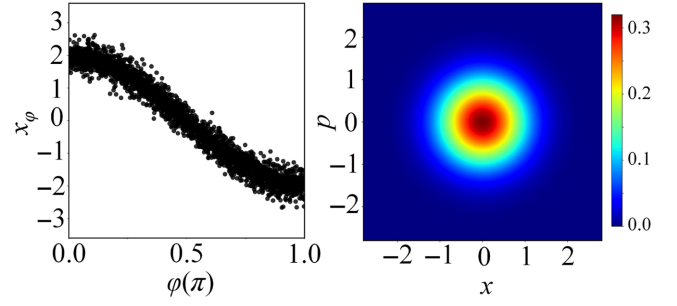

FIG. 15. Quantum tomography of an optical coherent state $|\alpha\rangle$. In the left panel we show the calculated homodyne detection signal x_ϕ, while the corresponding Wigner function centered at $|\alpha| = 2$ is shown in the right panel.

$(\Delta x_\varphi)^2 = 1/2$] remains constant along the cycle. All these characteristic features are shown by the Wigner function that depicts a Gaussian distribution given by

$$W(\beta) = \frac{2}{\pi} e^{-2|\beta-\alpha|^2}. \qquad (95)$$

In the above equation we have used the transformations $x \equiv \mathrm{Re}[\beta - \alpha]$ and $p \equiv \mathrm{Im}[\beta - \alpha]$ (where β is a variable), which centers the Wigner function at the origin since, for $\beta = \alpha$, $x = 0$, and $p = 0$. This is a convenient way to plot a Wigner function, as well as writing its expression in a more compact form.

The situation changes dramatically when the HHG process and the QS are switched on. In Fig. 16 we show the calculated homodyne traces (left panels) and the corresponding Wigner functions (right panels) of an optical "catlike" [Figs. 16(a) and 16(b)] and a "kittenlike" [Figs. 16(c) and 16(d)] state created when we introduce conditioning on the HHG process. In Figs. 16(a) and 16(b), the calculation is performed using the optical "cat" state $|\phi_c\rangle = |\alpha + \chi\rangle - \xi_{(IR)}|\alpha\rangle$ shown in Eq. (81) with $|\alpha| = 2$ and $|\chi| = 0.8$. In Figs. 16(c) and 16(d), the value of $|\chi|$ has been reduced to 0.1. In both cases, $\hat{\rho} = |\phi_c\rangle\langle\phi_c|$ and the mean value $\langle \hat{x}_\varphi \rangle = \langle \phi_c|\hat{x}_\varphi|\phi_c\rangle$ exhibits an oscillation with $\langle \hat{x}_\varphi \rangle = \sqrt{\langle n\rangle}\cos\varphi$. On the other hand, and contrarily to what we saw in the case of a coherent state, P_φ changes along the cycle and depicts a minimum around the center of the quantum fluctuation that is larger than the vacuum state. All these characteristic features are shown in the equation of the Wigner function, which reads

$$W(\beta) = \frac{2}{\pi N}[e^{-2|\beta-\alpha-\chi|^2} + e^{-|\chi|^2}e^{-2|\beta-\alpha|^2}$$
$$- (e^{2(\beta-\alpha)\chi^*} + e^{2(\beta-\alpha)^*\chi})e^{-|\chi|^2}e^{-2|\beta-\alpha|^2}], \quad (96)$$

where $N = 1 - e^{-|\chi|^2}$ is the normalization factor for Eq. (81). The Wigner function depicts the features of a genuine optical "cat" ("kitten" for $\chi = 0.1$) state as it has
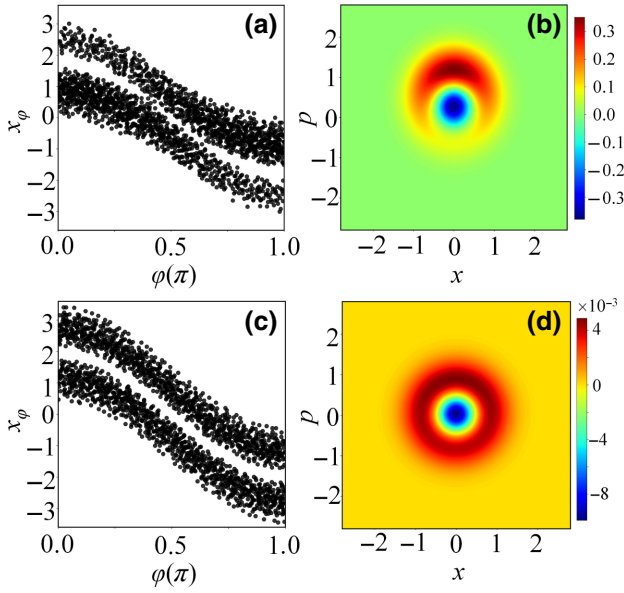
FIG. 16. Quantum tomography of optical "catlike" CSS [(a) and (b)] and "kittenlike" CSS [(c) and (d)] states created when the HHG and the QS are switched on. The left panels show the calculated homodyne detection signal x_ϕ and the right panels the corresponding Wigner functions centered at $|\alpha|$. The calculations are preformed using state $|\phi_c\rangle = |\alpha + \chi\rangle - \xi_{(IR)}|\alpha\rangle$ (with $|\alpha| = 2$) created by conditioning on the HHG process. The value of $|\chi|$ is set at 0.8 for the optical "catlike" state [(a) and (b)] and reduced to 0.1 for the "kittenlike" state [(c) and (d)].

a ringlike shape with a minimum around the center, and shows pronounced nonclassical signatures by means of its negative values.

5. Analysis of an experimentally reconstructed Wigner function

Obtaining quantitative information about the nonclassicality of the optical coherent state superposition measured by a quantum tomography method requires optimization k_c to be used to reconstruct the Wigner function and an error analysis. Both are associated with the number of points of the measured homodyne detection signal x_ϕ and the error introduced by the balanced detector of the homodyne detection system in the measurement of the photon number.

A convenient way to estimate the error is to use the Wigner function of a coherent state [92]. In this case the error can be obtained by comparing (subtracting) the ideal Wigner function of a coherent state with the Wigner function of the state reconstructed from the experimental data. Figure 17(a) shows how this procedure can be used to find the optimum value of k_c and minimize the error of the amplitude of the reconstructed Wigner function $W(x, p)$. The same procedure can be used for obtaining the error in the mean photon number. This can be done using the density matrix elements ρ_{nm} in the Fock basis $|n\rangle$, where
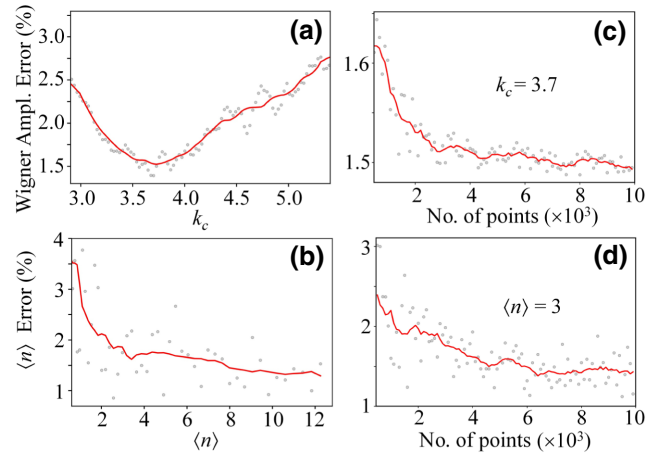

FIG. 17. (a) Dependence of the error amplitude of a reconstructed Winger function of a coherent state on k_c, using a homodyne trace with about 10^4 points for $0 \leq \phi \leq \pi$. (b) Dependence of the accuracy of measuring the mean photon number on the mean photon number of the light state. (c) Dependence of the Wigner function amplitude error on the number of points of the measured homodyne detection signal x_ϕ for $k_c \approx 3.7$. (d) Dependence of the accuracy of measuring the mean photon number of the light state on the number of points of the measured homodyne detection signal x_ϕ for $\langle n \rangle = 3$. In all graphs, the red solid line is a 15-point running average of the data (gray points). Panels (a) and (b) are reproduced from Ref. [92].

the mean photon number is obtained from the diagonal elements ρ_{nn} and the relation $\langle n \rangle = \sum n \rho_{nn}$. Figure 17(b) shows the dependence of the accuracy of measuring the photon number $\langle n \rangle$ on the mean photon number $\langle n \rangle$ of the light state [Error(%) = $|\langle n_{rec}\rangle - \langle n_{th}\rangle|/\langle n_{th}\rangle$, where $\langle n_{rec}\rangle$ is the mean photon number of a coherent state calculated using the number of data points of the measured homodyne detection signal x_ϕ, and $\langle n_{th}\rangle$ is the mean photon-number value of an ideal coherent state]. As shown in Fig. 17(b), this procedure can be repeated for coherent states of different photon-number values. The dependence of the Wigner function amplitude and mean photon-number errors on the number of points of the measured homodyne detection signal x_ϕ is shown in Figs. 17(c) and 17(d) for $k_c \approx 3.7$ and $\langle n \rangle = 3$, respectively. A homodyne trace that contains $\geq 5 \times 10^3$ measured x_ϕ values (for $0 \leq \phi \leq \pi$) results in a Wigner function amplitude and mean photon-number error $\leq 1.5\%$.

After the error analysis, the nonclassicality of the measured light state can be obtained by quantitatively evaluating its quantum features (such as its negativity) using the reconstructed Wigner function. The negativity is associated with the contrast of the fringe pattern created by quantum interference effects between the coherent states participating in the coherent state superposition. One of the reasons why the negativity can be reduced compared to the ideal case is the presence of decoherence effects on

the coherent state superposition after its creation. Although the optical coherent state superpositions can be considered as (almost) decoherence-free compared to the particle state superposition, the presence of optical losses during the propagation in optical elements affects the nonclassicality of these light states. This leads to a Wigner function with reduced negativity or reduced fringe contrast. Also, the influence of the decoherence effects on the nonclassicality of the state depends on the difference between the coherent states in the superposition χ. Hence, large traditional cat states ($|\alpha\rangle \pm |-\alpha\rangle$) are more sensitive to decoherence effects. The decoherence can be quantitatively studied using a noise model that introduces photon losses due to the interaction with a Gaussian reservoir [92,148], via the von Neumann entropy S, or using the fidelity F (see, e.g., Ref. [149]).

VI. DISCUSSION

The interaction of intense laser fields with matter leads to a highly nonlinear electronic response, simultaneously influences the electromagnetic field by generating radiation in the previously unpopulated field modes, and leads to a backaction on the fundamental mode that drives the process. Furthermore, the interaction induces correlations among the modes participating in the process. With the full quantum electrodynamical description of intense laser-matter interaction introduced in this tutorial, we were able to explicitly show how the two most common processes of high-harmonic generation and above-threshold ionization influence the quantum state of the electromagnetic field modes. Utilizing conditioning procedures on the different processes allowed us to perform quantum state engineering protocols for generating nonclassical optical field states with novel properties, such as high photon number, extending towards the extreme wavelength regime and using ultrashort light pulses.

The fully quantized descriptions of HHG and ATI processes allow us to obtain further insights into the dynamics of intense laser-matter interaction, from a novel perspective by taking into account the quantum nature of the electromagnetic field. This allows us to answer questions about the nonclassical properties of the electromagnetic field, and to investigate the backaction of the interaction on the driving laser field in intense laser-matter interaction. In particular, we uncovered dynamical changes of the electromagnetic field that could not be addressed by previous semiclassical theory.

We introduced quantum electrodynamical descriptions of the HHG and ATI processes considering the natural continuum of electromagnetic field modes. Considering a conditioning procedure on the emission of harmonic radiation leads to entangled coherent states, and coherent state superposition with nonclassical signatures.

We obtained the quantum state of the EM field for the conditioning procedure on ATI, which allowed us to obtain the backaction on the fundamental mode. We emphasize that the backaction on the EM field due to the electron dynamics in the ATI process can be decomposed into three steps. First, the bound electron wave function oscillates in the field, leading to a shift in the EM field modes themselves. In the second step, the electron transitions from the ground state to the continuum state, which influences the EM field state due to the coupling of the dipole transition matrix element with the electric field operator. In the last step, after ionization, the electron is driven by the field, leading to a shift in the EM field state due to the charge current associated with the electron's motion in the continuum.

With the ability to compute the EM field state conditioned on ATI, we obtain field observables of the driving laser mode (photon-number distribution and its mean value) to understand the underlying dynamics, and the backaction associated with the process. Interestingly, the direction of the electron propagation (determined by the initial electron momentum after ionization) determines whether the shift in the field state amplitude is in or out of phase, leading to an enhancement or depletion of the fundamental mode, respectively.

This quantum electrodynamical description, together with the conditioning procedures introduced in theory and experiment, gives rise to the opportunity to generate nonclassical field states. The applicability and use of those states towards a novel platform for quantum information science will be outlined in the next section.

VII. OUTLOOK

This paper provides a tutorial to a new emerging interdisciplinary area of science, in which ultrafast laser physics and attoscience merge with quantum optics and quantum information science. In this sense it serves as an invitation to researchers to join the efforts in this area, and for this reason, we devote special attention to the discussion of the outlook and possible future investigations. We decided to organize this section using the different levels: *operational* (concerning "day-to-day" generalization and continuations of the research discussed in this tutorial), *tactical* (connecting merging the present state-of-the-art status with quantum technologies, focused on detection, characterization, and applications of massive superposition and entangled states generated with the present framework), and *strategic* (relating to long-term goals and aims—the development of the new interdisciplinary platform for quantum technologies that merges quantum information, attoscience, and quantum optics).

A. Outlook—operational level

Typically, the operational plan describes the day-to-day running of the operation; in our case the new area of

science. The operational plan charts out "small steps" or milestones to achieve the higher level (tactical) goals within a realistic time frame. The present paper sets the QED framework for attoscience, and focuses on some applications related to conditional measurements of HHG and ATI in atomic media that lead to the generation of the massive Schrödinger cat states (massive superposition and entanglement states). There is an obvious ocean of possible generalizations, and applications of the present theory that can indeed be achieved on a "day-to-day" basis. Here we list a few.

(a) Even in the presently investigated schemes, there is plenty of place for further studies, such as, for instance, the role of the CEP, and there is a whole plethora of possibilities associated with using more complex polarization states (elliptic, time-dependent elliptic, locally chiral, etc.), combining polarization with two-color fields and structuring polarization in space (cf. Refs. [150–158]). This might lead to the creation of novel types of topological Schrödinger cats, very different from those discussed so far in the literature (cf. Ref. [159]).

(b) Another important consideration is the spin of the electron, which was overlooked until recently [160–164], where it has been shown that circular strong-field ionization produces spin-polarized electrons. As such, this process may be exploited to produce entanglement between the spin and the laser field. The electronic spin provides an additional degree of freedom useful in heading towards delivering quantum technologies, as the discrete spin can be more easily measured and manipulated than the continuous electronic degrees of freedom typically considered.

(c) The same QED theory, and conditioning methods, can be applied to multielectron processes in atoms (ionization in general, NSDI by the interplay between electron impact ionization, and resonant excitation with subsequent ionization). These can at least be analyzed using the SFA approach.

(d) The present framework can be extended to more complex targets such as molecules, where, e.g., chirality can lead to otherwise symmetry-forbidden electronic responses, like electronic motion perpendicular to the polarization plane [165], and electronic orbital angular momentum in ionization with linearly polarized light [166], thus expanding the spectrum of possible conditioning setups.

(e) A completely new avenue is to apply the present framework to solid-state and condensed matter systems. In the first place, this could be done for weakly correlated systems that can be described by semiconductor Bloch equations [31,45] or the little more flexible Wannier-Bloch approach [46]. The

next step would be to apply the present framework to imaging of topological, chiral, and/or strongly correlated systems, such as topological insulators [32,33] or high-T_c superconductors (cf. Ref. [50]).

B. Outlook—tactical level

In order to explore the creation of a new feasible platform for quantum technologies, one needs to clearly relate "what we have" to the basic aspects of quantum information science: detection, characterization, and finally, applications of generated quantum correlations and quantum entanglement. At this stage, experiments generate in a simplified view the massive superposition of the fundamental laser mode [90], or massively entangled states of several modes [91,93].

The next directions of research should then focus on the following topics.

(a) Detection and characterization methods of massive Schrödinger cat states. This is a formidable challenge [167], which, for large cats, is extremely demanding [129].

(b) These kinds of states are in the first place useful for quantum metrology in general [168–170], and on photonic platforms [171–173] in particular, and perhaps in quantum communications. It will thus be important to design concrete protocols for their applications.

C. Outlook—strategic level

On the strategic level we aim at developing a novel *quantum technology platform combining attoscience, quantum optics, and quantum information*. Each of these areas are already at a step where proof-of-principle experiments have been developed. The point is to create a new platform that is totally and intrinsically interdisciplinary. The research presented here, focused in theory and experiments on conditioning, is only a part of this general vision aimed at realizing a universal and firmly established tool to offer completely unknown solutions and developments, i.e., a set of stable and reproducible methods to generate massive entangled states and massive quantum superposition. Most, if not all of these methods, involve quantum electrodynamics of intense laser-matter interactions, i.e., the framework described in the present tutorial. Here is a more complete list of future research lines, related to these strategic objectives, aims, and goals.

(a) *Objective 1*: generation, characterization, and concrete applications in QT of entangled and quantum correlated states using conditioning methods.

(b) *Objective 2*: generation, characterization, and concrete applications in QT of entangled and quantum

correlated states in strong-field physics and attosecond science driven by quantum light; this includes driving by strongly squeezed light, light with orbital angular momentum (cf. Ref. [174]), effects on photoelectron orbital angular momentum [175], and more.

(c) *Objective 3*: generation, characterization, and concrete applications in QT of entangled and quantum correlated states in *Zerfall* processes, such as single [176–178] or double ionization (cf. Ref. [11]).

(d) *Objective 4*: studying quantitative and measurable effects of decoherence in attoscience by studying reduced density matrices of *Zerfall* products in ionization processes (cf. Refs. [179–181]).

The results of the present tutorial set up the basis for a road map toward this novel platform of attoscience, quantum optics, and quantum information science for quantum technologies.

APPENDIX A: FIELD COMMUTATION RELATIONS

The commutation relation between the canonical field variables $\mathbf{A}(\mathbf{r})$ and $\mathbf{\Pi}(\mathbf{r})$ defined respectively in Eqs. (3) and (5) is given by

$$[A_m(\mathbf{r}), \Pi_n(\mathbf{r}')] = i\hbar \delta_{mn}^{\perp}(\mathbf{r} - \mathbf{r}') \tag{A1}$$

with the transverse δ function

$$\delta_{mn}^{\perp}(\mathbf{r} - \mathbf{r}') = \frac{1}{(2\pi)^3} \int d^3 k \left[\delta_{mn} - \frac{k_m k_n}{k^2} \right] e^{i\mathbf{k} \cdot (\mathbf{r} - \mathbf{r}')}. \tag{A2}$$

These canonical conjugate field variables are related to the field operators $\mathbf{B} = \nabla \times \mathbf{A}$ and $\mathbf{E}^{\perp} = -\mathbf{\Pi}/\epsilon_0$ of the magnetic field and transverse part of the electric field, respectively. The free-field Hamiltonian H_f can then be expressed in terms of the physical operators

$$H_f = \frac{1}{2} \int d^3 r \left[\epsilon_0 \mathbf{E}^2(\mathbf{r}) + \frac{1}{\mu_0} \mathbf{B}^2(\mathbf{r}) \right], \tag{A3}$$

which has the same form as the energy of the classical electromagnetic field, and it is required that the observables obey the commutation relation

$$\left[E_m(\mathbf{r}), B_n(\mathbf{r}') \right] = -\epsilon_{\mathrm{mnl}} \frac{i\hbar}{\epsilon_0} \frac{\partial}{\partial x_l} \delta(\mathbf{r} - \mathbf{r}'). \tag{A4}$$

APPENDIX B: INTERACTION HAMILTONIAN

The minimal-coupling Hamiltonian (17) can be written in terms of the transformed dynamical variables from Eqs. (23) and (24) to obtain the multipolar-coupling Hamiltonian

$$\begin{aligned} H' = \frac{1}{2} \int d^3 r &\left\{ \frac{1}{\epsilon_0} [\mathbf{\Pi}'(\mathbf{r}) + \mathbf{P}_{\perp}(\mathbf{r})]^2 + \frac{1}{\mu_0} [\nabla \times \mathbf{A}(\mathbf{r})]^2 \right\} \\ &+ \sum_{\alpha} \left[\frac{1}{2m} \left\{ \mathbf{p}'_{\alpha} - e \int_0^1 ds\, s(\mathbf{r}_{\alpha} - \mathbf{R}_{\alpha}) \right. \right. \\ &\left. \left. \times [\nabla \times \mathbf{A}(\mathbf{R}_{\alpha} + s(\mathbf{r}_{\alpha} - \mathbf{R}_{\alpha}))] \right\}^2 + V_{\mathrm{at}}(\mathbf{r}_{\alpha}, \mathbf{R}_{\alpha})) \right], \end{aligned} \tag{B1}$$

where, as mentioned in Sec. III, $V_{at}(\mathbf{r}_\alpha, \mathbf{R}_\alpha)$ is the effective potential felt by the single active electron, and $\mathbf{\Pi}'$ and $\mathbf{p}'$ are given by Eqs. (23) and (24), respectively.

Using the mode expansion of the dynamical field variables of the transverse part of the electromagnetic field, the total Hamiltonian can be decomposed as

$$H' = H'_f + H'_{at} + H'_{int}, \tag{B2}$$

where the free-field Hamiltonian H'_f has the same form as Eq. (2) but in terms of the new mode operators

$$H'_f = \frac{1}{2}\int d^3r\left\{\frac{1}{\epsilon_0}\mathbf{\Pi}'^2(\mathbf{r}) + \frac{1}{\mu_0}[\nabla\times\mathbf{A}(\mathbf{r})]^2\right\}$$
$$= \sum_\mu\int d^3k\hbar\omega_k\left(a'^\dagger_{\mathbf{k}\mu}a'_{\mathbf{k}\mu} + \frac{1}{2}\right). \tag{B3}$$

We have separated the purely electronic (atomic or molecular) Hamiltonian

$$H'_{at} = \sum_\alpha\left[\frac{\mathbf{p}'^2_\alpha}{2m} + V_{at}(\mathbf{r}_\alpha, \mathbf{R}_\alpha) + \frac{1}{2\epsilon_0}\int d^3r\mathbf{P}^2_\perp(\mathbf{r})\right]$$
$$= \sum_\alpha\left[\frac{\mathbf{p}'^2_\alpha}{2m_\alpha} + \tilde{V}_{at}(\mathbf{r}_\alpha, \mathbf{R}_\alpha)\right], \tag{B4}$$

where $\tilde{V}_{at}(\mathbf{r}_\alpha, \mathbf{R}_\alpha)$ is the final effective potential for single active electrons that includes effects of polarization. Finally, the interaction Hamiltonian reads

$$H'_{int} = -\frac{e}{\epsilon_0}\sum_\alpha\int_0^1 ds(\mathbf{r}_\alpha - \mathbf{R}_\alpha)\cdot\mathbf{\Pi}'(\mathbf{R}_\alpha + s(\mathbf{r}_\alpha - \mathbf{R}_\alpha))$$
$$+ \frac{e}{2m}\sum_\alpha\int_0^1 ds\,s\{[(\mathbf{r}_\alpha - \mathbf{R}_\alpha)\times\mathbf{p}'_\alpha]$$
$$\times[\nabla\times\mathbf{A}(\mathbf{R}_\alpha + s(\mathbf{r}_\alpha - \mathbf{R}_\alpha))] + \text{H.c.}\}$$
$$+ \frac{e^2}{2m}\sum_\alpha\left\{\int_0^1 ds\,s(\mathbf{r}_\alpha - \mathbf{R}_\alpha)\right.$$
$$\left.\times[\nabla\times\mathbf{A}(\mathbf{R}_\alpha + s(\mathbf{r}_\alpha - \mathbf{R}_\alpha))]\right\}^2. \tag{B5}$$

The first term is the most relevant in our analysis since it couples the transverse displacement field $\mathbf{\Pi}'(\mathbf{r}) = -[\epsilon_0\mathbf{E}_\perp(\mathbf{r}) + \mathbf{P}_\perp(\mathbf{r})]$ with the atomic polarization $\mathbf{P}(\mathbf{r})$. The second and third terms describe the interaction of the paramagnetic magnetization with the magnetic induction field $\mathbf{B}(\mathbf{r}) = \nabla\times\mathbf{A}(\mathbf{r})$ and the diamagnetic energy of the system that is quadratic in the magnetic induction field, respectively.

APPENDIX C: HHG SPECTRUM

The coherent contribution to the HHG spectrum is proportional to

$$S(\omega_{\mathbf{k},\mu}) \propto \lim_{t\to\infty}|\chi_{\mathbf{k},\mu}(t)|^2 = \tilde{g}(k)^2 N|\boldsymbol{\epsilon}_{\mathbf{k},\mu}\cdot\langle\mathbf{d}(\omega_{\mathbf{k}})\rangle|^2$$
$$+ \tilde{g}(k)^2\sum_{\alpha\neq\alpha'}e^{-i\mathbf{k}(\mathbf{R}_\alpha - \mathbf{R}_{\alpha'})}\boldsymbol{\epsilon}_{\mathbf{k},\mu}\cdot\langle\mathbf{d}_\alpha(\omega_{\mathbf{k}})\rangle\boldsymbol{\epsilon}_{\mathbf{k},\mu}$$
$$\cdot\langle\mathbf{d}_{\alpha'}(\omega_{\mathbf{k}})\rangle^*, \tag{C1}$$

where we have assumed that each of the N atoms contributes equally to the HHG spectrum such that

$$\sum_{\alpha=\alpha'}|\boldsymbol{\epsilon}_{\mathbf{k},\mu}\cdot\langle\mathbf{d}_\alpha(\omega_{\mathbf{k}})\rangle|^2 = N|\boldsymbol{\epsilon}_{\mathbf{k},\mu}\cdot\langle\mathbf{d}(\omega_{\mathbf{k}})\rangle|^2. \tag{C2}$$

Assuming that the N atoms contribute equally to the HHG spectrum of course implies the additional assumption that all atoms see the same radiation field of the driving source. In realistic experiments this is almost never the case, and focal averaging over the spatial beam profile needs to be taken into account. However, for the concepts and methods introduced in this manuscript, this only plays a minor role since the postselection scheme does not depend on the particular structure of the HHG spectra, and holds for generic harmonic amplitudes $\chi_{\mathbf{k},\mu}$.

Following the same assumptions that lead to the dipole approximation, i.e., $\mathbf{k}\cdot\mathbf{R}_\alpha \ll 1$, and again assuming that all N atoms equally contribute to the HHG process, the second term in Eq. (C1) is given by

$$\tilde{g}(k)^2\sum_{\alpha\neq\alpha'}e^{-i\mathbf{k}(\mathbf{R}_\alpha - \mathbf{R}_{\alpha'})}\boldsymbol{\epsilon}_{\mathbf{k},\mu}\cdot\langle\mathbf{d}_\alpha(\omega_{\mathbf{k}})\rangle\boldsymbol{\epsilon}_{\mathbf{k},\mu}\cdot\langle\mathbf{d}_{\alpha'}(\omega_{\mathbf{k}})\rangle^*$$
$$= \tilde{g}(k)^2(N^2 - N)|\boldsymbol{\epsilon}_{\mathbf{k},\mu}\cdot\langle\mathbf{d}(\omega_{\mathbf{k}})\rangle|^2, \tag{C3}$$

such that the spectrum is given by

$$S(\omega_{\mathbf{k},\mu}) \propto \lim_{t\to\infty}|\chi_{\mathbf{k},\mu}(t)|^2 = \tilde{g}(k)^2N^2|\boldsymbol{\epsilon}_{\mathbf{k},\mu}\cdot\langle\mathbf{d}(\omega_{\mathbf{k}})\rangle|^2. \tag{C4}$$

APPENDIX D: DERIVATION OF ELECTRONIC TRANSITION MATRIX ELEMENTS

In the main part of the manuscript we need the time-dependent dipole transition matrix elements between the ground state $|g\rangle$ and a continuum state $|\mathbf{v}\rangle$, or between two different continuum states; see, for instance, Eq. (69) or (57), respectively. To obtain the transition matrix elements, we use the fact that $\mathbf{r}(t) = U^\dagger_{sc}(t)\mathbf{r}U_{sc}(t)$, and we further use the fact that the action of the propagator on the

electronic state is known from semiclassical theory [117],

$$\left|\psi_{g/\mathbf{v}}(t)\right\rangle = U_{\text{sc}}(t)\left|g/\mathbf{v}\right\rangle = e^{iI_p t/\hbar}$$

$$\times \left(a_{g/\mathbf{v}}(t)\left|g\right\rangle + \int d^3 v' b_{g/\mathbf{v}}(\mathbf{v}', t)\left|\mathbf{v}'\right\rangle \right),$$

(D1)

which are the solutions of the time-dependent Schrödinger equation with the ground state $|g\rangle$ or the continuum state $|\mathbf{v}\rangle$ as the initial condition, respectively.

1. Electron ground and continuum state population amplitudes

Amplitudes (D1) of the ground and continuum states obey the coupled differential equations

$$\frac{d}{dt}a_{g/\mathbf{v}}(t) = \frac{i}{\hbar}\int d^3 v' \mathbf{E}_{\text{cl}}(t) \cdot \mathbf{d}^*(\mathbf{v}') b_{g/\mathbf{v}}(\mathbf{v}', t),$$

(D2)

$$\frac{d}{dt}b_{g/\mathbf{v}}(\mathbf{v}', t) = -\frac{i}{\hbar}\left(\frac{\mathbf{v}'^2}{2m} + I_p\right)b_{g/\mathbf{v}}(\mathbf{v}', t) + \frac{i}{\hbar}\mathbf{E}_{\text{cl}}(t) \cdot \mathbf{d}(\mathbf{v}')a_{g/\mathbf{v}}(t)$$

$$+ e\mathbf{E}_{\text{cl}}(t) \cdot \nabla_{\mathbf{v}'} b_{g/\mathbf{v}}(\mathbf{v}', t) + i\mathbf{E}_{\text{cl}}(t) \cdot \int d^3 v'' b_{g/\mathbf{v}}(\mathbf{v}'', t)\mathbf{g}(\mathbf{v}', \mathbf{v}''),$$

(D3)

where $\mathbf{d}(\mathbf{v}') = -e\langle\mathbf{v}'|\mathbf{r}|g\rangle$. However, to solve this coupled differential equations, we perform the following approximation by neglecting rescattering events and only consider the contribution from direct electrons, i.e., we neglect the continuum-continuum transitions in Eq. (D3) [term with $\mathbf{g}(\mathbf{v}', \mathbf{v}'')$]. We can therefore solve the differential equation for the continuum amplitude with the initial condition $b_g(\mathbf{v}', t_0) = 0$ and $a_g(t_0) = 1$, i.e., the initial ground-state population

$$\frac{d}{dt}b_g(\mathbf{v}', t) = -\frac{i}{\hbar}\left(\frac{\mathbf{v}'^2}{2m} + I_p\right)b_g(\mathbf{v}', t) + \frac{i}{\hbar}\mathbf{E}_{\text{cl}}(t) \cdot \mathbf{d}(\mathbf{v}')a_g(t) + e\mathbf{E}_{\text{cl}}(t) \cdot \nabla_{\mathbf{v}'} b_g(\mathbf{v}', t),$$

(D4)

with the solution given by

$$b_g(\mathbf{p}', t) = \frac{i}{\hbar}\int_{t_0}^t dt' \mathbf{E}_{\text{cl}}(t') \cdot \mathbf{d}\left(\mathbf{p}' + \frac{e}{c}\mathbf{A}_{\text{cl}}(t')\right)\exp\left\{-\frac{i}{\hbar}S(\mathbf{p}', t, t')\right\}a_g(t'),$$

(D5)

where we have substituted the canonical momentum $\mathbf{p}' = m\mathbf{v}' - e\mathbf{A}(t)/c$, such that the gauge invariant kinetic momentum $m\dot{\mathbf{r}}(t) = \mathbf{p} + e\mathbf{A}(t)/c$ appears in the expression. With this, we denote by $S(\mathbf{p}, t, t')$ the semiclassical action given by

$$S(\mathbf{p}, t, t') = \int_{t'}^t dt''\left[\frac{1}{2m}\left(\mathbf{p}' + \frac{e}{c}\mathbf{A}_{\text{cl}}(t'')\right)^2 + I_p\right].$$

(D6)

This can now be substituted into the differential equation for the ground-state amplitude, Eq. (D2), and we obtain

$$\frac{d}{dt}a_g(t) = -\int_{t_0}^t dt' \gamma(t, t')a_g(t'),$$

(D7)

where

$$\gamma(t, t') = \frac{1}{\hbar^2}\int d^3 p \mathbf{E}_{\text{cl}}(t) \cdot \mathbf{d}^*\left(\mathbf{p} + \frac{e}{c}\mathbf{A}_{\text{cl}}(t)\right)\mathbf{E}_{\text{cl}}(t') \cdot \mathbf{d}\left(\mathbf{p} + \frac{e}{c}\mathbf{A}_{\text{cl}}(t')\right)\exp\left\{-\frac{i}{\hbar}S(\mathbf{p}, t, t')\right\}.$$

(D8)

We now assume that the rate of change of $a_g(t)$ is slow compared to the field, such that we can replace $a_g(t')$ by $a_g(t)$ in the integrand, and the solution is given by

$$a_g(t) = \exp\left\{-\int_{t_0}^t dt' W(t')\right\}a_g(t_0) = \exp\left\{-\int_{t_0}^t dt' W(t')\right\}$$

(D9)

with the ionization rate given by

$$W(t) = \int_{t_0}^{t} dt' \gamma(t, t').$$

(D10)

We further need the amplitudes with the continuum state as the initial condition $b_{\mathbf{v}}(\mathbf{v}', t_0) = \delta(\mathbf{v} - \mathbf{v}')$ and $a_{\mathbf{v}}(t_0) = 0$. The corresponding solution of Eq. (D4) for $b_{\mathbf{v}}(\mathbf{v}', t)$ is given by

$$b_{\mathbf{v}}(\mathbf{v}', t) = \frac{i}{\hbar} \int_{t_0}^{t} dt' \mathbf{E}_{\mathrm{cl}}(t') \cdot \mathbf{d}\left(\mathbf{p}' + \frac{e}{c}\mathbf{A}_{\mathrm{cl}}(t')\right) \exp\left\{-\frac{i}{\hbar}S(\mathbf{p}', t, t')\right\} a_{\mathbf{v}}(t') + \exp\left\{-\frac{i}{\hbar}S(\mathbf{p}', t, t_0)\right\} \delta(\mathbf{v} - \mathbf{v}'),$$

(D11)

where the last term takes into account the initial condition $b_{\mathbf{v}}(\mathbf{v}', t_0) = \delta(\mathbf{v} - \mathbf{v}')$. Under the same assumptions for the solution of the differential equation of $a_{\mathbf{v}}(t)$ in Eq. (D2), we find that, for $a_{\mathbf{v}}(t_0) = 0$,

$$a_{\mathbf{v}}(t) = \frac{i}{\hbar} \int d^3v' \int_{t_0}^{t} dt' \mathbf{E}_{\mathrm{cl}}(t') \cdot \mathbf{d}^*(\mathbf{v}') \exp\left\{-\frac{i}{\hbar}S(\mathbf{p}', t', t_0)\right\} \exp\left\{-\int_{t'}^{t} d\tau W(\tau)\right\} \delta(\mathbf{v} - \mathbf{v}')$$

$$= \frac{i}{\hbar} \int_{t_0}^{t} dt' \mathbf{E}_{\mathrm{cl}}(t') \cdot \mathbf{d}^*(\mathbf{v}) \exp\left\{-\frac{i}{\hbar}S(\mathbf{p}, t', t_0)\right\} \exp\left\{-\int_{t'}^{t} d\tau W(\tau)\right\}.$$

(D12)

We assume that the probability of recombination to the ground state is small when the electron is initially in the continuum. This means that we approximate $a_{\mathbf{v}}(t) \approx 0$, which simplifies the amplitude of the continuum population

$$b_{\mathbf{p}}(\mathbf{p}', t) = \exp\left\{-\frac{i}{\hbar}S(\mathbf{p}', t, t_0)\right\} \delta(\mathbf{p} - \mathbf{p}').$$

(D13)

We further assume that the depletion of the ground state can be neglected such that $a_g(t) \simeq 1$ and accordingly the continuum population (D5) reads

$$b_g(\mathbf{p}', t) = \frac{i}{\hbar} \int_{t_0}^{t} dt' \mathbf{E}_{\mathrm{cl}}(t') \cdot \mathbf{d}\left(\mathbf{p}'(t) + \frac{e}{c}\mathbf{A}_{\mathrm{cl}}(t')\right) \exp\left\{-\frac{i}{\hbar}S(\mathbf{p}, t, t')\right\}.$$

(D14)

We have expressed both amplitudes in terms of the gauge invariant kinetic momentum $\mathbf{p} = \mathbf{v} - e\mathbf{A}(t)/c$.

2. Bound-continuum transition matrix element

In Eq. (69) we need the time-dependent transition matrix element between the ground state $|g\rangle$ and the continuum state $\mathbf{v}_\alpha$ for the process of ATI. We can use Eq. (D1), and have

$$\langle \mathbf{v}| \mathbf{r}(t) |g\rangle = \langle \psi_{\mathbf{v}}(t)| \mathbf{r} |\psi_g(t)\rangle \simeq \int d^3v' b_{\mathbf{v}}^*(\mathbf{v}', t) \langle \mathbf{v}' | \mathbf{r} |g\rangle,$$

(D15)

where we have used the facts that $a_{\mathbf{v}}(t) \approx 0$ and $a_g(t) \simeq 1$. We have also further neglected continuum-continuum transition matrix elements. Inserting Eq. (D13) we have

$$\langle \mathbf{v}| \mathbf{r}_\alpha(t) |g\rangle \simeq \exp\left\{\frac{i}{\hbar}S(\mathbf{p}, t, t_0)\right\} \left\langle \mathbf{p} + \frac{e}{c}\mathbf{A}(t)\middle| \mathbf{r} |g\right\rangle.$$

(D16)

3. Continuum-continuum transition matrix element

For the time-dependent transition matrix element between the two continuum states in Eq. (57), we have

$$\langle \mathbf{v}| \mathbf{r}(t) |\mathbf{v}'\rangle = \langle \psi_{\mathbf{v}}(t)| \mathbf{r} |\psi_{\mathbf{v}'}(t)\rangle \simeq \int d^3v'' \int d^3v''' b_{\mathbf{v}}^*(\mathbf{v}'', t) b_{\mathbf{v}'}(\mathbf{v}''', t) \langle \mathbf{v}'' | \mathbf{r} |\mathbf{v}'''\rangle,$$

(D17)

where we have again used the facts that $a_{\mathbf{v}}(t) \approx 0$ and $a_g(t) \simeq 1$.

APPENDIX E: FIELD OBSERVABLES FOR DIRECT ATI

The pure state of the EM field conditioned on ATI (68) is given by

$$|\phi_{\text{ATI}}(t, \mathbf{p})\rangle = \frac{-ie}{\hbar} \int_{t_0}^{t} dt' \prod_{\mathbf{k},\mu} e^{i\varphi_{\mathbf{k}\mu}(t,t',\mathbf{v}_\alpha)} D[\delta_\alpha(t,t',\omega_k,\mathbf{v}_\alpha)] \mathbf{E}_Q(t', \mathbf{R}_\alpha) \cdot \langle \mathbf{v}_\alpha | \mathbf{r}_\alpha(t') | g \rangle$$

$$\bigotimes_{\mathbf{k},\mu \simeq \mathbf{k}_{L,\mu}} |\chi_{\mathbf{k},\mu}(t')\rangle \bigotimes_{\mathbf{k},\mu \gg \mathbf{k}_{L,\mu}} |\chi_{\mathbf{k},\mu}(t')\rangle. \tag{E1}$$

We can now use

$$\prod_{\mathbf{k},\mu} e^{i\varphi_{\mathbf{k}\mu}(t,t',\mathbf{v}_\alpha)} D[\delta_\alpha(t,t',\omega_k,\mathbf{v}_\alpha)] \mathbf{E}_Q(t', \mathbf{R}_\alpha) = [\mathbf{E}_Q(t', \mathbf{R}_\alpha) - \mathbf{E}_\delta(t', \mathbf{R}_\alpha)] \prod_{\mathbf{k},\mu} e^{i\varphi_{\mathbf{k}\mu}(t,t',\mathbf{v}_\alpha)} D[\delta_\alpha(t,t',\omega_k,\mathbf{v}_\alpha)], \tag{E2}$$

where

$$\mathbf{E}_\delta(t', \mathbf{R}_\alpha) = i \sum_\mu \int d^3k \tilde{g}(k) \epsilon_{k\mu} \left[\delta_\alpha(t,t',\omega_k,\mathbf{v}_\alpha) e^{-i\omega_k t + i\mathbf{k}\cdot\mathbf{R}_\alpha} - \text{c.c.} \right] \tag{E3}$$

such that the state of the field now reads

$$|\phi_{\text{ATI}}(t, \mathbf{p})\rangle = \frac{-ie}{\hbar} \int_{t_0}^{t} dt' [\mathbf{E}_Q(t', \mathbf{R}_\alpha) - \mathbf{E}_\delta(t', \mathbf{R}_\alpha)] \cdot \langle \mathbf{v}_\alpha | \mathbf{r}_\alpha(t') | g \rangle$$

$$\times \left[\bigotimes_{\mathbf{k},\mu \simeq \mathbf{k}_{L,\mu}} e^{i[\varphi_{\mathbf{k}\mu}(t,t',\mathbf{v}_\alpha) + \varphi_{\mathbf{k}\mu}^{\chi,\delta}(t,t')]} |\chi_{\mathbf{k},\mu}(t') + \delta_\alpha(t,t',\omega_k,\mathbf{v}_\alpha)\rangle \right]$$

$$\times \left[\bigotimes_{\mathbf{k},\mu \gg \mathbf{k}_{L,\mu}} e^{i[\varphi_{\mathbf{k}\mu}(t,t',\mathbf{v}_\alpha) + \varphi_{\mathbf{k}\mu}^{\chi,\delta}(t,t')]} |\chi_{\mathbf{k},\mu}(t') + \delta_\alpha(t,t',\omega_k,\mathbf{v}_\alpha)\rangle \right], \tag{E4}$$

where

$$\varphi_{\mathbf{k}\mu}^{\chi,\delta}(t,t') = \text{Im}[\delta_\alpha(t,t',\omega_k,\mathbf{v}_\alpha)\chi_{\mathbf{k},\mu}^*(t')]. \tag{E5}$$

We can now do the transformation back to the original laboratory frame

$$|\Phi_{\text{ATI}}(t, \mathbf{p})\rangle = e^{-iH_f t} D(\alpha_{\mathbf{k}_L}) |\phi_{\text{ATI}}(t, \mathbf{p})\rangle, \tag{E6}$$

and we find that

$$|\Phi_{\text{ATI}}(t, \mathbf{p})\rangle = \frac{-ie}{\hbar} \int_{t_0}^{t} dt' [\mathbf{E}_Q(t' - t, \mathbf{R}_\alpha) - \mathbf{E}_\delta(t', \mathbf{R}_\alpha) - \mathbf{E}_{\text{cl}}(t', \mathbf{R}_\alpha)] \cdot \langle \mathbf{v}_\alpha | \mathbf{r}_\alpha(t') | g \rangle$$

$$\bigotimes_{\mathbf{k},\mu \simeq \mathbf{k}_{L,\mu}} e^{i[\varphi_{\mathbf{k}\mu}(t,t',\mathbf{v}_\alpha) + \varphi_{\mathbf{k}\mu}^{\chi,\delta}(t,t') + \varphi_{\mathbf{k}\mu}^{\chi,\delta,\alpha}(t,t')]} \times |[\alpha_{\mathbf{k}_L} + \chi_{\mathbf{k},\mu}(t') + \delta_\alpha(t,t',\omega_k,\mathbf{v}_\alpha)] e^{-i\omega_{\mathbf{k}} t}\rangle$$

$$\bigotimes_{\mathbf{k},\mu \gg \mathbf{k}_{L,\mu}} e^{i[\varphi_{\mathbf{k}\mu}(t,t',\mathbf{v}_\alpha) + \varphi_{\mathbf{k}\mu}^{\chi,\delta}(t,t')]} |[\chi_{\mathbf{k},\mu}(t') + \delta_\alpha(t,t',\omega_k,\mathbf{v}_\alpha)] e^{-i\omega_{\mathbf{k}} t}\rangle, \tag{E7}$$

where

$$\varphi_{\mathbf{k}\mu}^{\chi,\delta,\alpha}(t,t') = \text{Im}\{\alpha_{\mathbf{k}_L}[\delta_\alpha^*(t,t',\omega_k,\mathbf{v}_\alpha) + \chi_{\mathbf{k},\mu}^*(t')]\}. \tag{E8}$$

We have further used the fact that

$$e^{-iH_f t}\mathbf{E}_Q(t', \mathbf{R}_\alpha)e^{iH_f t} = \mathbf{E}_Q(t' - t, \mathbf{R}_\alpha)$$

$$= i\sum_\mu \int d^3k\tilde{g}(k)\epsilon_{k\mu}[a_{k\mu}e^{-i\omega_k(t'-t)+i\mathbf{k}\cdot\mathbf{R}_\alpha} - \text{H.c.}]. \tag{E9}$$

State (E7) is the field state conditioned on ATI with a single electron momentum in the laboratory frame. We now project this state onto the harmonic vacuum $|\{0\}_{\text{HH}}\rangle$ in order to obtain the state of the driving field mode in the situation where no harmonic radiation is generated. We thus find that

$$|\Phi_{\text{ATI}}^{\mathbf{k}_L}(t, \mathbf{p})\rangle = \langle\{0\}_{\text{HH}}|\,|\Phi_{\text{ATI}}(t, \mathbf{p})\rangle$$

$$= \frac{-ie}{\hbar}\int_{t_0}^t dt'\left[\mathbf{E}_{Q,\mathbf{k}_L}(t' - t, \mathbf{R}_\alpha) + i\sum_\mu \int d^3k\Theta(\mathbf{k}_{\text{HH}})\tilde{g}(k)\epsilon_{\mathbf{k},\mu}e^{-i\omega_k t'+i\mathbf{k}\cdot\mathbf{R}_\alpha}[\chi_{\mathbf{k},\mu}(t') + \delta_\alpha(t, t', \omega_k, \mathbf{v}_\alpha)]\right]$$

$$- [\mathbf{E}_\delta(t', \mathbf{R}_\alpha) - \mathbf{E}_{\text{cl}}(t', \mathbf{R}_\alpha)]\cdot\langle\mathbf{v}_\alpha|\,\mathbf{r}_\alpha(t')\,|g\rangle\prod_{\mathbf{k},\mu\gg\mathbf{k}_{L,\mu}}[e^{i[\varphi_{\mathbf{k}\mu}(t,t',\mathbf{v}_\alpha)+\varphi_{\mathbf{k}\mu}^{\chi,\delta}(t,t')]}e^{-|\chi_{\mathbf{k},\mu}(t')+\delta_\alpha(t,t',\omega_k,\mathbf{v}_\alpha)|^2/2}]$$

$$\bigotimes_{\mathbf{k},\mu\simeq\mathbf{k}_{L,\mu}}e^{i[\varphi_{\mathbf{k}\mu}(t,t',\mathbf{v}_\alpha)+\varphi_{\mathbf{k}\mu}^{\chi,\delta}(t,t')+\varphi_{\mathbf{k}\mu}^{\chi,\delta,\alpha}(t,t')]}\,\big|[\alpha_{\mathbf{k}_L} + \chi_{\mathbf{k},\mu}(t') + \delta_\alpha(t, t', \omega_k, \mathbf{v}_\alpha)]e^{-i\omega_{\mathbf{k}}t}\big\rangle, \tag{E10}$$

where $\Theta(\mathbf{k}_{\text{HH}})$ is a Heaviside function taking into account only the contributions with field momentum $\mathbf{k}_{\text{HH}} \gg \mathbf{k}_L$. Having in mind that the action of the electric field operator over a generic coherent state $|\beta_{\mathbf{k}}\rangle$ can be written as

$$\mathbf{E}_{Q,\mathbf{k}}(t, \mathbf{R}_\alpha)\,|\beta_{\mathbf{k}}\rangle = \mathbf{E}_{\beta\cdot\mathbf{k}}(t, \mathbf{R}_\alpha)\,|\beta_{\mathbf{k}}\rangle - i\tilde{g}(k)\epsilon_{\mathbf{k},\mu}D(\beta_{\mathbf{k}})\,|1_{\mathbf{k}}\rangle, \tag{E11}$$

we can then write

$$\mathbf{E}_{Q,\mathbf{k}_L}(t' - t, \mathbf{R}_\alpha)\,\big|[\alpha_{\mathbf{k}_L} + \chi_{\mathbf{k},\mu}(t') + \delta_\alpha(t, t', \omega_k, \mathbf{v}_\alpha)]e^{-i\omega_{\mathbf{k}}t}\big\rangle$$

$$= [\mathbf{E}_{\text{cl}}(t', \mathbf{R}_\alpha) + \mathbf{E}_\delta(t', \mathbf{R}_\alpha) + \mathbf{E}_\chi(t', \mathbf{R}_\alpha)]\,\big|[\alpha_{\mathbf{k}_L} + \xi_{\mathbf{k},\mu}(t') + \delta_\alpha(t, t', \omega_k, \mathbf{v}_\alpha)]e^{-i\omega_{\mathbf{k}}t}\big\rangle$$

$$- i\tilde{g}(\mathbf{k}_L)\epsilon_{\mathbf{k}_L,\mu}D([\alpha_{\mathbf{k}_L} + \chi_{\mathbf{k},\mu}(t') + \delta_\alpha(t, t', \omega_k, \mathbf{v}_\alpha)]e^{-i\omega_{\mathbf{k}}t})\,|1\rangle \tag{E12}$$

such that the conditioned to ATI state reads

$$|\Phi_{\text{ATI}}^{\mathbf{k}_L}(t, \mathbf{p})\rangle = \langle\{0\}_{\text{HH}}|\,|\Phi_{\text{ATI}}(t, \mathbf{p})\rangle$$

$$= \frac{-ie}{\hbar}\int_{t_0}^t dt'\left[\mathbf{E}_\chi(t', \mathbf{R}_\alpha) + \int d^3k\Theta(\mathbf{k}_{\text{HH}})\tilde{g}(k)\epsilon_{\mathbf{k},\mu}e^{-i\omega_k t'+i\mathbf{k}\cdot\mathbf{R}_\alpha}[\chi_{\mathbf{k},\mu}(t') + \delta_\alpha(t, t', \omega_k, \mathbf{v}_\alpha)]\right]$$

$$\times \langle\mathbf{v}_\alpha|\,\mathbf{r}_\alpha(t')\,|g\rangle\,\mathcal{C}_{\text{HH}}(p, t, t')\bigotimes_{\mathbf{k},\mu\simeq\mathbf{k}_{L,\mu}}e^{i\theta_{\mathbf{k},\mu}(t,t',\mathbf{p},\alpha)}\,\big|[\alpha_{\mathbf{k}_L} + \chi_{\mathbf{k},\mu}(t') + \delta_\alpha(t, t', \omega_k, \mathbf{v}_\alpha)]e^{-i\omega_{\mathbf{k}}t}\big\rangle$$

$$- \frac{e}{\hbar}\int d^3k\Pi(\mathbf{k}_L)\tilde{g}(k)\int_{t_0}^t dt'\epsilon_{\mathbf{k}_L,\mu}\cdot\langle\mathbf{v}_\alpha|\,\mathbf{r}_\alpha(t')\,|g\rangle\,\mathcal{C}_{\text{HH}}(p, t, t')$$

$$\times \prod_{\mathbf{k},\mu\simeq\mathbf{k}_{L,\mu}}D([\alpha_{\mathbf{k}} + \chi_{\mathbf{k},\mu}(t') + \delta_\alpha(t, t', \omega_k, \mathbf{v}_\alpha)]e^{-i\omega_{\mathbf{k}}t})\bigotimes_{\mathbf{k}',\mu\simeq\mathbf{k}_{L,\mu}}e^{i\theta_{\mathbf{k}',\mu}(t,t',\mathbf{p},\alpha)}\,\big|1_{\mathbf{k}}, \{0\}_{\mathbf{k}'\neq\mathbf{k}}\big\rangle, \tag{E13}$$

where $\Theta(\mathbf{k}_{\text{HH}})$ is a Heaviside function that takes into account contributions for which $\mathbf{k}_{\text{HH}} \gg \mathbf{k}_L$, and $\Pi(\mathbf{k}_L)$ is a rectangular function that is one whenever $\mathbf{k} \simeq \mathbf{k}_L$ and zero otherwise. We have further defined

$$\theta_{\mathbf{k},\mu}(t, t', \mathbf{p}, \alpha) = \phi_{\mathbf{k},\mu}(t, t', \mathbf{v}_\alpha) + \text{Im}[\delta_\alpha(t, t', \omega_k, \mathbf{v}_\alpha)\chi_{\mathbf{k},\mu}^*(t')]$$

$$+ \text{Im}\{\alpha_{\mathbf{k}_L}[\delta_\alpha^*(t, t', \omega_k, \mathbf{v}_\alpha) + \chi_{\mathbf{k},\mu}^*(t')]\}, \tag{E14}$$

which is the Baker-Campbell-Hausdorff (BCH) phase that appears together with other phases arising from applying the

commutation relation between two displacement operators. We have also defined

$$C_{\mathrm{HH}}(p,t,t') = \prod_{\mathbf{k},\mu \gg \mathbf{k}_{L,\mu}} [e^{i\{\varphi_{\mathbf{k}\mu}(t,t',\mathbf{v}_\alpha)+\mathrm{Im}[\delta_\alpha(t,t',\omega_k,\mathbf{v}_\alpha)\chi^*_{\mathbf{k},\mu}(t')]\}} e^{-|\chi_{\mathbf{k},\mu}(t')+\delta_\alpha(t,t',\omega_k,\mathbf{v}_\alpha)|^2/2}], \tag{E15}$$

which is a weight function that arises as a consequence of the conditioning onto the vacuum state of the harmonics modes. Finally, we have defined

$$\mathbf{E}_\chi(t',\mathbf{R}_\alpha) = i\sum_\mu \int d^3k \tilde{g}(k)\epsilon_{k\mu}[\chi_{\mathbf{k},\mu}(t')e^{-i\omega_k t+i\mathbf{k}\cdot\mathbf{R}_\alpha} - \chi^*_{\mathbf{k},\mu}(t')e^{i\omega_k t-i\mathbf{k}\mathbf{R}_\alpha}]. \tag{E16}$$

Finally, we project the previous expression with respect to the Fock state basis $|n\rangle$ to get the photon-number probability amplitude for the direct term. Note that in order to get expressions that can be analyzed computationally we consider a single fundamental mode, corresponding to the central frequency of the employed electric field

$$|\Phi^{\mathbf{k}_L}_{\mathrm{ATI}}(t,\mathbf{p})\rangle = \langle\{0\}_{\mathrm{HH}}| |\Phi_{\mathrm{ATI}}(t,\mathbf{p})\rangle$$

$$= \frac{-ie}{\hbar}\int_{t_0}^t dt' \left[\mathbf{E}_\chi(t',\mathbf{R}_\alpha) + \int d^3k\,\Theta(\mathbf{k}_{\mathrm{HH}})\tilde{g}(k)\epsilon_{\mathbf{k},\mu}e^{-i\omega_k t'+i\mathbf{k}\cdot\mathbf{R}_\alpha}[\chi_{\mathbf{k},\mu}(t')+\delta_\alpha(t,t',\omega_k,\mathbf{v}_\alpha)]\right]$$

$$\times \langle\mathbf{v}_\alpha|\,\mathbf{r}_\alpha(t')\,|g\rangle\, C_{\mathrm{HH}}(p,t,t')e^{i\theta_{\mathbf{k},\mu}(t,t',\mathbf{p},\alpha)}e^{-|\alpha_{\mathbf{k}_L}+\chi_{\mathbf{k},\mu}(t')+\delta_\alpha(t,t',\omega_k,\mathbf{v}_\alpha)|^2/2}\frac{([\alpha_{\mathbf{k}_L}+\chi_{\mathbf{k},\mu}(t')+\delta_\alpha(t,t',\omega_k,\mathbf{v}_\alpha)]e^{-i\omega_k t})^n}{\sqrt{n!}}$$

$$- \frac{e}{\hbar}\int d^3k\,\Pi(\mathbf{k}_L)\tilde{g}(\mathbf{k})\int_{t_0}^t dt'\epsilon_{\mathbf{k}_L,\mu}\cdot\langle\mathbf{v}_\alpha|\,\mathbf{r}_\alpha(t')\,|g\rangle\, C_{\mathrm{HH}}(p,t,t')e^{i\theta_{\mathbf{k'},\mu}(t,t',\mathbf{p},\alpha)}e^{-|\alpha_{\mathbf{k}_L}+\chi_{\mathbf{k},\mu}(t')+\delta_\alpha(t,t',\omega_k,\mathbf{v}_\alpha)|^2/2}$$

$$\times \left[\sqrt{n}\frac{([\alpha_{\mathbf{k}_L}+\chi_{\mathbf{k},\mu}(t')+\delta_\alpha(t,t',\omega_k,\mathbf{v}_\alpha)]e^{-i\omega_k t})^{n-1}}{\sqrt{n-1!}} - \frac{([\alpha_{\mathbf{k}_L}+\chi_{\mathbf{k},\mu}(t')+\delta_\alpha(t,t',\omega_k,\mathbf{v}_\alpha)]e^{-i\omega_k t})^n}{\sqrt{n!}}\right], \tag{E17}$$

such that, up to a normalization factor, the photon-number probability distribution for the $\mathbf{k}_{L,\mu}$ mode is given by

$$P_{n_{\mathbf{k}_L}}(t,\mathbf{p}) = |\langle n|\Phi^{\mathbf{k}_L}_{\mathrm{ATI}}(t,\mathbf{p})\rangle|^2. \tag{E18}$$

APPENDIX F: PERTURBATION THEORY FOR RESCATTERING IN ATI

From the perturbation theory analysis considered in the main part of the manuscript, Eq. (79), for the introduction of the rescattering part of the state, we get the following set of equations for each of the perturbation orders:

$$i\hbar\frac{d}{dt}|\phi^{(0)}(\mathbf{v},t)\rangle = e\mathbf{E}_Q(t,\mathbf{R})\cdot\langle\mathbf{v}|\,\mathbf{r}(t)\,|g\rangle\,|\phi(t)\rangle + e\mathbf{E}_Q(t,\mathbf{R})\cdot\Delta\mathbf{r}(t,\mathbf{v}_\alpha)|\phi^{(0)}(\mathbf{v},t)\rangle, \tag{F1a}$$

$$i\hbar\frac{d}{dt}|\phi^{(1)}(\mathbf{v},t)\rangle = e\mathbf{E}_Q(t,\mathbf{R})\Delta\mathbf{r}(t,\mathbf{v})|\phi^{(1)}(\mathbf{v},t)\rangle - \frac{\hbar}{e}\int d^3v'\exp\left[\frac{i}{\hbar}S(\mathbf{v}',t,t_0)\right]\mathbf{E}_Q(t,\mathbf{R})\mathbf{g}(\mathbf{v},\mathbf{v}')$$

$$\times \exp\left[-\frac{i}{\hbar}S(\mathbf{v}',t',t_0)\right]|\phi^{(0)}(\mathbf{v}',t)\rangle. \tag{F1b}$$

Here, we define $\Delta\mathbf{r}(t,\mathbf{v})$ as in Eq. (62), so that the first equation describes the dynamics of the zeroth-order perturbation term that characterizes direct ionization phenomena, and that has been previously discussed. On the other hand, the second term describes the rescattering dynamics, i.e., electrons that, once ionized, can then rescatter at the potential of the parent ion. Similarly to what we had in the direct ionization term, the solution to this differential equation is given as the superposition of a homogeneous term similar to that in Eq. (63), plus an inhomogeneous term of the form

$$|\phi^{(1)}(\mathbf{v},t)\rangle = -i\int_{t_0}^t dt_2\int d^3v'\prod_{\mathbf{k},\mu}e^{i\varphi_{\mathbf{k}\mu}(t,t_2,\mathbf{v})}D(\delta(t,t_2,\omega_k,\mathbf{v}))\exp\left[\frac{i}{\hbar}S(\mathbf{v},t,t_0)\right]$$

$$\times \mathbf{E}_Q(t_2,\mathbf{R})\cdot\mathbf{g}(\mathbf{v},\mathbf{v}')\exp\left[-\frac{i}{\hbar}S(t_2,t_0,\mathbf{v}')\right]|\phi^{(0)}(\mathbf{v}',t_2)\rangle. \tag{F2}$$

However, since the electron is initially in the ground state, $\left|\phi^{(1)}(\mathbf{v}, t_0)\right\rangle = 0$, which implies that the homogeneous solution does not participate in the final solution. Then, the rescattering part of the state is entirely described by Eq. (F2).

APPENDIX G: DESCRIPTION OF THE NUMERICAL IMPLEMENTATION

In the following we describe the numerical procedure used to obtain the field observables in the main part of the manuscript (see Sec. IV C 2). The analysis is implemented in PYTHON, and the codes are available from Zenodo [182]. Our numerical implementation consists of the following steps.

1. Once the vector potential $\mathbf{A}(t)$ of the pulse under consideration is defined, we compute the expectation value of the time-dependent dipole moment $\langle \mathbf{d}(t) \rangle$ under the SFA framework.
2. Given a time interval $[t_0, T]$, where t_0 and T correspond to the beginning and end of the pulse, respectively, we compute $\chi(t)$ and $C_{\mathrm{HH}}(p, T, t)$ given by Eq. (E15). We use a step size of $\Delta t = 1.0$. For the displacement via $\delta(t, t_0, \omega_k, p)$, we compute the analytic exact expression for a $\sin^2$ envelope pulse.
3. Finally, we use an interpolating scheme such that we can have a numerical function for $\chi(t)$ and $C_{\mathrm{HH}}(p, T, t)$, which can adapt to the time integrals that need to be done for computing the photon-number probability distribution.

Furthermore, along this section we work with atomic units (a.u.), such that $\hbar = 1, e^2 = 1, m = 1$, and $\epsilon_0 = 4\pi$.

1. SFA expressions for the time-dependent dipole

The expectation value of the time-dependent dipole moment is defined as

$$\langle \mathbf{d}(t) \rangle = \langle \psi(t)| \, \mathbf{d} \, |\psi(t)\rangle, \qquad (G1)$$

where $|\psi(t)\rangle$ is the wave function of a single electron in the intense laser field. To obtain the wave function, we introduce the SFA approximations [117], namely (i) the contribution of all bound states except the ground state are neglected; (ii) the depletion of the ground state can be neglected; and (iii) in the continuum, the electron can be treated as a free particle, that is, we can neglect the interaction with the binding potential. Thus, we can write the semiclassical quantum state describing the electron as

$$|\psi(t)\rangle = e^{iI_p t} |g\rangle + \int d^3 p \, b(\mathbf{p}, t) \, |\mathbf{p} + \mathbf{A}(t)\rangle, \qquad (G2)$$

where the probability amplitude of finding the electron in the continuum state $|\mathbf{p} + \mathbf{A}(t)\rangle$ is given by

$$b(\mathbf{p}, t) = i \int_{t_0}^{t} dt' \mathbf{E}(t') \cdot \mathbf{d}(\mathbf{p} + \mathbf{A}(t'))$$
$$\times \exp\left\{ -i \int_{t'}^{t} d\tau [(\mathbf{p} + \mathbf{A}(\tau))^2 + I_p] \right\}, \quad (G3)$$

where $\mathbf{d}(\mathbf{p} + \mathbf{A}(t)) = \langle \mathbf{p} + \mathbf{A}(t)| \, \mathbf{d} \, |g\rangle$ is the transition dipole moment between the ground and continuum states. Substituting these expressions into Eq. (G1), and neglecting the contributions from the continuum-continuum transitions, we get the SFA expression for the dipole moment expectation value

$$\langle \mathbf{d}(t) \rangle = i \int d^3 p \int_{t_0}^{t} dt' \mathbf{d}^*(\mathbf{p} + \mathbf{A}(t)) \mathbf{E}(t') \cdot \mathbf{d}(\mathbf{p} + \mathbf{A}(t'))$$
$$\times \exp\left\{ -i \int_{t'}^{t} d\tau [(\mathbf{p} + \mathbf{A}(\tau))^2 + I_p] \right\} + \text{c.c.}$$
$$(G4)$$

For the numerical analysis, we considered a linearly polarized field with vector potential given by

$$\mathbf{A}(t) = \epsilon_z \frac{E_0}{\omega} \sin[2]\left(\frac{\omega}{2n_{\mathrm{cyc}}}\right) \sin(\omega t), \qquad (G5)$$

where n_{cyc} is the total number of cycles of the pulse with a $\sin^2$ envelope and ϵ_z is a unitary vector along the z axis describing the polarization of the state. In all numerical analyses, we use $\omega = 0.057$ a.u. and $E_0 = 0.053$ a.u. On the other hand, we consider the ground-state wave function of the electron to be described by

$$\langle x|g \rangle = \sqrt{\frac{\lambda^3}{\pi}} e^{-\lambda r}, \qquad (G6)$$

such that the dipole transition matrix element connecting the continuum state with the ground state is given by

$$\mathbf{d}(\mathbf{p} + \mathbf{A}(t)) = \langle \mathbf{p} + \mathbf{A}(t)| \, \mathbf{d} \, |g\rangle$$
$$= -i\sqrt{\frac{\lambda^3}{\pi}} \frac{\mathbf{p} + \mathbf{A}(t)}{(2\pi)^{3/2}} \frac{32\pi\lambda}{(\lambda^2 + (p + A(t))^2)^3}. \qquad (G7)$$

More particularly, for a 1s state of a hydrogen atom, we set $I_p = 0.5$ a.u. and $\lambda = 1$. In Fig. 18(a) we show the dipole moment expectation value (G4) obtained, and in Fig. 18(b) we show the corresponding vector potential with $n_{\mathrm{cyc}} = 5$. In order to perform the two integrals, we first discretize that for the momentum (which we perform in one dimension) and use the `quad` function from the SciPy package [183].
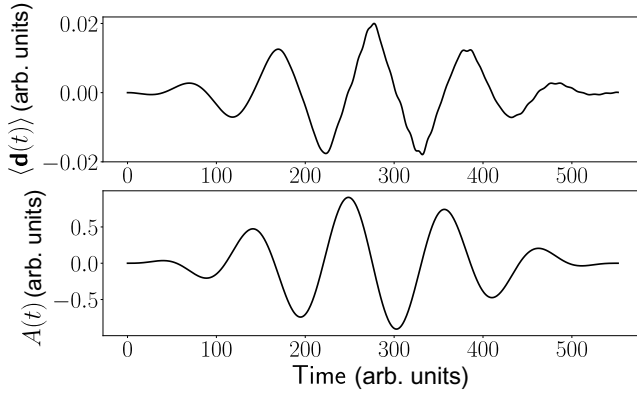
FIG. 18. (a) Dipole moment expectation value obtained from the numerical calculations under the SFA approach. (b) Vector potential used to obtain the dipole moment shown in (a). The pulse shown has $n_{\mathrm{cyc}} = 5$ cycles.

FIG. 19. Behaviors of (a) $\chi_{\mathbf{k}_L}(t)$ and (b) $C_{\mathrm{HH}}(p = 2U_p, T, t)$ with a time interval of $\Delta t = 1.0$ (solid black curve), and the function obtained from the interpolation (dashed orange curve). For the interpolation plot, we considered a time step $\Delta t = 0.01$.

2. Calculation and interpolation of the quantum optical displacements

With the dipole moment obtained in the previous subsection within the SFA approach, we can now compute the photonic displacement given by $\xi(t)$, which is defined as

$$\chi(t) \propto \int_{t_0}^{t} dt' e^{i\omega t'} \langle \mathbf{d}(t') \rangle. \tag{G8}$$

We further compute

$$C_{\mathrm{HH}}(p, T, t') = \prod_{\mathbf{k},\mu \gg \mathbf{k}_{L,\mu}} [e^{i\{\varphi_{\mathbf{k}\mu}(T,t',\mathbf{v}_\alpha) + \mathrm{Im}[\delta_\alpha(T,t',\omega_k,\mathbf{v}_\alpha)\chi_{\mathbf{k},\mu}^*(t')]\}}$$

$$\times e^{-|\chi_{\mathbf{k},\mu}(t') + \delta_\alpha(T,t',\omega_k,\mathbf{v}_\alpha)|^2/2}], \tag{G9}$$

where $\delta(p, T, t', \omega_k)$ is obtained analytically. In particular, the computation of $C_{\mathrm{HH}}(p, T, t')$ involves the calculation of the BCH phase $\varphi_{\mathbf{k}\mu}(T, t', \mathbf{v}_\alpha)$ from Eq. (E5). For this, we consider a discrete set of harmonic modes consisting of the second up to the 21st harmonic, and perform an interpolation for each of the BCH phase factors. In principle, we could consider more harmonic orders, but their amplitudes $|\delta(t, t', \omega_k, \mathbf{v})|$ rapidly decrease for increasing harmonic orders, and therefore their contributions are negligible. Since the effect of $\chi_{\mathbf{k},\mu}$ can be neglected in comparison to that introduced by $\delta(t, t', \omega_k, \mathbf{v})$, we neglect their effect in the previous conditioning operation. Finally, once $C_{\mathrm{HH}}(p, T, t')$ has been obtained for each value of the ionization time t', we proceed to use an interpolation scheme to compute the photon-number probability distribution.

In both cases, similarly to what we did before, we perform this integral with the `quad` function, followed by performing an interpolation using the `interp1d` function provided by `SciPy`. The reason behind this is that, after the interpolation, we get two functions that exactly
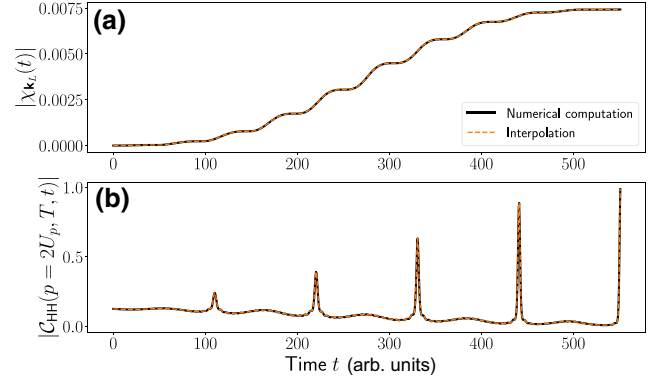
behave as $\chi(t)$ and $C_{\mathrm{HH}}(p, T, t')$ within the $[t_0, T]$ interval. Thus, by doing this we avoid the nested integrals that appear within the definition of the photon-number probability distribution. This provides a huge numerical speed up. In particular, for doing the interpolation, we use the `cubic` option that considers polynomials of zeroth to third order, and that better fits the oscillating behavior of both functions. The results of the interpolation are shown with the dashed orange curves in Fig. 19.

For computing the dipole moment expectation value, we set the time step $\Delta t = 1.0$. In Fig. 19, we show the behaviors of $\chi(t)$ and $\delta(p, T, t)$ (with $p = 0.1U_p$) defined by the integral (solid black line) and after the interpolation (dashed orange line). For the interpolation plot, we considered a time step $\Delta t = 0.01$.

3. Further considerations

As written in the main part of the manuscript, the photon-number probability distribution is computed in the original reference frame, i.e., after undoing the displacement operation $D(\alpha)$. The usual regime of intense laser field physics has coherent state amplitudes of the driving laser of the order of $|\alpha| \sim 10^6$. Such high photon numbers can only barely be implemented in the numerical analysis due to the numerical accuracy. Thus, in order to avoid this problem, we artificially reduce the value of α and multiply $g(k)$ by an extra factor $\lambda < 1$ to account for this reduction in the computed values of $\delta(p, t, t')$ and $\xi(t)$.

On the other hand, the specific value of α that we used in our numerical analysis is $\alpha = 7i$. This value is obtained from the definition of the vector potential, which is proportional to

$$\hat{A}(t) \propto f(t)[\hat{a}^\dagger e^{i\omega t} + \hat{a} e^{-i\omega t}]. \tag{G10}$$

Note that in the last expression we introduced the envelope function via $f(t)$, which appears as a consequence of

the multimode nature of our quantum optical description. If we now compute the average value of the vector potential operator with respect to the selected coherent state, we obtain

$$\langle A(t) \rangle = \langle 7i| \, \hat{A}(t) \, |7i \rangle \propto 14f(t) \sin(\omega t), \qquad \text{(G11)}$$

which has the same form as the vector potential we used in the previous part of our numerical analysis. Note that one can similarly get the same phase by looking at the real and imaginary parts of $\alpha_{\mathbf{k},\mu}$ in Fig. 3 of the main text.

---

[1] A. Siegman *Lasers* (University Science Books, California, 1986).

[2] R. J. Glauber, Coherent and incoherent states of the radiation field, Phys. Rev. **131**, 2766 (1963).

[3] R. J. Glauber, The quantum theory of optical coherence, Phys. Rev. **130**, 2529 (1963).

[4] E. Sudarshan, Equivalence of Semiclassical and Quantum Mechanical Descriptions of Statistical Light Beams, Phys. Rev. Lett. **10**, 277 (1963).

[5] J. H. Eberly and L. Allen, *Optical Resonance and Two Level Atoms* (Dover Publication, USA, 1987).

[6] S. Piszczatowski, G. Łach, M. Przybytek, J. Komasa, K. Pachucki, and B. Jeziorski, Theoretical determination of the dissociation energy of molecular hydrogen, J. Chem. Theory Comput. **5**, 3039 (2009).

[7] K. Pachucki, D. Leibfried, M. Weitz, A. Huber, W. König, and T. Hänsch, Theory of the energy levels and precise two-photon spectroscopy of atomic hydrogen and deuterium, J. Phys. B: At., Mol. Opt. Phys. **29**, 177 (1996).

[8] G. Drake, Accuracy in atomic and molecular data, J. Phys. B: At., Mol. Opt. Phys. **53**, 223001 (2020).

[9] J. Larson and T. Mavrogordatos, *Jaynes-Cummings Model and Its Descendants: Modern Research Directions*, IOP Series in Quantum Technology (IOP Publishing Ltd, Bristol, 2022).

[10] G. W. Drake, *Springer Handbook of Atomic, Molecular, and Optical Physics* (Springer Handbooks, Würzburg, 2022).

[11] A. S. Maxwell, L. B. Madsen, and M. Lewenstein, Entanglement of orbital angular momentum in non-sequential double ionization, Nat. Commun. **13**, 1 (2022).

[12] K. Amini, J. Biegert, F. Calegari, A. Chacón, M. F. Ciappina, A. Dauphin, D. K. Efimov, C. F. de Morisson Faria, K. Giergiel, and P. Gniewek, *et al.*, Symphony on strong field approximation, Rep. Prog. Phys. **82**, 116001 (2019).

[13] P. Agostini, F. Fabre, G. Mainfray, G. Petite, and N. K. Rahman, Free-Free Transitions Following Six-Photon Ionization of Xenon Atoms, Phys. Rev. Lett. **42**, 1127 (1979).

[14] P. Kruit, J. Kimman, H. G. Muller, and M. J. van der Wiel, Electron spectra from multiphoton ionization of xenon at 1064, 532, and 355 nm, Phys. Rev. A **28**, 248 (1983).

[15] W. Becker, F. Grasbon, R. Kopold, D. B. Milošević, G. G. Paulus, and H. Walther, Above-threshold ionization: from classical features to quantum effects, Adv. At. Mol. Opt. Phys. **48**, 35 (2002).

[16] A. McPherson, G. Gibson, H. Jara, U. Johann, T. S. Luk, I. A. McIntyre, K. Boyer, and C. K. Rhodes, Studies of multiphoton production of vacuum-ultraviolet radiation in the rare gases, J. Opt. Soc. Am. B **4**, 595 (1987).

[17] M. Ferray, A. L'Huillier, X. Li, L. Lompre, G. Mainfray, and M. C, Multiple-harmonic conversion of 1064 nm radiation in rare gases, J. Phys. B: At., Mol. Opt. Phys. **21**, L31 (1988).

[18] M. Lewenstein and A. L'Huillier, *Strong Field Laser Physics*, edited by T. Brabec, Chap. Principles of Single Atom Physics: High-Order Harmonic Generation, Above-Threshold Ionization and Non-Sequential Ionization (Springer, New York, 2009), p. 147.

[19] A. l'Huillier, L. A. Lompre, G. Mainfray, and C. Manus, Multiply charged ions induced by multiphoton absorption in rare gases at 0.53 μm, Phys. Rev. A **27**, 2503 (1983).

[20] P. B. Corkum, Plasma Perspective on Strong Field Multiphoton Ionization, Phys. Rev. Lett. **71**, 1994 (1993).

[21] B. Walker, B. Sheehy, L. F. DiMauro, P. Agostini, K. J. Schafer, and K. C. Kulander, Precision Measurement of Strong Field Double Ionization of Helium, Phys. Rev. Lett. **73**, 1227 (1994).

[22] B. Feuerstein, R. Moshammer, D. Fischer, A. Dorn, C. D. Schröter, J. Deipenwisch, J. R. Crespo Lopez-Urrutia, C. Höhr, P. Neumayer, J. Ullrich, H. Rottke, C. Trump, M. Wittmann, G. Korn, and W. Sandner, Separation of Recollision Mechanisms in Nonsequential Strong Field Double Ionization of Ar: The Role of Excitation Tunneling, Phys. Rev. Lett. **87**, 043003 (2001).

[23] W. Becker, X. Liu, P. Ho, and J. Eberly, Theories of photoelectron correlation in laser-driven multiple atomic ionization, Rev. Mod. Phys. **84**, 1011 (2012).

[24] A. Bandrauk and H. Kono, *Advances in Multi-Photon Processes and Spectroscopy: Molecules in Intense Laser Fields*. Nonlinear Multiphoton Spectrocopy and Near-femtosecond to Sub-Femtosecond (Attosecond) Dynamics (15, p. World Scientific, Singapore, 2006), Vol. 149.

[25] F. Calegari, G. Sansone, S. Stagira, C. Vozzi, and M. Nisoli, Advances in attosecond science, J. Phys. B: At., Mol. Opt. Phys. **49**, 062001 (2016).

[26] M. Nisoli, P. Decleva, F. Calegari, A. Palacios, and F. Martín, Attosecond electron dynamics in molecules, Chem. Rev. **117**, 10760 (2017).

[27] Y. Liu, Ed., *Advances of Atoms and Molecules in Strong Laser Fields* (World Scientific, Singapore, 2015).

[28] M. Lezius, S. Dobosz, D. Normand, and M. Schmidt, Explosion Dynamics of Rare Gas Clusters in Strong Laser Fields, Phys. Rev. Lett. **80**, 261 (1998).

[29] C. Jungreuthmayer, M. Geissler, J. Zanghellini, and T. Brabec, Microscopic Analysis of Large-Cluster Explosion in Intense Laser Fields, Phys. Rev. Lett. **92**, 133401 (2004).

[30] C. Siedschlag, U. Saalmann, and J. Rost, *Latest Advances in Atomic Cluster Collisions: Clusters in Intense Laser Fields* (World Scientific, 2004), Vol. 15, p. 271.

[31] G. Vampa and T. Brabec, Merge of high harmonic generation from gases and solids and its implications for attosecond science, J. Phys. B **50**, 083001 (2017).

[32] A. Jiménez-Galán, R. E. F. Silva, O. Smirnova, and M. Ivanov, Lightwave control of topological properties in 2D

materials for sub-cycle and non-resonant valley manipulation, Nat. Photonics **14**, 728 (2020).

[33] A. Chacón, D. Kim, W. Zhu, S. Kelly, A. Dauphin, E. Pisanty, A. Maxwell, A. Picón, M. Ciappina, D. Kim, C. Ticknor, A. Saxena, and M. Lewenstein, Circular dichroism in higher-order harmonic generation: Heralding topological phases and transitions in Chern insulators, Phys. Rev. B **102**, 134115 (2020).

[34] Classical random fluctuation of the laser fields, such as the phase or amplitude fluctuations, were obviously already considered both in multiphoton physics and in SILAP [10, 184,185].

[35] A. N. Artemyev, L. S. Cederbaum, and P. V. Demekhin, Impact of intense laser pulses on the autoionization dynamics of the $2s2p$ doubly excited state of He, Phys. Rev. A **96**, 033410 (2017).

[36] A. N. Artemyev, L. S. Cederbaum, and P. V. Demekhin, Impact of two-electron dynamics and correlations on high-order-harmonic generation in He, Phys. Rev. A **95**, 033402 (2017).

[37] E. Runge and E. K. U. Gross, Density-Functional Theory for Time-Dependent Systems, Phys. Rev. Lett. **52**, 997 (1984).

[38] A. Castro, A. Rubio, and E. K. U. Gross, Enhancing and controlling single-atom high-harmonic generation spectra: A time-dependent density-functional scheme, Eur. Phys. J. B **88**, 191 (2015).

[39] A. P. Woźniak, M. Lesiuk, M. Przybytek, D. K. Efimov, J. S. Prauzner-Bechcicki, M. Mandrysz, M. Ciappina, E. Pisanty, J. Zakrzewski, M. Lewenstein, and R. Moszyński, A systematic construction of Gaussian basis sets for the description of laser field ionization and high-harmonic generation, J. Chem. Phys. **154**, 094111 (2021).

[40] A. P. Woźniak, M. Przybytek, M. Lewenstein, and R. Moszyński, Effects of electronic correlation on the high harmonic generation in helium: A time-dependent configuration interaction singles vs time-dependent full configuration interaction study, ArXiv:2201.09339 (2022).

[41] C. J. Joachain, N. J. Kylstra, and R. Potvliege, *Atoms in Intense Laser Fields* (Cambridge University Press, Cambridge, Cambridge, 2012).

[42] J. G. Leopold and I. C. Percival, Microwave Ionization and Excitation of Rydberg Atoms, Phys. Rev. Lett. **41**, 944 (1978).

[43] I. C. Percival, in *Advances in Chemical Physics* (John Wiley & Sons, Ltd, 1977), p. 1.

[44] J. Grochmalicki, M. Lewenstein, and K. Rzążewski, Stabilization of Atoms in Superintense Laser Fields: Is It Real?, Phys. Rev. Lett. **66**, 1038 (1991).

[45] G. Vampa, C. R. McDonald, G. Orlando, D. D. Klug, P. B. Corkum, and T. Brabec, Theoretical Analysis of High-Harmonic Generation in Solids, Phys. Rev. Lett. **113**, 073901 (2014).

[46] E. N. Osika, A. Chacón, L. Ortmann, N. Suárez, J. A. Pérez-Hernández, B. Szafran, M. F. Ciappina, F. Sols, A. S. Landsman, and M. Lewenstein, Wannier-Bloch Approach to Localization in High-Harmonics Generation in Solids, Phys. Rev. X **7**, 021017 (2017).

[47] D. Bauer and K. K. Hansen, High-Harmonic Generation in Solids with and without Topological Edge States, Phys. Rev. Lett. **120**, 177401 (2018).

[48] C. Jürß and D. Bauer, High-harmonic generation in Su-Schrieffer-Heeger chains, Phys. Rev. B **99**, 195428 (2019).

[49] N. Baldelli, U. Bhattacharya, D. González-Cuadra, M. Lewenstein, and T. Graß, Detecting Majorana zero modes via strong field dynamics, ArXiv:2202.03547 (2022).

[50] J. Alcalà, U. Bhattacharya, J. Biegert, M. Ciappina, U. Elu, T. Graß, P. T. Grochowski, M. Lewenstein, A. Palau, T. P. H. Sidiropoulos, T. Steinle, and I. Tyulnev, High-harmonic spectroscopy of quantum phase transitions in a high-T_c superconductor, PNAS **119**, e2207766119 (2022).

[51] A. Georges, G. Kotliar, W. Krauth, and M. J. Rozenberg, Dynamical mean-field theory of strongly correlated fermion systems and the limit of infinite dimensions, Rev. Mod. Phys. **68**, 13 (1996).

[52] G. Kotliar, S. Y. Savrasov, K. Haule, V. S. Oudovenko, O. Parcollet, and C. A. Marianetti, Electronic structure calculations with dynamical mean-field theory, Rev. Mod. Phys. **78**, 865 (2006).

[53] D. Vollhardt, Dynamical mean-field theory of electronic correlations in models and materials, AIP Conf. Proc. **1297**, 339 (2010).

[54] P. A. Lee, From high temperature superconductivity to quantum spin liquid: Progress in strong correlation physics, Rep. Prog. Phys. **71**, 012501 (2007).

[55] J. H. Eberly and J. Javanainen, Above-threshold ionisation, Eur. J. Phys. **9**, 265 (1988).

[56] J. H. Eberly, J. Javanainen, and K. Rzążewski, Above-threshold ionization, Phys. Rep. **204**, 331 (1991).

[57] N. Suárez, A. Chacón, M. F. Ciappina, J. Biegert, and M. Lewenstein, Above-threshold ionization and photoelectron spectra in atomic systems driven by strong laser fields, Phys. Rev. A **92**, 063421 (2015).

[58] N. Suárez, A. Chacón, M. F. Ciappina, B. Wolter, J. Biegert, and M. Lewenstein, Above-threshold ionization and laser-induced electron diffraction in diatomic molecules, Phys. Rev. A **94**, 043423 (2016).

[59] N. Suárez, A. Chacón, J. A. Pérez-Hernández, J. Biegert, M. Lewenstein, and M. F. Ciappina, High-order-harmonic generation in atomic and molecular systems, Phys. Rev. A **95**, 033415 (2017).

[60] N. Suárez, A. Chacón, E. Pisanty, L. Ortmann, A. S. Landsman, A. Picón, J. Biegert, M. Lewenstein, and M. F. Ciappina, Above-threshold ionization in multicenter molecules: The role of the initial state, Phys. Rev. A **97**, 033415 (2018).

[61] N. Suárez Rojas, Strong-field processes in atoms and polyatomic molecules, TDX (Tesis Doctorals en Xarxa) (2018).

[62] M. Schuricke, G. Zhu, J. Steinmann, K. Simeonidis, I. Ivanov, A. Kheifets, A. N. Grum-Grzhimailo, K. Bartschat, A. Dorn, and J. Ullrich, Strong-field ionization of lithium, Phys. Rev. A **83**, 023413 (2011).

[63] K. T. Taylor, J. S. Parker, K. J. Meharg, and D. Dundas, Laser-driven helium at 780 nm, Eur. Phys. J. D: At., Mol. Opt. Plasma Phys. **26**, 67 (2003).

[64] J. S. Parker, L. R. Moore, D. Dundas, and K. T. Taylor, Double ionization of helium at 390 nm, J. Phys. B: At., Mol. Opt. Phys. **33**, L691 (2000).

[65] L. Moore, J. Parker, D. Dundas, K. Cairns, and K. Taylor, in *NATO Advanced Research Workshop on Super-Intense Laser-Atom Physics* (Springer, 2001), p. 107.

[66] H. G. Muller, Non-sequential double ionization of helium and related wave-function dynamics obtained from a five-dimensional grid calculation, Opt. Express **8**, 417 (2001).

[67] R. Grobe and J. H. Eberly, Photoelectron Spectra for a Two-Electron System in a Strong Laser Field, Phys. Rev. Lett. **68**, 2905 (1992).

[68] W.-C. Liu, J. H. Eberly, S. L. Haan, and R. Grobe, Correlation Effects in Two-Electron Model Atoms in Intense Laser Fields, Phys. Rev. Lett. **83**, 520 (1999).

[69] W. Becker, X. Liu, P. J. Ho, and J. H. Eberly, Theories of photoelectron correlation in laser-driven multiple atomic ionization, Rev. Mod. Phys. **84**, 1011 (2012).

[70] C. F. de Morisson Faria and X. Liu, Electron–electron correlation in strong laser fields, J. Mod. Opt. **58**, 1076 (2011).

[71] K. Sacha and B. Eckhardt, Pathways to double ionization of atoms in strong fields, Phys. Rev. A **63**, 043414 (2001).

[72] J. S. Prauzner-Bechcicki, K. Sacha, B. Eckhardt, and J. Zakrzewski, Time-Resolved Quantum Dynamics of Double Ionization in Strong Laser Fields, Phys. Rev. Lett. **98**, 203002 (2007).

[73] D. K. Efimov, A. Maksymov, M. Ciappina, J. S. Prauzner-Bechcicki, M. Lewenstein, and J. Zakrzewski, Three-electron correlations in strong laser field ionization, Opt. Express **29**, 26526 (2021).

[74] A. S. Maxwell and C. F. de Morisson Faria, Controlling Below-Threshold Nonsequential Double Ionization via Quantum Interference, Phys. Rev. Lett. **116**, 143001 (2016).

[75] D. S. Guo and T. Åberg, Quantum electrodynamical approach to multiphoton ionisation in the high-intensity H field, J. Phys. A: Math. General **21**, 4577 (1988).

[76] P. Fu, B. Wang, X. Li, and L. Gao, Interrelation between high-order harmonic generation and above-threshold ionization, Phys. Rev. A: At., Mol. Opt. Phys. **64**, 063401 (2001).

[77] B. Wang, L. Gao, X. Li, D. S. Guo, and P. Fu, Frequency-domain theory of high-order above-threshold ionization based on nonperturbative quantum electrodynamics, Phys. Rev. A: At., Mol. Opt. Phys. **75**, 063419 (2007).

[78] B. Wang, Y. Guo, J. Chen, Z.-C. Yan, and P. Fu, Frequency-domain theory of nonsequential double ionization in intense laser fields based on nonperturbative QED, Phys. Rev. A **85**, 023402 (2012).

[79] I. A. Gonoskov, N. Tsatrafyllis, I. K. Kominis, and P. Tzallas, Quantum optical signatures in strong-field laser physics: Infrared photon counting in high-order-harmonic generation, Sci. Rep. **6**, 32821 (2016).

[80] N. Tsatrafyllis, I. K. Kominis, I. A. Gonoskov, and P. Tzallas, High-order harmonics measured by the photon statistics of the infrared driving-field exiting the atomic medium, Nat. Commun. **8**, 15170 (2017).

[81] A. Gorlach, O. Neufeld, N. Rivera, O. Cohen, and I. Kaminer, The quantum-optical nature of high harmonic generation, Nat. Commun. **11**, 4598 (2020).

[82] N. Rivera and I. Kaminer, Light-matter interactions with photonic quasiparticles, Nat. Rev. Phys. **2**, 538 (2020).

[83] S. Fuchs, J. J. Abel, J. Nathanael, J. Reinhard, F. Wiesner, M. Wünsche, S. Skruszewicz, C. Rödel, D. Born, H. Schmidt, and G. G. Paulus, Photon counting of extreme ultraviolet high harmonics using a superconducting nanowire single-photon detector, Appl. Phys. B **128**, 26 (2022).

[84] K. Y. Spasibko, D. A. Kopylov, V. L. Krutyanskiy, T. V. Murzina, G. Leuchs, and M. V. Chekhova, Multiphoton Effects Enhanced Due to Ultrafast Photon-Number Fluctuations, Phys. Rev. Lett. **119**, 223603 (2017).

[85] M. Manceau, K. Y. Spasibko, G. Leuchs, R. Filip, and M. V. Chekhova, Indefinite-Mean Pareto Photon Distribution from Amplified Quantum Noise, Phys. Rev. Lett. **123**, 123606 (2019).

[86] A. Gorlach, M. E. Tzur, M. Birk, M. Krüger, N. Rivera, O. Cohen, and I. Kaminer, High harmonic generation driven by quantum light, Preprint ArXiv:2211.03188 (2022).

[87] S. Varró, Quantum optical aspects of high-harmonic generation, Photonics **8**, 269 (2021).

[88] P. Földi, I. Magashegyi, A. Gombkötő, and S. Varró, Describing high-order harmonic generation using quantum optical models, Photonics **8**, 263 (2021).

[89] A. Gombkötő, P. Földi, and S. Varró, Quantum-optical description of photon statistics and cross correlations in high-order harmonic generation, Phys. Rev. A **104**, 033703 (2021).

[90] M. Lewenstein, M. Ciappina, E. Pisanty, J. Rivera-Dean, P. Stammer, Th. Lamprou, and P. Tzallas, Generation of optical Schrödinger cat states in intense laser–matter interactions, Nat. Phys. **17**, 1104 (2021).

[91] P. Stammer, J. Rivera-Dean, Th. Lamprou, E. Pisanty, M. F. Ciappina, P. Tzallas, and M. Lewenstein, High Photon Number Entangled States and Coherent State Superposition from the Extreme Ultraviolet to the Far Infrared, Phys. Rev. Lett. **128**, 123603 (2022).

[92] J. Rivera-Dean, Th. Lamprou, E. Pisanty, P. Stammer, A. Ordóñez, A. Maxwell, M. Ciappina, M. Lewenstein, and P. Tzallas, Strong laser fields and their power to generate controllable high-photon-number coherent-state superpositions, Phys. Rev. A **105**, 033714 (2022).

[93] P. Stammer, Theory of entanglement and measurement in high-order harmonic generation, Phys. Rev. A **106**, L050402 (2022).

[94] T. Lamprou, R. Lopez-Martens, S. Haessler, I. Liontos, S. Kahaly, J. Rivera-Dean, P. Stammer, E. Pisanty, M. F. Ciappina, M. Lewenstein, and P. Tzallas, Quantum-optical spectrometry in relativistic laser–plasma interactions using the high-harmonic generation process: A proposal, Photonics **8**, 192 (2021).

[95] J. Rivera-Dean, P. Stammer, E. Pisanty, Th. Lamprou, P. Tzallas, M. Lewenstein, and M. F. Ciappina, New schemes for creating large optical Schrödinger cat states using strong laser fields, J. Comput. Electron. **20**, 2111 (2021).

[96] C. C. Tannoudji, G. Grynberg, and J. Dupont-Roe, *Atom-Photon Interactions* (New York, NY, USA, John Wiley and Sons Inc., 1992).

[97] C. Cohen-Tannoudji, J. Dupont-Roc, and G. Grynberg, *Photons and Atoms-Introduction to Quantum Electrodynamics* (Wiley-VCH, Weinheim, 1997).

[98] R. J. Glauber and M. Lewenstein, Quantum optics of dielectric media, Phys. Rev. A **43**, 467 (1991).

[99] W. Vogel and D.-G. Welsch, *Quantum Optics* (John Wiley & Sons, Weinheim, 2006).

[100] M. O. Scully and M. S. Zubairy, *Quantum Optics* (Cambridge University Press, Cambridge, 2001).

[101] S. Haroche and J.-M. Raimond, *Exploring the Quantum: Atoms, Cavities and Photons* (Oxford Graduate Texts, Oxford, 2006).

[102] R. L. Hudson, When is the Wigner quasi-probability density non-negative?, Rep. Math. Phys. **6**, 249 (1974).

[103] A. Kenfack and K. Życzkowski, Negativity of the Wigner function as an indicator of non-classicality, J. Opt. B: Quantum Semiclass. Opt. **6**, 396 (2004).

[104] J. K. Asbóth, P. Adam, M. Koniorczyk, and J. Janszky, Coherent-state qubits: Entanglement and decoherence, Eur. Phys. J. D: At., Mol. Opt. Plasma Phys. **30**, 403 (2004).

[105] B. C. Sanders, Entangled coherent states, Phys. Rev. A **45**, 6811 (1992).

[106] A. Gilchrist, K. Nemoto, W. J. Munro, T. C. Ralph, S. Glancy, S. L. Braunstein, and G. J. Milburn, Schrödinger cats and their power for quantum information processing, J. Opt. B: Quantum Semiclass. Opt. **6**, S828 (2004).

[107] P. Jouguet, S. Kunz-Jacques, A. Leverrier, P. Grangier, and E. Diamanti, Experimental demonstration of long-distance continuous-variable quantum key distribution, Nat. Photonics **7**, 378 (2013).

[108] S. Lloyd and S. L. Braunstein, Quantum Computation over Continuous Variables, Phys. Rev. Lett. **82**, 1784 (1999).

[109] T. C. Ralph, A. Gilchrist, G. J. Milburn, W. J. Munro, and S. Glancy, Quantum computation with optical coherent states, Phys. Rev. A **68**, 042319 (2003).

[110] J. Joo, W. J. Munro, and T. P. Spiller, Quantum Metrology with Entangled Coherent States, Phys. Rev. Lett. **107**, 083601 (2011).

[111] P. C. Aichelburg and H. Grosse, Exactly soluble system of relativistic two-body interaction, Phys. Rev. D **16**, 1900 (1977).

[112] P. C. Aichelburg, Model for Relativistic Two-Body Interaction with Radiation Reaction, Phys. Rev. Lett. **38**, 451 (1977).

[113] K. Rzążewski and W. Żakowicz, Initial value problem and causality of radiating oscillator, J. Phys. A: Math. General **9**, 1159 (1976).

[114] K. Rzążewski and W. Żakowicz, Initial value problem for two oscillators interacting with electromagnetic field, J. Math. Phys. **21**, 378 (1980).

[115] X.-M. Tong and S.-I. Chu, Density-functional theory with optimized effective potential and self-interaction correction for ground states and autoionizing resonances, Phys. Rev. A **55**, 3406 (1997).

[116] X. M. Tong and C. D. Lin, Empirical formula for static field ionization rates of atoms and molecules by lasers in the barrier-suppression regime, J. Phys. B: At., Mol. Opt. Phys. **38**, 2593 (2005).

[117] M. Lewenstein, P. Balcou, M. Y. Ivanov, A. L'Huillier, and P. B. Corkum, Theory of high-harmonic generation by low-frequency laser fields, Phys. Rev. A **49**, 2117 (1994).

[118] B. Sundaram and P. W. Milonni, High-order harmonic generation: Simplified model and relevance of single-atom theories to experiment, Phys. Rev. A **41**, 6571 (1990).

[119] D. Bauer and P. Koval, Qprop: A Schrödinger-solver for intense laser-atom interaction, Comput. Phys. Commun. **174**, 396 (2006).

[120] M. A. Nielsen and I. L. Chuang, *Quantum Computation and Quantum Information* (Cambridge University Press, Cambridge, 2000).

[121] J. L. Krause, K. J. Schafer, and K. C. Kulander, High-order Harmonic Generation from Atoms and Ions in the High Intensity Regime, Phys. Rev. Lett. **68**, 3535 (1992).

[122] S. J. van Enk and O. Hirota, Entangled coherent states: Teleportation and decoherence, Phys. Rev. A **64**, 022313 (2001).

[123] A. Othman and D. Yevick, Quantum properties of the superposition of two nearly identical coherent states, Int. J. Theor. Phys. **57**, 2293 (2018).

[124] L. B. Madsen, Strong-field approximation for high-order harmonic generation in infrared laser pulses in the accelerated Kramers-Henneberger frame, Phys. Rev. A **104**, 033117 (2021).

[125] G. G. Paulus, F. Lindner, H. Walther, A. Baltuška, E. Goulielmakis, M. Lezius, and F. Krausz, Measurement of the Phase of Few-Cycle Laser Pulses, Phys. Rev. Lett. **91**, 253004 (2003).

[126] D. B. Milošević, G. G. Paulus, D. Bauer, and W. Becker, Above-threshold ionization by few-cycle pulses, J. Phys. B: At., Mol. Opt. Phys. **39**, R203 (2006).

[127] A. I. Lvovsky and M. G. Raymer, Continuous-variable optical quantum-state tomography, Rev. Mod. Phys. **81**, 299 (2009).

[128] G. Breitenbach, S. Schiller, and J. Mlynek, Measurement of the quantum states of squeezed light, Nature **387**, 471 (1997).

[129] M. Skotiniotis, W. Dür, and P. Sekatski, Macroscopic superpositions require tremendous measurement devices, Quantum **1**, 34 (2017).

[130] S. Chatziathanasiou, S. Kahaly, E. Skantzakis, G. Sansone, R. Lopez-Martens, S. Haessler, K. Varju, G. D. Tsakiris, D. Charalambidis, and P. Tzallas, Generation of attosecond light pulses from gas and solid state media, Photonics **4**, 26 (2006).

[131] G. G. Paulus, F. Grasbon, H. Walther, P. Villoresi, M. Nisoli, S. Stagira, E. Priori, and S. D. Silvestri, Absolute-phase phenomena in photoionization with few-cycle laser pulses, Nature **414**, 182 (2001).

[132] N. Tsatrafyllis, S. Kühn, M. Dumergue, P. Foldi, S. Kahaly, E. Cormier, I. A. Gonoskov, B. Kiss, K. Varju, S. Varro, and P. Tzallas, Quantum Optical Signatures in a Strong Laser Pulse after Interaction with Semiconductors, Phys. Rev. Lett. **122**, 193602 (2019).

[133] I. J. Kim, C. M. Kim, H. T. Kim, G. H. Lee, Y. S. Lee, J. Y. Park, D. J. Cho, and C. H. Nam, Highly Efficient High-Harmonic Generation in an Orthogonally Polarized Two-Color Laser Field, Phys. Rev. Lett. **94**, 243901 (2005).

[134] J. Mauritsson, P. Johnsson, E. Gustafsson, A. L'Huillier, K. J. Schafer, and M. B. Gaarde, Attosecond Pulse Trains Generated Using Two Color Laser Fields, Phys. Rev. Lett. **97**, 013001 (2006).

[135] A. Fleischer, O. Kfir, T. Diskin, P. Sidorenko, and O. Cohen, Spin angular momentum and tunable polarization in highharmonic generation, Nat. Photonics **8**, 543 (2014).

[136] A. Gilchrist, K. Nemoto, W. J. Munro, T. C. Ralph, S. Glancy, S. L. Braunstein, and G. J. Milburn, Schrödinger cats and their power for quantum information processing, J. Opt B: Quantum Semiclass. **6**, 5828 (2004).

[137] A. Laghaout, J. S. Neergaard-Nielsen, I. Rigas, C. Kragh, A. Tipsmark, and U. L. Andersen, Amplification of realistic Schrödinger-cat-state-like states by homodyne heralding, Phys. Rev. A **87**, 043826 (2013).

[138] D. V. Sychev, A. E. Ulanov, A. A. Pushkina, M. W. Richards, I. A. Fedorov, and A. I. Lvovsky, Enlargement of optical Schrödinger's cat states, Nat. Photonics **11**, 379 (2017).

[139] H. Bachor and T. Ralph, *A Guide to Experiments in Quantum Optics* (Wiley-VCH Verlag, Weinheim, Germany, 2019).

[140] H. P. Yuen and V. W. S. Chan, Noise in homodyne and heterodyne detection, Opt. Lett. **8**, 177 (1983).

[141] A. I. Lvovsky, Iterative maximum-likelihood reconstruction in quantum homodyne tomography, J. Opt. B: Quantum Semiclass. Opt. **6**, S556 (2004).

[142] W. P. Schleich, *Quantum Optics in Phase Space* (Wiley-VHC Verlag, Weinheim, Germany, 2001).

[143] C. Gerry and P. Knight, *Introductory Quantum Optics* (Cambridge University Press, Cambridge, UK, 2005).

[144] U. Leonhardt, Measuring the quantum state of light, edited by P. Knight and A. Miller (Cambridge University Press, UK, 1997).

[145] U. Leonhardt, *Essential Quantum Optics* (Cambridge University Press, UK, 2010).

[146] G. T. Herman, *Image Reconstruction from Projections: The Fundamentals of Computerized Tomography* (Academic Press, New York, 1980).

[147] K. Banaszek, Quantum homodyne tomography with a priori constraints, Phys. Rev. A **59**, 4797 (1999).

[148] M. Leonhardt, Quantum statistics of a lossless beam splitter: SU(2) symmetry in phase space, Phys. Rev. A **48**, 3265 (1993).

[149] M. Zhang, H. Kang, M. Wang, F. Xu, X. Su, and K. Peng, Quantifying quantum coherence of optical cat states, Photonics Res. **9**, 887 (2021).

[150] E. Pisanty, G. J. Machado, V. Vicuña-Hernández, A. Picón, A. Celi, J. P. Torres, and M. Lewenstein, Knotting fractional-order knots with the polarization state of light, Nat. Photonics **13**, 569 (2019).

[151] E. Pisanty, L. Rego, J. San Román, A. Picón, K. M. Dorney, H. C. Kapteyn, M. M. Murnane, L. Plaja, M. Lewenstein, and C. Hernández-García, Conservation of Torus-Knot Angular Momentum in High-Order Harmonic Generation, Phys. Rev. Lett. **122**, 203201 (2019).

[152] L. Rego, K. M. Dorney, N. J. Brooks, Q. L. Nguyen, C.-T. Liao, J. San Román, D. E. Couch, A. Liu, E. Pisanty, and M. Lewenstein, *et al.*, Generation of extreme-ultraviolet beams with time-varying orbital angular momentum, Science **364**, eaaw9486 (2019).

[153] O. Neufeld, D. Podolsky, and O. Cohen, Floquet group theory and its application to selection rules in harmonic generation, Nat. Commun. **10**, 405 (2019).

[154] D. Ayuso, O. Neufeld, A. F. Ordonez, P. Decleva, G. Lerner, O. Cohen, M. Ivanov, and O. Smirnova, Synthetic chiral light for efficient control of chiral light-matter interaction, Nat. Photonics **13**, 866 (2019).

[155] P. Stammer, S. Patchkovskii, and F. Morales, Evidence of ac-Stark-shifted resonances in intense two-color circularly polarized laser fields, Phys. Rev. A **101**, 033405 (2020).

[156] D. Ayuso, A. F. Ordonez, P. Decleva, M. Ivanov, and O. Smirnova, Enantio-sensitive unidirectional light bending, Nat. Commun. **12**, 3951 (2021).

[157] G. P. Katsoulis, Z. Dube, P. Corkum, A. Staudte, and A. Emmanouilidou, Momentum scalar triple product as a measure of chirality in electron ionization dynamics of strongly-driven atoms, ArXiv:2112.02670 (2021).

[158] N. Mayer, S. Patchkovskii, F. Morales, M. Ivanov, and O. Smirnova, Imprinting Chirality on Atoms Using Synthetic Chiral Light Fields, Phys. Rev. Lett. **129**, 243201 (2022).

[159] J. Dziarmaga, W. H. Zurek, and M. Zwolak, Non-local quantum superpositions of topological defects, Nat. Phys. **8**, 49 (2012).

[160] I. Barth and O. Smirnova, Spin-polarized electrons produced by strong-field ionization, Phys. Rev. A **88**, 013401 (2013).

[161] A. Hartung, F. Morales, M. Kunitski, K. Henrichs, A. Laucke, M. Richter, T. Jahnke, A. Kalinin, M. Schöffler, L. P. H. Schmidt, M. Ivanov, O. Smirnova, and R. Dörner, Electron spin polarization in strong-field ionization of xenon atoms, Nat. Photonics **10**, 526 (2016).

[162] S. Eckart, M. Kunitski, M. Richter, A. Hartung, J. Rist, F. Trinter, K. Fehre, N. Schlott, K. Henrichs, L. P. H. Schmidt, T. Jahnke, M. Schöffler, K. Liu, I. Barth, J. Kaushal, F. Morales, M. Ivanov, O. Smirnova, and R. Dörner, Ultrafast preparation and detection of ring currents in single atoms, Nat. Phys. **14**, 701 (2018).

[163] J. Kaushal and O. Smirnova, Looking inside the tunnelling barrier III: Spin polarisation in strong field ionisation from orbitals with high angular momentum, J. Phys. B: At., Mol. Opt. Phys. **51**, 174003 (2018).

[164] D. Trabert, A. Hartung, S. Eckart, F. Trinter, A. Kalinin, M. Schöffler, L. P. H. Schmidt, T. Jahnke, M. Kunitski, and R. Dörner, Spin and Angular Momentum in Strong-Field Ionization, Phys. Rev. Lett. **120**, 43202 (2018).

[165] D. Ayuso, A. F. Ordonez, and O. Smirnova, Ultrafast chirality: the road to efficient chiral measurements, Phys. Chem. Chem. Phys. **24**, 26962 (2022).

[166] X. B. Planas, A. Ordóñez, M. Lewenstein, and A. S. Maxwell, Strong-field chiral imaging with twisted photoelectrons, Preprint ArXiv:2202.07289 (2022).

[167] J. I. Cirac, M. Lewenstein, K. Mølmer, and P. Zoller, Quantum superposition states of Bose-Einstein condensates, Phys. Rev. A **57**, 1208 (1998).

[168] V. Giovannetti, S. Lloyd, and L. Maccone, Quantum-enhanced measurements: Beating the standard quantum limit, Science **306**, 1330 (2004).

[169] G. Tóth and I. Apellaniz, Quantum metrology from a quantum information science perspective, J. Phys. A: Math. Theor. **47**, 424006 (2014).

[170] L. Pezze, A. Smerzi, M. K. Oberthaler, R. Schmied, and P. Treutlein, Quantum metrology with nonclassical states of atomic ensembles, Rev. Mod. Phys. **90**, 035005 (2018).

[171] E. Polino, M. Valeri, N. Spagnolo, and F. Sciarrino, Photonic quantum metrology, AVS Quantum Sci. **2**, 024703 (2020).

[172] E. O. Göbel and U. Siegner, *Quantum Metrology: Foundation of Units and Measurements* (John Wiley & Sons, 2015).

[173] M. Barbieri, Optical Quantum Metrology, PRX Quantum **3**, 010202 (2022).

[174] U. Bhattacharya, S. Chaudhary, T. Grass, A. S. Johnson, S. Wall, and M. Lewenstein, Fermionic Chern insulator from twisted light with linear polarization, Phys. Rev. B **105**, L081406 (2022).

[175] A. Maxwell, G. Armstrong, M. Ciappina, E. Pisanty, Y. Kang, A. Brown, M. Lewenstein, and C. F. de Morisson Faria, Manipulating twisted electrons in strong-field ionization, Faraday Discuss. **228**, 394 (2021).

[176] M. J. Vrakking, Control of Attosecond Entanglement and Coherence, Phys. Rev. Lett. **126**, 113203 (2021).

[177] L.-M. Koll, L. Maikowski, L. Drescher, T. Witting, and M. J. Vrakking, Experimental Control of Quantum-Mechanical Entanglement in an Attosecond Pump-Probe Experiment, Phys. Rev. Lett. **128**, 043201 (2022).

[178] M. J. Vrakking, Ion-photoelectron entanglement in photoionization with chirped laser pulses, J. Phys. B: At., Mol. Opt. Phys. **55**, 134001 (2022).

[179] C. Bourassin-Bouchet, L. Barreau, V. Gruson, J.-F. Hergott, F. Quéré, P. Salières, and T. Ruchon, Quantifying Decoherence in Attosecond Metrology, Phys. Rev. X **10**, 031048 (2020).

[180] H. Laurell, D. Finkelstein-Shapiro, C. Dittel, C. Guo, R. Demjaha, M. Ammitzböll, R. Weissenbilder, L. Neoričić, S. Luo, and M. Gisselbrecht, *et al.*, Continuous variable quantum state tomography of photoelectrons, Preprint ArXiv:2202.06798 (2022).

[181] D. Busto, H. Laurell, D. F. Shapiro, C. Alexandridi, M. Isinger, S. Nandi, R. Squibb, M. Turconi, S. Zhong, C. Arnold, and *et al.*, Probing electronic decoherence with high-resolution attosecond photoelectron interferometry, Preprint ArXiv:2111.12037 (2021).

[182] P. Stammer, J. Rivera-Dean, A. Maxwell, T. Lamprou, A. Ordóñez, M. F. Ciappina, P. Tzallas, and M. Lewenstein, Quantum electrodynamics of ultra-intense laser-matter interactions, Zenodo (2022).

[183] P. Virtanen, *et al.*, SciPy 1.0 Contributors, SciPy 1.0: Fundamental algorithms for scientific computing in Python, Nat. Meth. **17**, 261 (2020).

[184] J. Eberly, K. Wódkiewicz, and B. Shore, Noise in strong laser-atom interactions: Phase telegraph noise, Phys. Rev. A **30**, 2381 (1984).

[185] K. Wódkiewicz and J. Eberly, Effects of hidden transient noise processes on multiphoton absorption, J. Opt. Soc. Am. B. **3**, 628 (1986).